Numerical studies of edge states in hydrogen terminated silicene ribbons

Sho Tanaya

Doctoral Program in Physics

Submitted to the Graduate School of
Pure and Applied Sciences
in Partial Fulfillment of the Requirements
for Degree of Doctor of Philosophy in
Science

at the
University of Tsukuba

Acknowledgements

Contents

Chapter 1

Introduction

In this chapter, we review research background of this thesis : silicene, edge states in graphene ribbons, and hydrogen termination in graphene and silicene ribbons. After that, we mention the objective of this thesis.

1.1 Background of silicene

1.1.1 Prediction of silicene and its lattice structures on several substrates

Silicene is a quasi-two dimensional material that is a honeycomb lattice formed by silicon atoms, and was predicted firstly by a theoretical first principle total-energy calculation[1][Fig.1.1(a)]. This study also show that a buckled honeycomb structure is energetically stable and a linear dispersion is emerged at K and K' points in the energy band structure[Fig.1.1(b)]. Recently, stable and metastable structures of a free-standing silicene were further investigated using a first-principle calculation based on the density functional theory. Cahangirov *et. al.* conducted structural optimization numerically, and calculated phonon dispersion of silicene [2]. In the energy versus lattice constant plot, they found multiple energy minima corresponding to two different buckled structures and a planer structure [Fig.1.2(a)]. Two buckled structures have different degrees of buckling, namely, one has $\Delta \sim 2$Å and the other has $\Delta \sim 0.44$Å. They are named as high and low buckled structures, respectively. From the obtained phonon dispersions, Cahangirov *et. al.* also showed that planer and high buckled structures have imaginary phonon frequencies, and are energetically unstable. Therefore, they concluded that low-buckled structure is energetically stable.

Recently, monolayer silicene sheets have been synthesized on Ag(111)[3, 4, 5, 6, 7] , ZrB$_2$[8], and Ir(111)[9] substrates, and have been payed much attention in several research fields. Here, we introduce studies related to the lattice structures of silicene sheet on several substrates. Lin *et. al.* synthesized a silicene sheet using epitaxial growth on an Ag(111) substrate and investigated a structure of this silicene sheet by scanning tunneling microscopy (STM), low-energy electron diffraction (LEED), and angular-resolved photoelectron spectroscopy(ARPES) measurements combined with density functional theory (DFT) calculation. Fig.1.4(a) shows topographic STM images of silicene sheets on Ag(111) substrates. In this
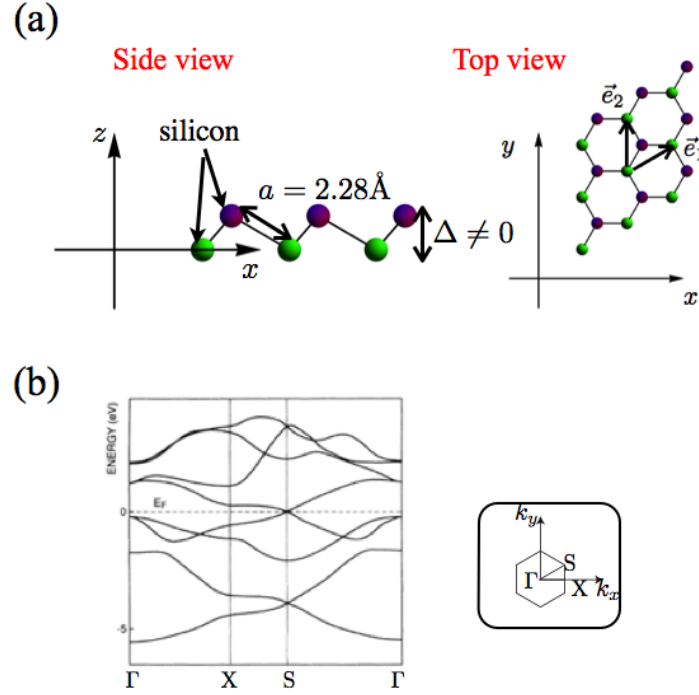
Fig. 1.1   (a): A schematic description of a lattice structure of silicene. Left and right panel show side and top views of silicene, respectively. Δ denotes buckling distance. Right panel shows top view of silicene. (b): Energy band structure of silicene obtained by first principle calculations with optimized lattice structure [1](left panel). In this figure, Γ, X, and S correspond to symmetric points in Brillouin zone(right panel).

figure, two types of atomic arrangements α and β are observed. An unit vector of α is aligned along the direction of symmetry axes of Ag(111) substrate, while an unit vector of β is rotated by 14° with respect to the symmetry axis. Figs. 1.4(a) and (b) show the high-resolution STM images of α and β, respectively. The length of the unit vector of $\alpha(\beta)$ is 11.5Å(10.4Å). From LEED measurements and DFT calculations, they show that α and β have the 4×4 and $\sqrt{13} \times \sqrt{13}$ superstructures on Ag(111) substrate. Lalmi *et. al.* also synthesized a silicene sheet on Ag(111) substrate and performed STM and LEED measurements combined with DFT calculation [3]. They obtained silicene sheet with the $2\sqrt{3} \times 2\sqrt{3}$ superstructure. It is argued that these variations of structures of silicene sheet on Ag substrate originated from temperature difference of substrates[3].

Fleurence *et. al.* synthesized a silicene sheet on ZrB_2 thin film and investigated its lattice structure via the STM measurements and its electronic structures by the angle-resolved ultraviolet photoelectron spectroscopy (ARUPS) measurements combined with DFT calculations. It is shown that silicene forms spontaneously through surface segregation on zirconium diboride thin films grown on Si wafers and has $\sqrt{3} \times \sqrt{3}$ superstructure[8]. Meng *et. al.* synthesized a silicene sheet on Ir(111) substrate and also investigated its lattice structure by STM and LEED measurements combined with DFT calculations. A silicene sheet on Ir(111) has
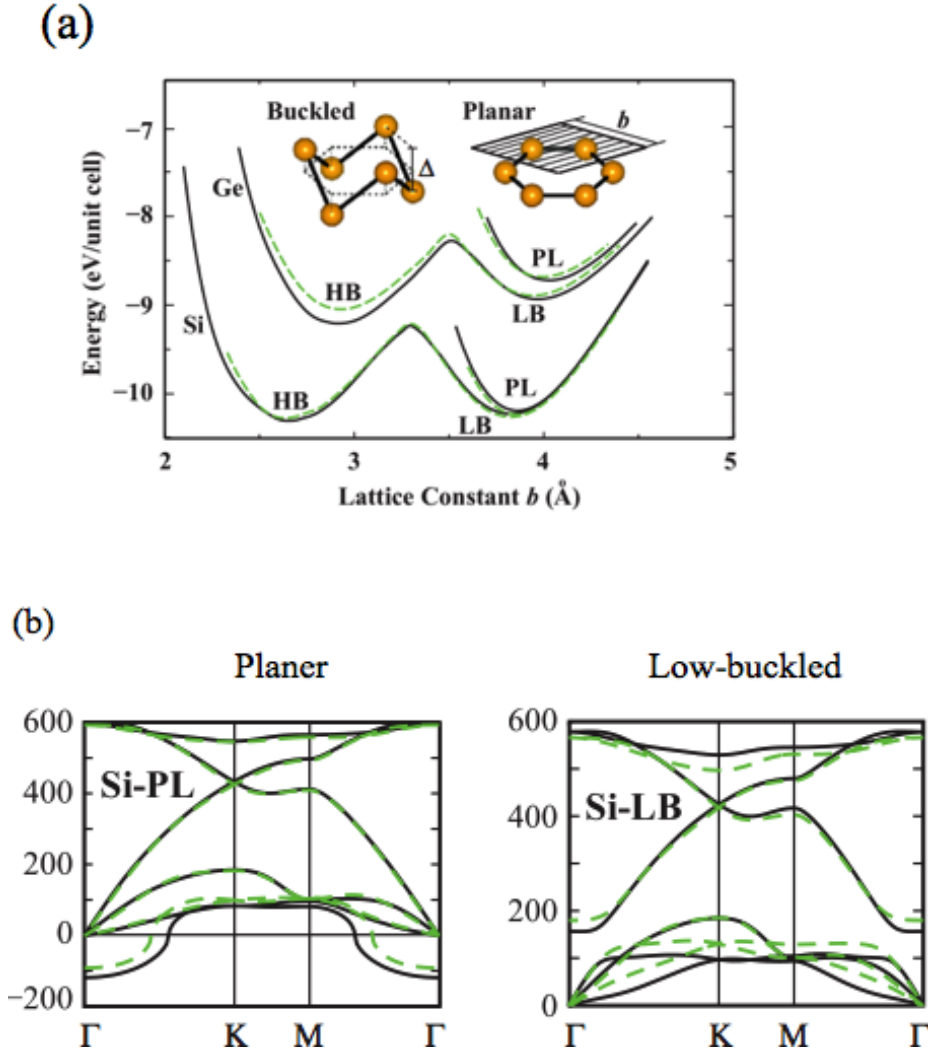
Fig. 1.2   (a) Energy versus hexagonal lattice constant of 2D Si and Ge calculated for various honeycomb structures. Black and dashed green curves of energy are calculated by local density approximation (LDA) using projector augmented wave (PAW) potential and ultrasoft pseudopotentials, respectively. (b): Phonon dispersion curves obtained by force-constant and linear response theory are presented by black and dashed green curves, respectively. [2]

$\sqrt{3} \times \sqrt{3}$ superstructure, as the one found in the case of silicene on ZrB_2[9].

Silicene ribbon, which is silicene with finite width , was also synthesized on Ag(110) substrate[10, 11, 12, 13, 14, 15]. Aufray *et. al.* synthesized a silicene ribbon on Ag(110) substrates and investigated its lattice structure by STM combined with DFT calculations[14]. According to the high resolution STM image of silicene ribbon in Fig.1.7(a), it was shown that silicene synthesized on Ag substrate forms a hexagonal structure. Furthermore, a detailed structure of silicene ribbon on Ag substrate was investigated by DFT calculations, and Aufray and co-worker showed that silicene ribbon tend to form a honeycomb structure [Fig.1.7(b)] and
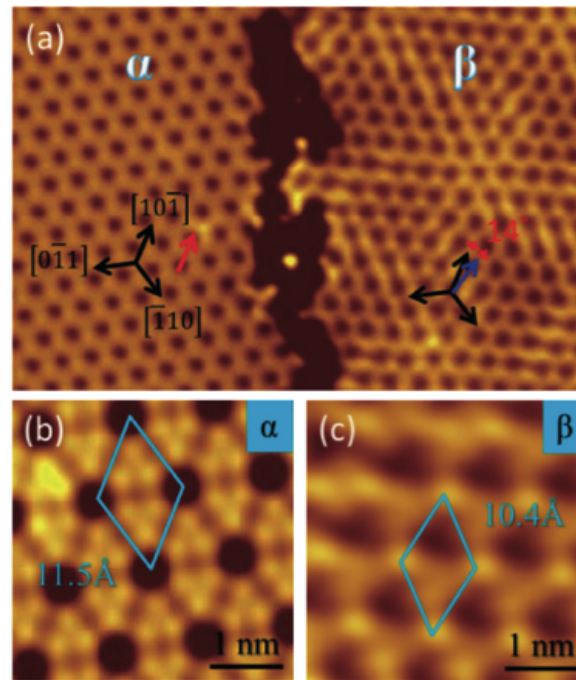
Fig. 1.3   (a) STM images of a silicene sheet on Ag(111) surface. In this figure, there exist two structures α and β[4].
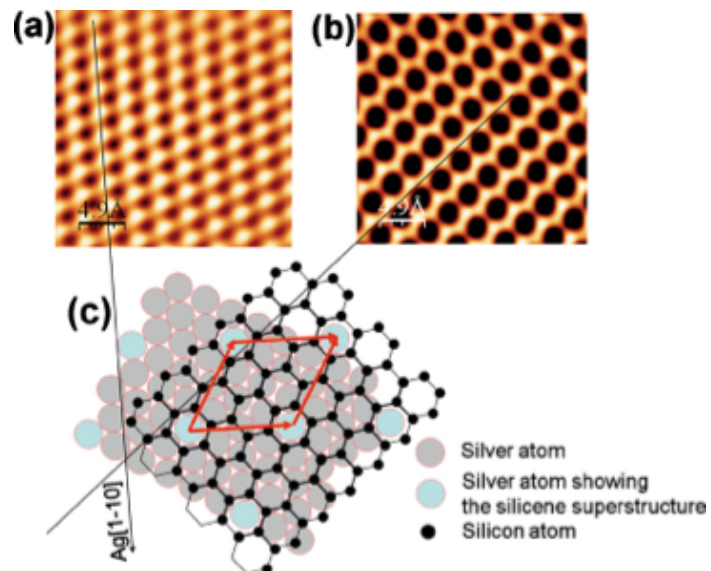
Fig. 1.4   (Color online).(a) STM images of a silicene sheet on Ag(111) surface. [3].
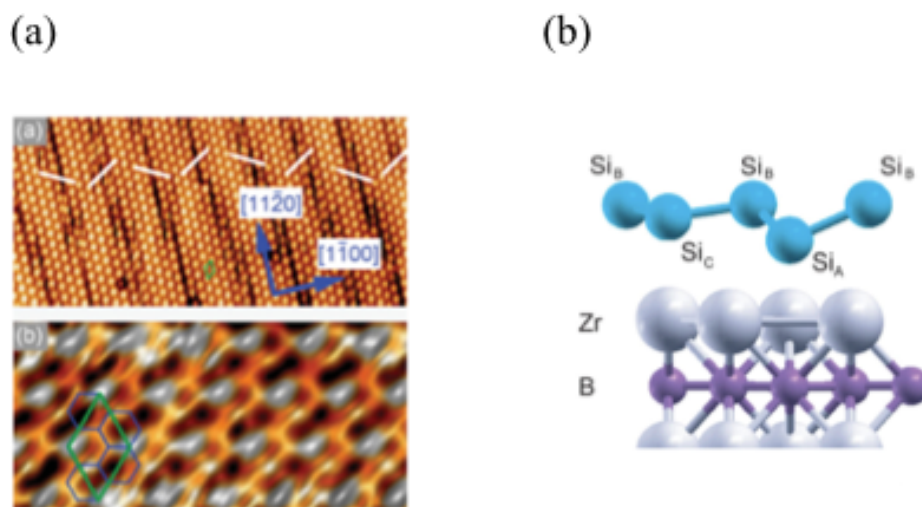
Fig. 1.5   (a):STM images of silicene sheet on Zr_2B substrate with different length scales 20nm×9.5nm(upper panel) and 4.2nm ×2nm(lower panel). (b): Ball model of silicene on ZrB_2 substrate [8].
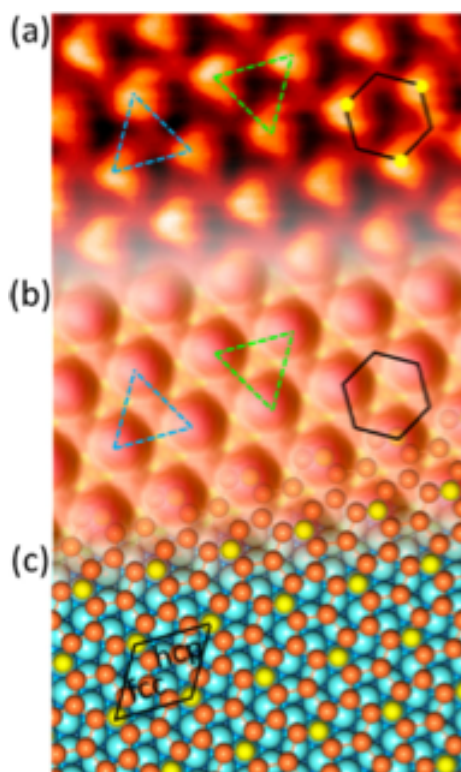
Fig. 1.6   (a)STM image of silicene sheet on Ir substrate. (b)Simulated STM image calculated by DFT calculations. (c) Top view of atomic models of silicene on Ir substrate[9].
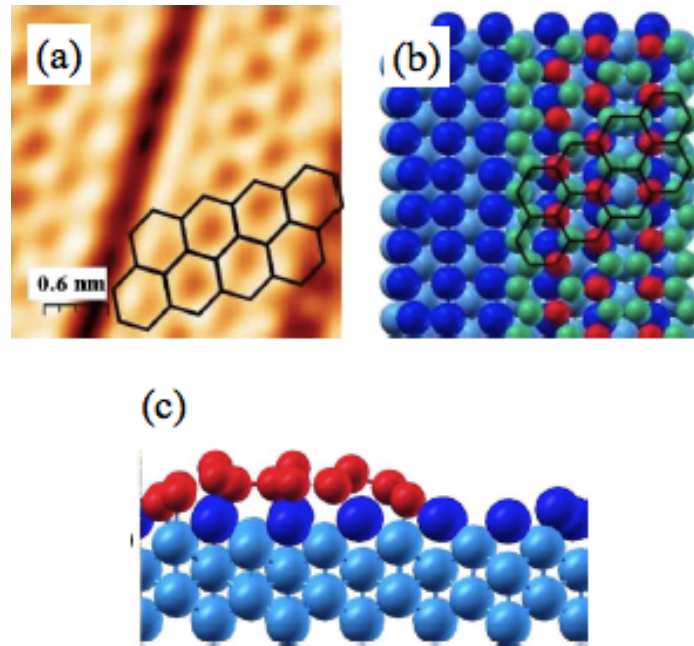
Fig. 1.7 (a) High resolution filled state STM images of a silicene ribbon. (b) Ball model for a calculated atomic structure of (a). Light green and red spheres represent bottom and top silicon atoms, respectively, while dark blue and light blue spheres represent top most and other silver atoms. (c) Side view of a calculated atomic structure of a silicene ribbon on a Ag substrate. Red spheres represent silicon atoms. [14]

an asymmetric buckling structure like an arch shape[Fig.1.7(c)]. These results of DFT calculations are consistent with a previous work[16].

Not only monolayer silicene ribbon and sheet, multilayer silicene ribbon [Fig.1.8(a)] and sheet [Fig.1.8(b)] have been also synthesized. Padova *et. al.* synthesized multilayer silicene ribbon on Ag(110) substrates and multi-layer silicene sheet on Ag(111) substrate using epitaxial growth technique[17, 18]. They also investigated its lattice structure by LEED, STM, reflection high-energy electron diffraction (RHEED), Auger electron spectroscopy (AES) measurements, and its electronic structures by ARPES measurements.

1.1.2 Electronic structures of silicene on several substrates

Next, we review electronic structures of these silicene sheet and ribbon on several substrates. In the seminal paper predicting the existence of silicene, the existence of the Dirac cone at the Fermi level is also predicted. However, as mention in previous subsection, silicene ribbons and sheets synthesized so far, have superstructures due to the strong interactions with substrates. This suggests that electronic structures of silicene ribbons and sheets are probably modulated by its super structures and the strong interactions with substrates. Here, we introduce some theoretical and experimental studies related to the existence of the Dirac
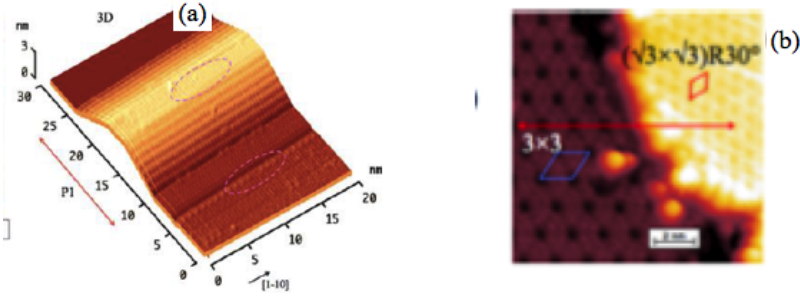
Fig. 1.8   STM images of multilayer silicene ribbon (a) and sheet (b) on Ag substrates [17, 18].

cone in silicene synthesized on Ag and ZrB_2 substrates.

Silicene sheets and ribbons on Ag substrates

It was reported in many theoretical and experimental studies that the Dirac cone is absent for silicene sheets with super lattice structures on Ag(111) substrates. Avila and coworkers carried out ARPES and LEED measurements against 4×4 silicene on Ag(111) substrate, and showed that an energy gap exists near the Fermi level at the $\bar{\Gamma}_{00}$ point where the K point in the original Brillouin zone(BZ) of silicene without super structure is folded[Fig.1.9(a)]. Guo and his coworkers worked on the first principle calculations of 4×4 and $\sqrt{13} \times \sqrt{13}$ silicene on Ag(111) substrate, and showed that energy band around the $\bar{\Gamma}_{00}$ point observed by Avila *et. al.*, is originated from Ag substrates[19]. They also noticed that π and π^* states that form the Dirac cone disappear from neighborhood of the Fermi level and appear in valence bands. They pointed out that these results are caused by the electron transfer from Ag substrate to silicene due to the strong interactions between silicene and Ag substrates[Fig.1.9(b)]. They also investigated electronic structures of silicene sheets with superstructures, which are peeled from silver substrate, and showed that sizable energy gap exists for 4×4 silicene, while energy gap for $\sqrt{13} \times \sqrt{13}$ silicene is negligibly small. In the case of 4×4 silicene, Cahangirov *et. al.* also obtained same results[20]. Furthermore the absence of the Dirac fermion in silicene on Ag substrate near the Fermi level was also suggested from an absence of $n = 0$ Landau level via STS measurements[21]. Similarly electronic structures of a silicene ribbon on Ag(110) was also investigated via ARPES measurements by Padova *et. al.*, and they found energy gap near the Fermi level in the electronic structures[12].

Silicene on a ZrB_2 substrate

As mentioned earlier, electronic structures of silicene sheet on ZrB_2 substrate, was investigated through the ARUPS measurements combined with DFT calculations by Fleurence and his coworkers[8]. Figure.1.12(b) shows ARUPS spectra along high symmetry directions. Features S_n and X_n in Fig.1.12(b) correspond to surface electronic states of diboride and those of epitaxial silicon layer, respectively. According to the analysis of Fleurence *et. al.*, a feature X_2 corresponds to a π
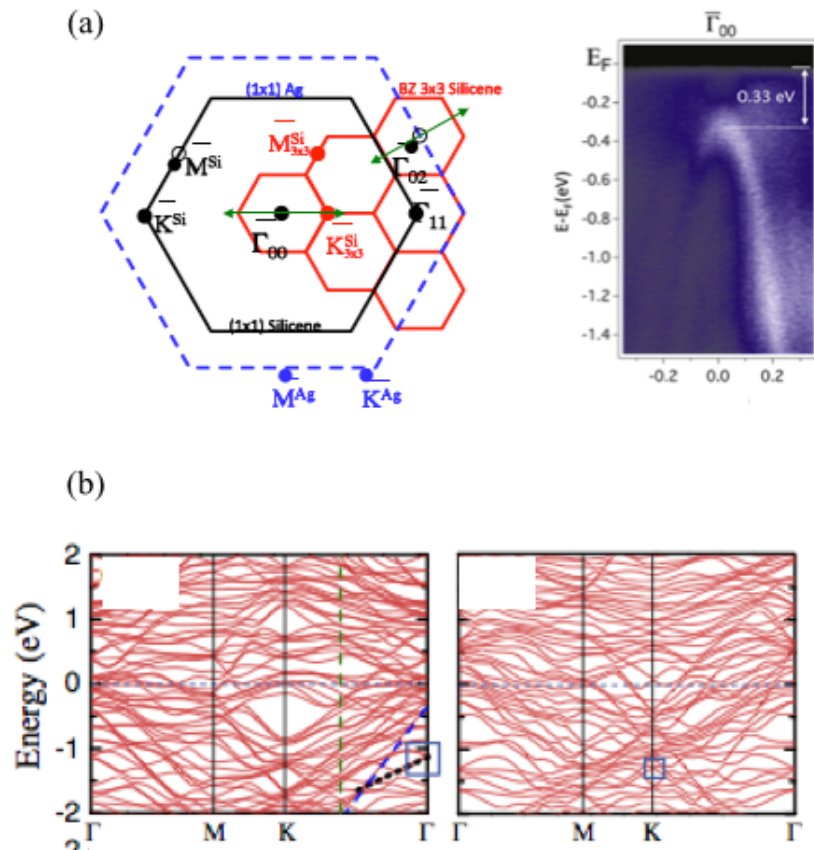
Fig. 1.9   (a)Left panel shows the Brillouin zones of Ag (blue), 1×1 silicene and 4×4 silicene. The green arrows indicate the directions on which the ARPES measurements have been carried out at each symmetry point[22]. Right panel shows that ARPES spectrum measured at the $\bar{\Gamma}_{00}$ point, along the $K - \Gamma - K$ direction. (b) Calculated energy bands of 4×4 (left panel) and $\sqrt{13} \times \sqrt{13}$ (right panel) silicene on Ag(111) substrates[19]. Blue squares indicate the region in which π and π^* states exist. Blue dashed line represents energy band observed by ARPES measurements.
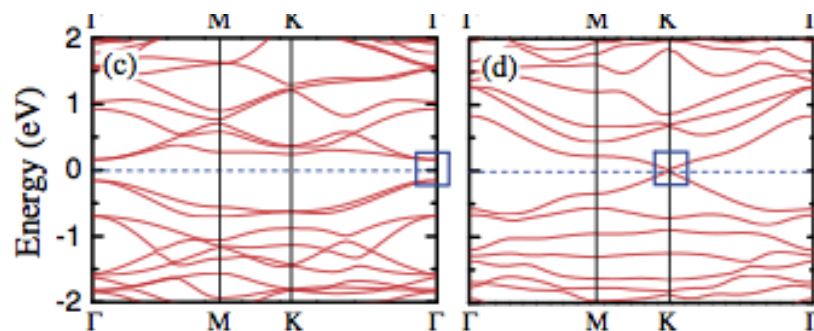
Fig. 1.10   (Color online) Calculated energy bands of 4×4(left panel) and $\sqrt{13} \times \sqrt{13}$(right panel) silicene peeled from silver substrate. [19].
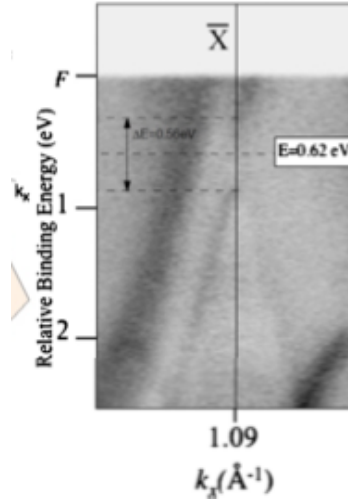
Fig. 1.11   ARPES spectrum of silicene ribbon on Ag(110) substrate[12].
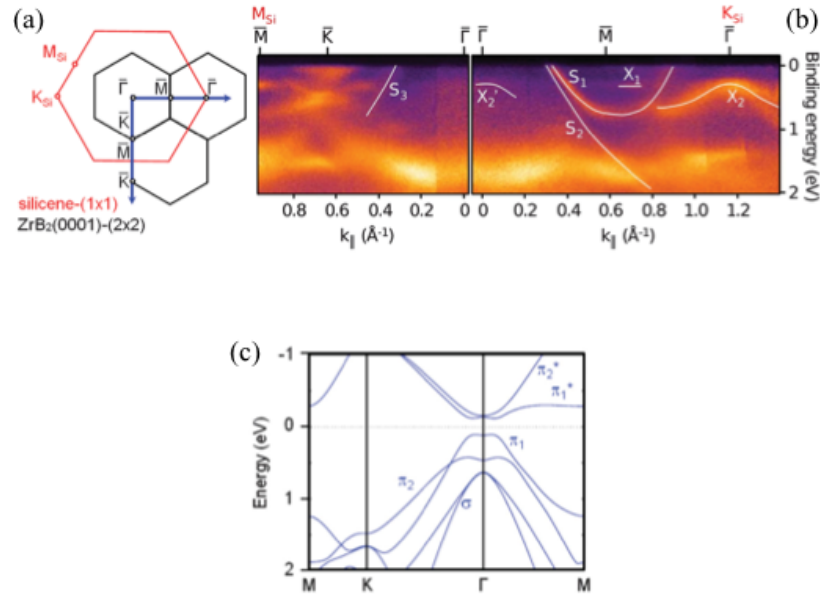
Fig. 1.12   (a) BZs of $ZrB_2(0001)$ surface with 2×2 superstructure (black line) and (1×1)silicene (red line). The K_{Si} point in the BZ of (1×1) silicene is folded on $\bar{\Gamma}$ point in the BZ of ZrB_2. (b) ARUPS spectra along the $\bar{M} - \bar{K} - \bar{\Gamma}$ and $\bar{\Gamma} - \bar{M} - \bar{\Gamma}$ directions. (c) Calculated energy bands of silicene with a $\sqrt{3} \times \sqrt{3}$ superlattice structure peeled from ZrB_2 substrate. [8]

band and there is an energy gap of 0.25eV at the $\bar{\Gamma}$ point. They also calculated a stable structures of silicene on ZrB_2 substrate and energy band of silicene peeled from its substrate through the first-principle methods, and showed that energy gap opening occurs at Γ points and a π_1 band in Fig.1.12(c) corresponds to a X_2 bands observed in ARUPS spectra.
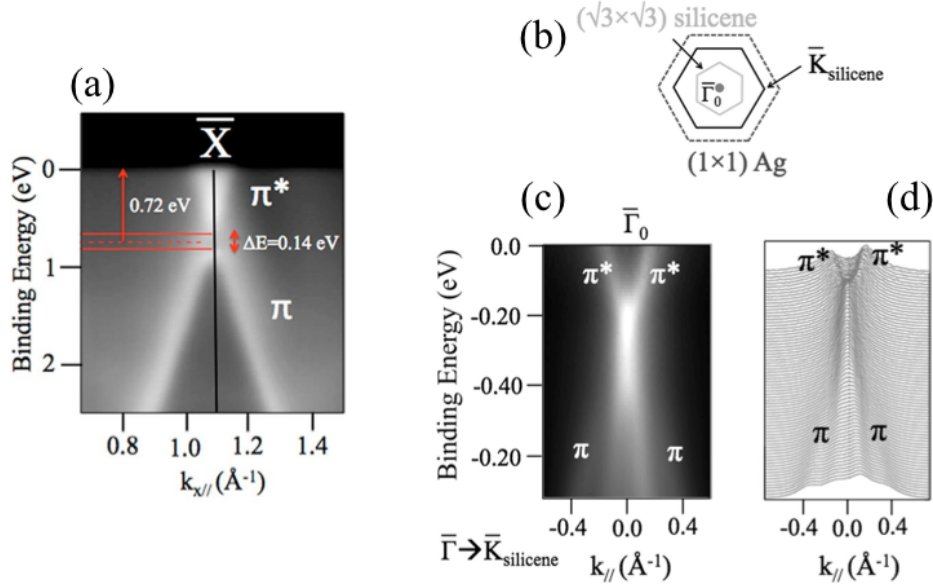
Fig. 1.13 (a) ARPES spectrum of multilayer silicene ribbon on Ag(110) substrate[17]. (b) Schematic description of BZs. (c) ARPES spectra of multilayer $\sqrt{3} \times \sqrt{3}$ silicene sheet. (d) The line profiles of (c)[18].

Multi-layer silicene

As monolayer silicene on Ag substrates, electronic structures of multilayer silicene on the same substrates were also investigated. Padova *et. al.* carried out ARPES measurements against multilayer silicene ribbons, and showed that energy gap opening occurs near the Fermi level[Fig.1.13(a)] and this gap narrows as the number of silicene layers increase [17]. Furthermore Padova *et. al.* performed ARPES measurements against multilayer silicene sheets where a $\sqrt{3} \times \sqrt{3}$ silicene sheet on a 3×3 silicene sheet, and observed the Dirac cone[Fig.1.13(c) and (d)][18].

Energy gap due to the spin-orbit interaction

Previously, we reviewed studies on energy gaps of silicene on several substrates. Here, we brief energy gap opening due to the spin-orbit interaction in ideal silicene and related studies. Since it is expected that a free-standing silicene has the Dirac cone at K and K' points, the spin-orbit coupling in silicene was investigated by DFT calculations in terms of quantum spin Hall effects. Liu *et. al.* performed first-principle calculations of energy bands of silicene as a function of bond angles, and showed that the spin-orbit band gap is 1.55meV for a low-buckled silicene that is an energetically stable structure ($\theta = 101.73°$)[23]. Based on this result, Liu *et. al.* also derived a low-energy effective hamiltonian involving spin-orbit coupling that is estimated as 3.9meV[24]. Using this hamiltonian, many theoretical works have been conducted in order to elucidate exotic features of silicene, such as a silicene under an electric field[25], zigzag and armchair nano-ribbons[26], quantum Hall effects[27], silicene nanotube[28], bilayer silicene[29], edge states of silicene

nanodisk[30]. In this thesis, we do not take into account the spin-orbit interaction because we consider the physics of silicene in the energy scale of eV order.

1.1.3   Theoretical proposal of several substrates for an emergence of the Dirac cone

As mentioned above, an ideal silicene as a Dirac fermion system has not yet synthesized experimentally. However, hexagonal boron nitride (h-BN) and hydrogen processed Si(111) surface were theoretically proposed as candidates of substrates on which the Dirac cone emerges in silicene by Guo *et. al.*[19]. They showed that energetically stable structures of silicene on h-BN and H-Si(111) are hexagonal structure with $\sqrt{3} \times \sqrt{3}$ super-periodicity and without super-periodicity, respectively[Fig.1.14]. Figures.1.14(a) and (b) show calculated energy bands of silicene sheets on h-BN and hydrogen processed Si(111) substrates. We can see that the Dirac cone is realized at the Fermi level. These results indicate that an appropriate choice of substrates is crucial for experimental realization of ideal silicene and for enabling us to regard silicene as a Dirac fermion system.

1.2   Physics of edge states and its topological origin for graphene

In this thesis, we focus on physics of edge states in silicene ribbons. Then, it is natural to make a comparison between silicene and graphene, which is a close relative of silicene and is known to host novel edge states. In this section, we will review edge states in graphene ribbons and its topological origin.

1.2.1   Edge states in graphene ribbons

Analysis of graphene ribbons using a single orbital tight-binding model[31, 32, 33] revealed that they have characteristic flat bands in energy spectra. The flat bands are originated from edge states, whose wave functions are localized to the edge. Interestingly, the edge states depend crucially on the edge geometries. For a graphene ribbon with zigzag edge, flat band emerges in regions of a wave number space $-\pi \leq k \leq -2\pi/3$ and $2\pi/3 \leq k \leq \pi$ at the Fermi level[Fig.1.15(a)], and its wavefunctions localize near the both edges (edges state). Similarly, for the case of Klein edge, flat bands also emerges in a region of a wave number space $-2\pi/3 \leq k \leq 2\pi/3$[Fig.1.15(b)] and its wave functions are edge states localized to edges. On the other hand, for the case of the armchair edge there are no flat bands and edge states[Fig.1.15(c)]. The edge state for a graphene ribbon with zigzag edge, is also confirmed by a first principle calculation based on DFT[Fig.1.16(a)][34], and is experimentally observed by STM measurements[Fig.1.16(b)][35].
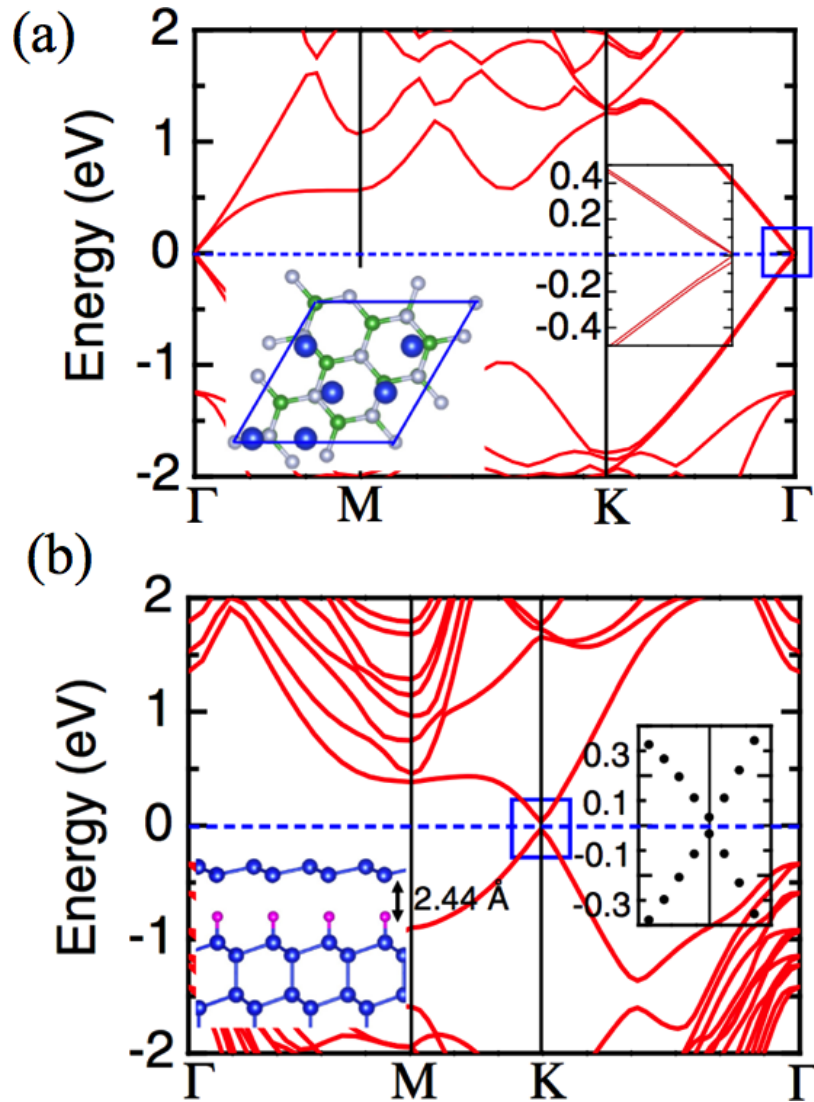
Fig. 1.14   Calculated energy bands of silicene on h-BN(a) and hydrogen processed Si(111) surface(b)[19]. Enlarged views of energy bands near the Fermi energy are shown in the insets, respectively. In (a), top view of optimized lattice structure is shown in another inset where blue, green and white spheres indicate Si, B and N atoms, respectively. Similarly, in (b), side view of optimized lattice structure is shown in another inset where blue and purple spheres indicate Si and H atoms, respectively.

1.2.2   Topological aspects of edge states

Emergence of edge states are not specific phenomena not only for graphene ribbons but also for edge currents of quantum Hall system[37], and degrees of freedom of edge spins in one-dimensional quantum spin systems[38]. Furthermore, existence of these edge states are not accidental and its properties reflect bulk features. This
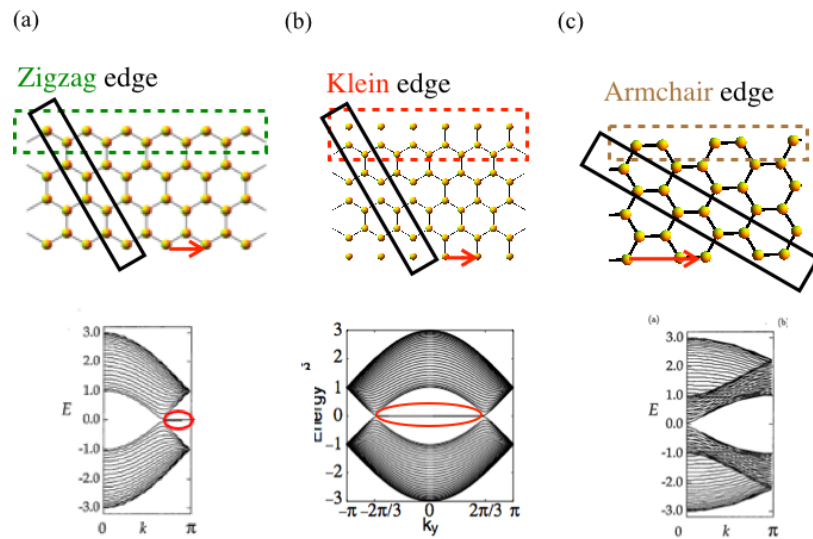
Fig. 1.15 Lattice geometries of graphene ribbons with several edge shapes(upper panels). Green, red and brown dashed squares indicate edge geometries of zigzag, Klein and armchair edges, respectively. Squares with solid line indicate the unit cells. Energy spectra for graphene ribbons with zigzag(a)[31], Klein(b)[32, 36] and armchair(c)[31] edges as functions of wave number k calculated from reciprocal lattice vector given by translational vectors(red arrow)(lower panels). Red circles indicate edge states.
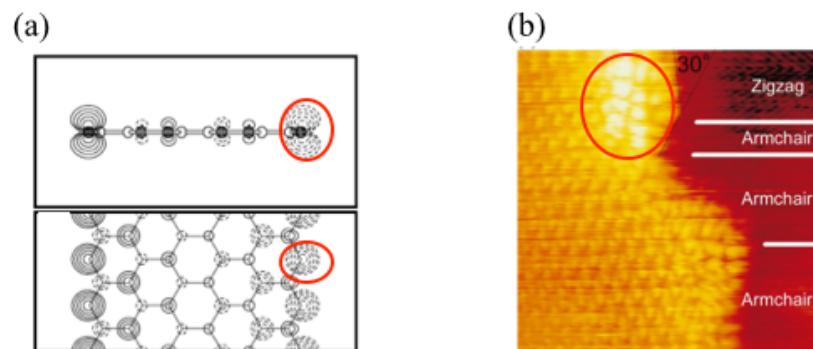
Fig. 1.16   (a):Calculated contour plots of spin density on a plane perpendicular to a zigzag graphene ribbon(upper panel) and a plane including a zigzag graphene ribbon(lower panel)[34]. (b):a STM image of graphene flakes with zigzag and armchair edges[35]. Red circles indicate edge states at zigzag edges.

idea is known as Bulk-Edge correspondence[39]. Based on this idea, it is expected that edge states can be detected by topological quantities which are calculated from bulk wave functions. Typical examples of these topological quantities are the Chern number as the Hall conductivity in quantum Hall systems[40, 41] and Z_2 Berry phase for a detection of edge states in Dirac fermion systems[42, 43, 36, 44]. Here, we explain topological aspects of the existence of flat-bands discussed through the Z_2 Berry phase[42, 43, 36] in graphene ribbons with several edge geometries.

Ryu *et. al.* established a criterion to determine the existence of zero-energy edge states of graphene ribbons with several edge geometries in terms of bulk properties[36]. For discussion of zero energy edge states of the graphene ribbons with several edge geometries, Ryu *et. al.* considered the Fourier transformed hamiltonians for several types of unit cells[left panels of Fig.1.18(a), (b) and (c)]. These hamiltonians formally given as $H = \sum_{k_x,k_y} H_{1D}^Z(k_x, k_y) = \sum_{k_x,k_y} H_{1D}^K(k_x, k_y) = \sum_{k_x,k_y} H_{1D}^A(k_x, k_y)$, where $H_{1D}^Z(k_x, k_y)$, $H_{1D}^K(k_x, k_y)$ and $H_{1D}^A(k_x, k_y)$ are 2×2 Hermitian matrices. Generally, tuning constants of diagonal elements 2×2 Hermitian matrices can be expand using the Pauli matrices σ_x, σ_y and σ_z with real constants[45, 42] [1]. Thus, excepting constants of diagonal elements$[R_z(k_x, k_y)] = 0$, hamiltonian $H(k_x, k_y)$ can be expressed as $H(k_x, k_y) = \mathbf{R}(k_x, k_y) \cdot \boldsymbol{\sigma}$ and described explicitly as follows:

$$H(k_x, k_y) = R_x(k_x, k_y)\sigma_x + R_y(k_x, k_y)\sigma_y. \tag{1.1}$$

This hamiltonian possesses the chiral symmetry [2]. In addition, Ryu *et. al.* considered a loop $\mathcal{L} : (k_x, k_y) \to R(k_x, k_y) \in \mathbb{R}^3$ in a parameter space R, and showed three conditions for a system for H_{1D} to support zero-energy edge states as follows:

1. $\mathcal{L}$ is on a 2D plane ($R_z = 0$) that contains the origin $\mathcal{O}$ of a parameter space R[Fig.1.17(a)].

2. $\mathcal{L}$ is continuously deformed to $\mathcal{L}_c$ without crossing $\mathcal{O}$[Fig.1.17(a)].

---

[1]

$$H = \mathbf{R} \cdot \boldsymbol{\sigma}$$

$$= R_x\sigma_x + R_y\sigma_y + R_z\sigma_z = \begin{pmatrix} R_z & R_x - iR_y \\ R_x + iR_y & -R_z \end{pmatrix}.$$

Eigen energies of H are given as $E = \pm R$, where $R = \sqrt{R_x^2 + R_y^2 + R_z^2}$. For $R = O$, eigen energies degenerate.

[2] The system possesses the chiral symmetry when a hamiltonian H satisfies the anti-commutation relation $\{H, \Gamma\} = 0$, where the chiral operator Γ is defined as follows:

$$\Gamma = \begin{pmatrix} 1 & 0 \\ 0 & -1 \end{pmatrix}$$
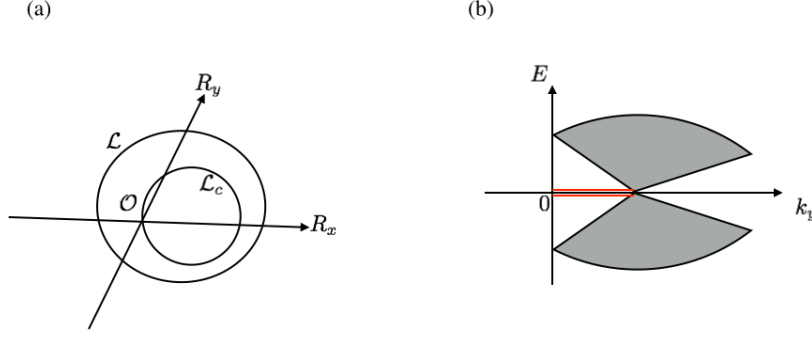
Fig. 1.17   Schematic illustrations of a loop $\mathcal{L}$ of a parameter space R(a) and energy spectra as function of k_y. Shade regions and red lines indicate energy spectra of bulk and zero energy edge states, respectively.

3. Edges of one-dimensional system possess the chiral symmetry.

In the second condition, parameters k_x and k_y $\mathcal{L}_c$ corresponds to the gap closing point in Fig.1.17(b). Ryu *et. al.* evaluated these conditions in $H_{1D}^Z(k_x, k_y)$, $H_{1D}^K(k_x, k_y)$ and $H_{1D}^A(k_x, k_y)$, and showed that regions of k-space that emerges zero energy edge states and that satisfies these conditions, are coincident[middle panels of Fig.1.18(a), (b) and (c)].

Based on this criterion, Hatsugai calculated the Berry phase in k-space (Zak phase)[46] for several types of one dimensional periodic systems[43, 47]. Zak phase is the Berry phase calculated from the integration with respect to a direction of the wave number space. Using these expressions, the Berry phase $\gamma(k_y)$ is defined as follows:

$$\gamma(k_y) = -i \int_{-\pi}^{\pi} dk_x \langle \mathbf{R}(k_x, k_y)| \frac{\partial}{\partial k_x} |\mathbf{R}(k_x, k_y)\rangle, \tag{1.2}$$

where $|\mathbf{R}(k_x, k_y)\rangle$ is one particle state of $H(k_x, k_y)$. Generally, it was showed that this Berry phase is quantized as 0 or π modulo 2π for the system possessing the chiral symmetry [43, 48]. Reflecting the first condition of this criterion, if the zero energy edge states exist, then the Berry phase should be π modulo 2π[49, 47, 36]. On the other hand, if the zero energy edge states absent, then the Berry phase should be 0 modulo 2π. The Berry phases of $H_{1D}^Z(k_x, k_y)$, $H_{1D}^K(k_x, k_y)$ and $H_{1D}^A(k_x, k_y)$ are calculated as follows:

$$\gamma^Z(k_y) = \begin{cases} \pi & |k_y| > \frac{2\pi}{3} \\ 0 & \text{otherwise} \end{cases}$$

$$\gamma^K(k_y) = \begin{cases} \pi & -\frac{2\pi}{3} < k_y < \frac{2\pi}{3} \\ 0 & \text{otherwise} \end{cases}$$

$$\gamma^A(k_y) = 0 \ (k_y \neq 0), \tag{1.3}$$

where $k_y = \pm\frac{2\pi}{3}$ for γ^Z and γ^K, and $k_y = 0$ for γ^A correspond to the gap closing points, respectively. Thus, the existence of edge states can be also discussed via
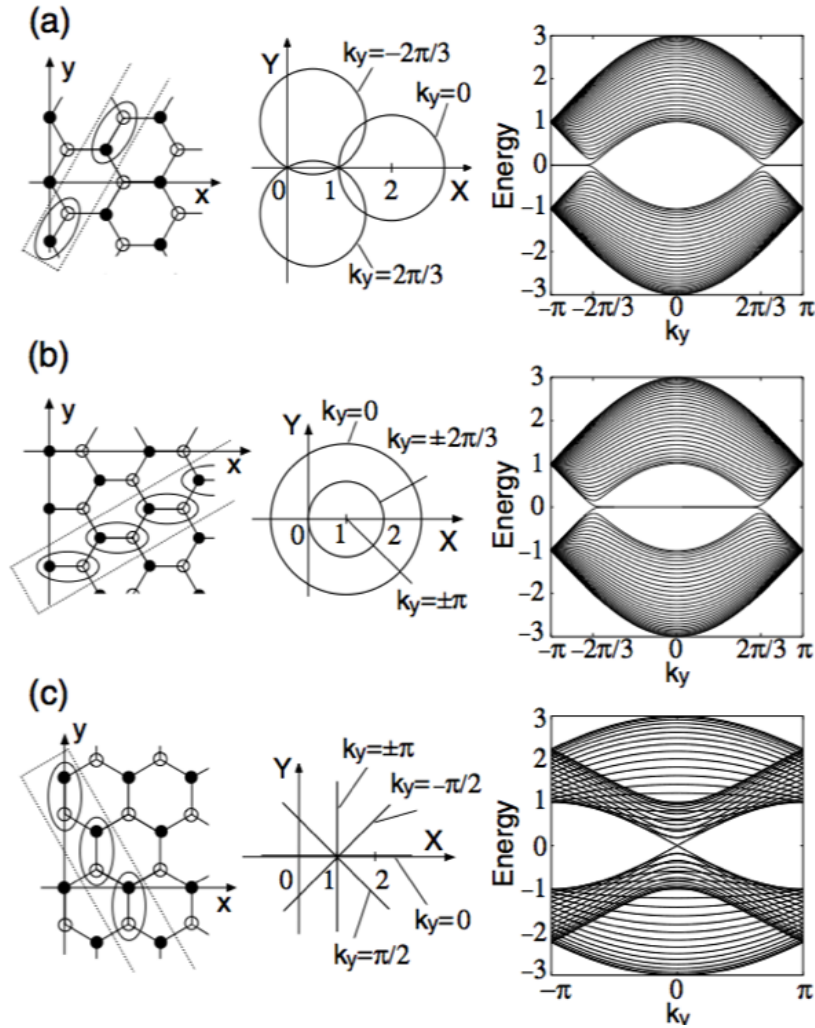
Fig. 1.18 Lattice geometries, loops in **R** space, and the energy spectrum of graphene ribbons with zigzag (a), Klein (b), and armchair (c) edges. Dotted squares indicate unit cell for the graphene ribbons with each edge geometries. [36]

the Berry phase, which is calculated from the wave functions of bulk, and can be correlated to the bulk features.

1.3 Hydrogen termination in silicene and graphene ribbons

In the previous section, we mentioned about physics of edge states of graphene ribbons with several edge geometries. In electronic structures of graphene ribbons, results calculated by a single orbital tight-binding model and a DFT calculation are unexpectedly similar. Because graphene prefer constructing sp^2 hybridized orbitals, π and σ orbitals are orthogonal[Fig.1.19(a)]. A binding energy of σ bond is larger than that of π bond. σ orbitals of carbon atoms on edges, which called dangling bonds, bond hydrogen atoms, in other words, dangling bonds are terminated
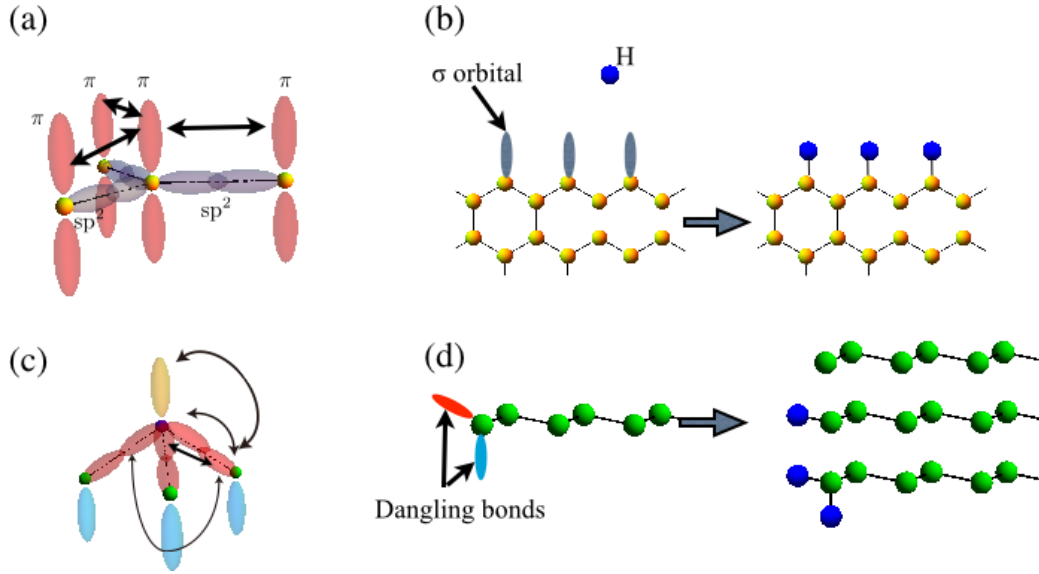
Fig. 1.19   Schematic illustrations of single orbital approach for graphene (a) and multi orbital approach for silicene (c), respectively. Schematic illustrations of hydrogen terminations for graphene (b) and for silicene (d), respectively.

by hydrogen atoms[Fig.1.19(b)]. Thus, π electrons contribute mainly edge states near the Fermi level. However, it is thinkable that four orbital of carbon atoms on the edges construct sp^3-like hybridized orbitals then bond hydrogen atoms. Then that influences crucially edge states of graphene ribbons. By contrast, silicene prefer constructing sp^3-like hybridized orbitals rather than sp^2, then these four orbitals are almost equivalent and its binding energies are almost the same. Hence, for the case of an investigation of edge states in electronic structures, a multi orbital treatment is needed different from the case of graphene[Fig.1.19(c)]. Besides, when the silicene is synthesized experimentally, it is expected that dangling bonds of silicene in edge and bulk region are terminated by hydrogen atoms. If we consider the desorption of these hydrogen atoms, several types of edge termination can be possible due to the construction of sp^3-like hybridized orbitals[Fig.1.19(d)]. Therefore, for the consideration of edge states in silicene ribbons, it is significant to take into account variations of the hydrogen termination at edge atoms. In this section, we introduce some theoretical and experimental studies of graphene and silicene ribbons as examples that hydrogen termination affects edge states.

1.3.1   graphene ribbons

Kusakabe *et. al.* investigated electronic structures of a graphene ribbon ,whose each carbon atom at one side is terminated by single hydrogen atom like the sp^2 orbitals and each one at another side is terminated by two hydrogen atoms like the sp^3 orbitals, by DFT calculations, and showed that flat bands emerge near the Fermi level in the whole space of the wave number[Fig.1.20(b)] and wave functions

of these flat bands localize mainly at carbon atoms α and γ in Fig.1.20(a) [50]. Simultaneously, amplitude of wave functions at a carbon atom β disappears due to the sp^3-like hydrogen termination. From these results, they indicated that the Klein edge fictitiously realized in the side of the edge with the sp^3-like hydrogen termination. Besides, Ziatdinov *et. al.* also investigated effects of hydrogen termination to edge states by STM measurements against edge of nanoholes in graphene combined with DFT calculation[51]. They observed experimentally that localized states at portion of carbon atoms on zigzag edges disappear via STM images, and show that this result is caused by the di-hydrogenation of carbon atoms at zigzag edges[Fig.1.20(c)]. These results were also obtained by other groups[52, 53]. These studies of the termination with two hydrogen atoms indicated that edge states could be modified by hydrogen terminations.

1.3.2   silicene ribbons

Kang *et. al.* investigated electronic structure of a free-standing zigzag silicene ribbon with sp^2 like hydrogen termination[Fig.1.21(b)] using DFT calculations and obtained energy band that is similar to that of a zigzag graphene ribbons with sp^2 like hydrogen termination[Fig.1.21(b)][54]. Besides, Ding *et. al.* also investigated electronic structure of a silicene ribbon with asymmetrical hydrogen terminations sp^2 and sp^3 [Fig.1.21(c)] using DFT calculations and show that flat bands emerge near the Fermi level in the whole space of the wave number[Fig.1.21(d)] and wave functions of flat bands in the region indicated open red circles in Fig.1.21(d) mainly localize at the silicon site Si_2 indicated in Fig.1.21(c), and wave functions of flat bands in the region indicated open blue circles in Fig.1.21(d) mainly localize at the silicon site Si_{12} indicated in Fig.1.21(c). From these results, they pointed out that the Klein edge is fictitiously realized at the edge with the sp^3 like hydrogen termination similar to the case of a graphene ribbon.

1.4   Objective of this thesis

Up to here, we reviewed background of this thesis, silicene, edge states in graphene ribbons with several edge geometries, and effects of hydrogen termination on edge states in graphene and silicene ribbons. For an investigation of electronic properties of silicene, multi orbital treatments are essentially significant because of the buckling structure. These treatments are also important for the comparison between graphene and silicene in terms of the Dirac fermion systems. Additionally, realization of several types of the hydrogen termination on the edges can be possible, and these affects edge states in hydrogen terminated silicene ribbons. Consequently, it is thinkable that characteristic features of edge states emerge in hydrogen terminated silicene ribbons. In this thesis, we investigate a relation between several types of hydrogen terminations and edge states of zigzag silicene ribbons, and its physical origin of these edge states. To understand this fundamentally, we consider multi-orbital tight-binding model on a honeycomb lattice. There are two reasons to adapt the multi-orbital approach. First is that sp^3 and
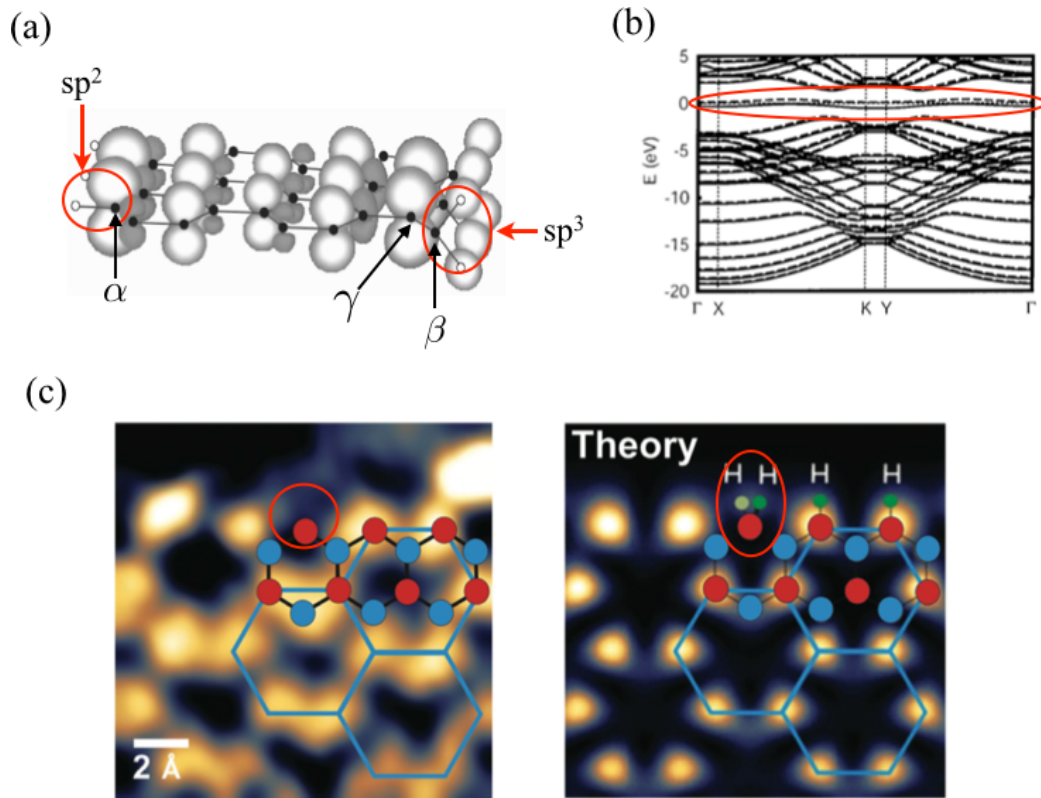
Fig. 1.20   (a) The optimized structure of a graphene ribbon with monohydrogenated and dihydrogenated zigzag edges. Black and white circles represent carbon and hydrogen atoms, respectively. Bright and dark surface represent spin-up and spin-down densities of flat bands, respectively. α, β and γ denote carbon atoms near the zigzag edges. Red circles indicate two types of hydrogen terminations.[50] (b) Calculated energy bands of a zigzag graphene ribbon with with monohydrogenated and dihydrogenated zigzag edges. Red circle indicates flat bands.[50] (c) Experimental(left panel) and theoretically calculated(right panel) STM images of graphene with monohydrogenated and dihydrogenated zigzag edge. Red and blue filled circles represent carbon atoms, and bright and dark green filled circles represent hydrogen atoms. [51]

sp^2 orbitals hybridize due to the buckled honeycomb structure. Second is to taking into account the effect of hydrogen termination. For the case of single orbital treatment, comparison between graphene and silicene, and effects of hydrogen termination can not be discussed.
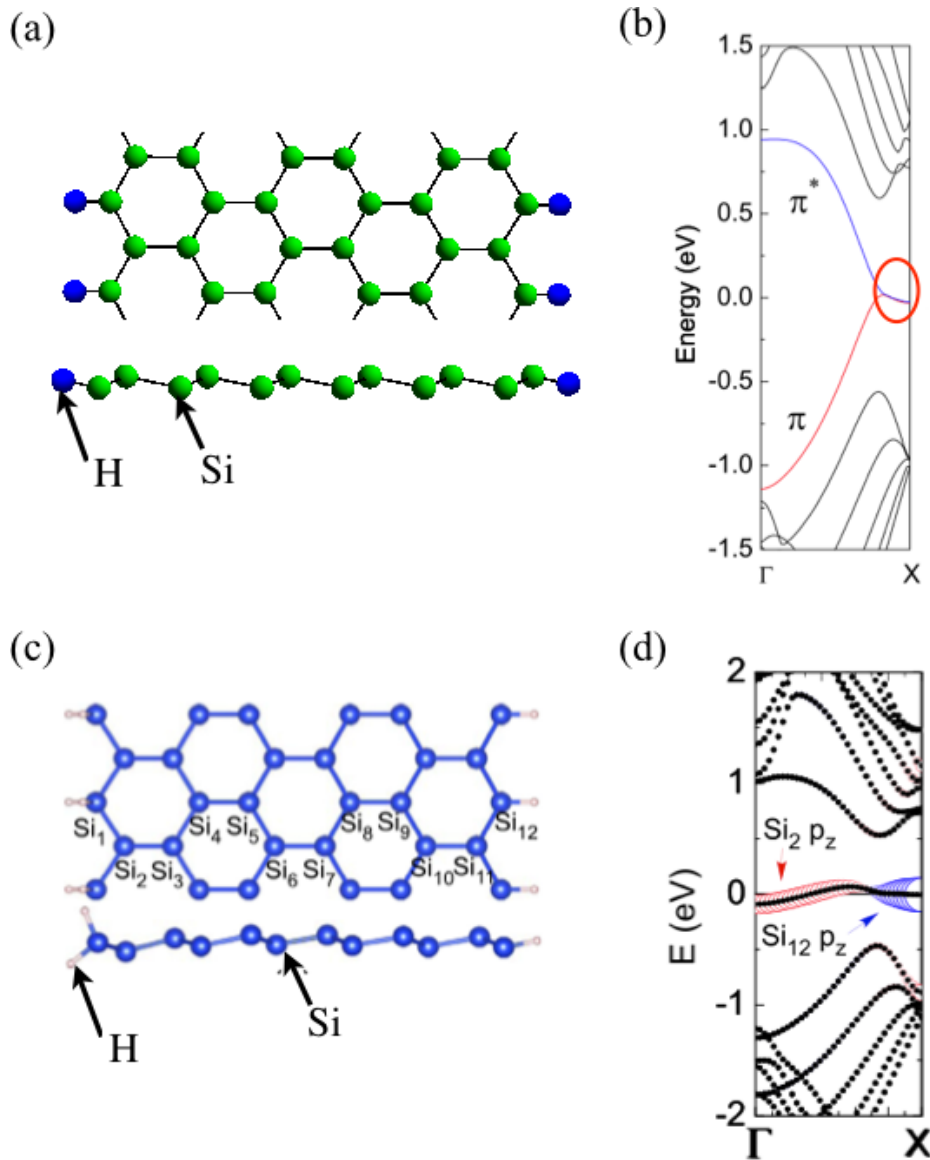
Fig. 1.21   (a) and (c) show lattice geometries of a zigzag silicene ribbon with sp^2 like hydrogen terminations in the both edges and with asymmetrical hydrogen terminations sp^2 and sp^3, respectively. Upper and lower panel show the top and side views of these silicene ribbons. In (a), green and blue spheres represent silicon and hydrogen atoms. On the other hand, in (b), blue and white spheres represent silicon and hydrogen atoms. (b) Calculated energy bands of a silicene ribbon with sp^2 like hydrogen termination[54]. (d) Calculated energy bands of a silicene ribbon with sp^2 and sp^3 like hydrogen terminations[55]. In (b), red circles indicate flat band edge states.

Chapter 2

Models and methods

2.1 Lattice geometry of silicene

A buckled structure of silicene is described by the angle θ [Fig. 2.1 (a)]. For the energetically stable structure of silicene calculated from DFT calculations, θ is $\theta = 101.73°$[23]. Moreover the three position vectors $\vec{d_1}$, $\vec{d_2}$, and $\vec{d_3}$ from a B sublattice to three nearest neighbor A sublattices are

$$\vec{d_1} = a(\sin\theta, 0, \cos\theta) \tag{2.1}$$

$$\vec{d_2} = a(\frac{-\sin\theta}{2}, \frac{\sqrt{3}\sin\theta}{2}, \cos\theta) \tag{2.2}$$

$$\vec{d_3} = a(\frac{-\sin\theta}{2}, \frac{-\sqrt{3}\sin\theta}{2}, \cos\theta), \tag{2.3}$$

where a is the lattice constant. The lattice geometries of zigzag silicene ribbons are buckled honeycomb lattices [Fig. 2.1 (b)]. In this study, we assume that the system has left and right edges with a spacing L_1 along a unit vector $\vec{e_1}$[Fig.2.1 (b)], and is imposed a periodic boundary condition along a unit vector $\vec{e_2}$ with a spacing L_2. In Fig. 2.1 (c) and (d), we show schematic figures of two types of hydrogen terminated silicene ribbons. In Fig. 2.1 (d), position vectors from B sites to two hydrogen sites $\vec{d_{H1}}$ and $\vec{d_{H2}}$ are given by

$$\vec{d_{H1}} = a_H(\sin\theta, 0, \cos\theta), \tag{2.4}$$

$$\vec{d_{H2}} = a_H(0, 0, 1), \tag{2.5}$$

where, a_H are the distance between hydrogen atoms and Si atoms. On the other hand, position vectors from A sites to two hydrogen sites $\vec{d_{H3}}$ and $\vec{d_{H4}}$ are also given by $\vec{d_{H3}} = -\vec{d_{H1}}$ and $\vec{d_{H4}} = -\vec{d_{H2}}$, respectively. Figs.2.2 and 2.3 show silicene ribbons with several types of edge terminations. Figs.2.2(a), (c) and (f) show the lattice geometries of silicene ribbons without termination(0H/0H ribbon), with a termination by single hydrogen atom at both edges(1H/1H ribbon) and by two hydrogen atoms at both edges, respectively(2H/2H ribbon). On the other hand, Figs.2.2(b), (d) and (e) show lattice geometries of silicene ribbons, terminated by single hydrogen atom at only one side edge(1H/0H ribbon), by two hydrogen atoms
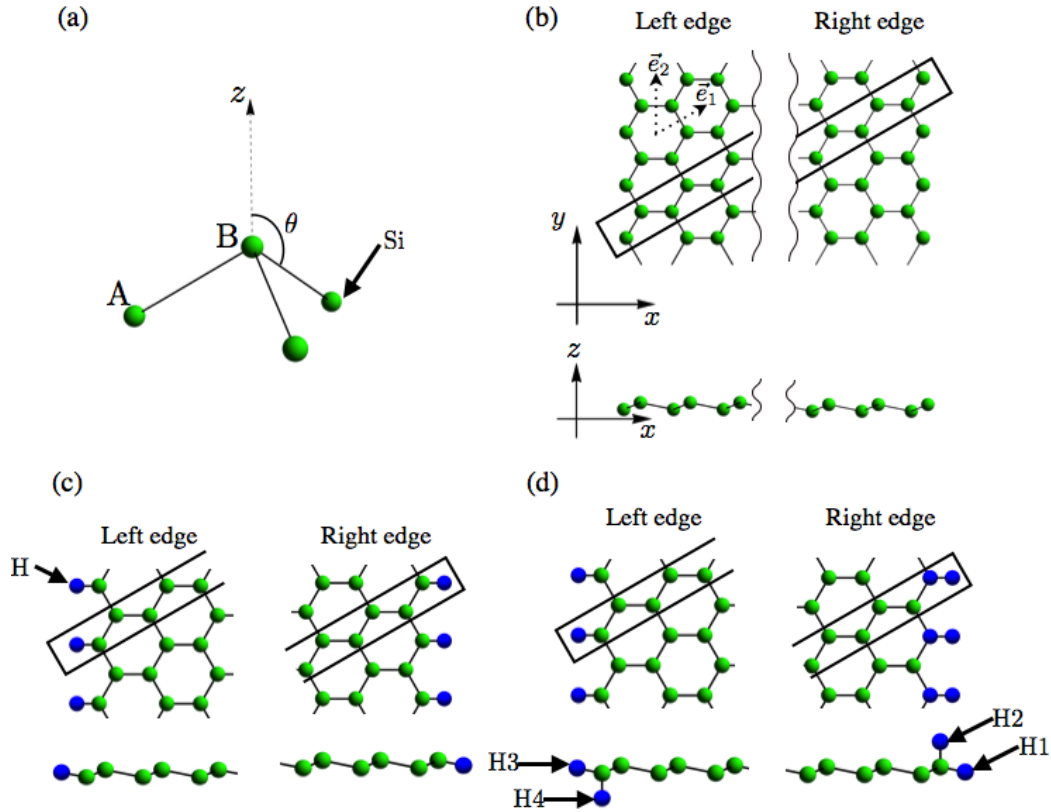
Fig. 2.1   (a) Green spheres show silicon atoms, and a bond angle θ is defined as being between the direction from a B site to a A site and the z-axes normal to the plane. Lattice geometries of silicene ribbons (b) without or (c),(d) with hydrogen terminations. In Fig.(b), above and bottom figures shows side and top of views of zigzag silicene ribbons without hydrogen termination, respectively. In this figure, a black frame represents a unit cell. In Fig.(c), above and bottom figures shows top and side of views of monohydrogenated zigzag silicene ribbons, respectively. Therefore in Fig.(d), above and bottom figures shows top and side of views of dihydrogenated zigzag silicene ribbons, respectively.

at only one side edge (2H/0H ribbon), and by two hydrogen atoms at one side edge and single hydrogen atom at another side edge (2H/1H ribbon), respectively. In addition, Figs.2.3 also show zigzag silicene ribbons with other types of hydrogen terminations.

2.2   Multi-orbital tight binding model on a honeycomb lattice

As the theoretical model of silicene, we consider a four orbitals tight binding model. These four orbitals are outer shell orbitals, and for a silicene case are
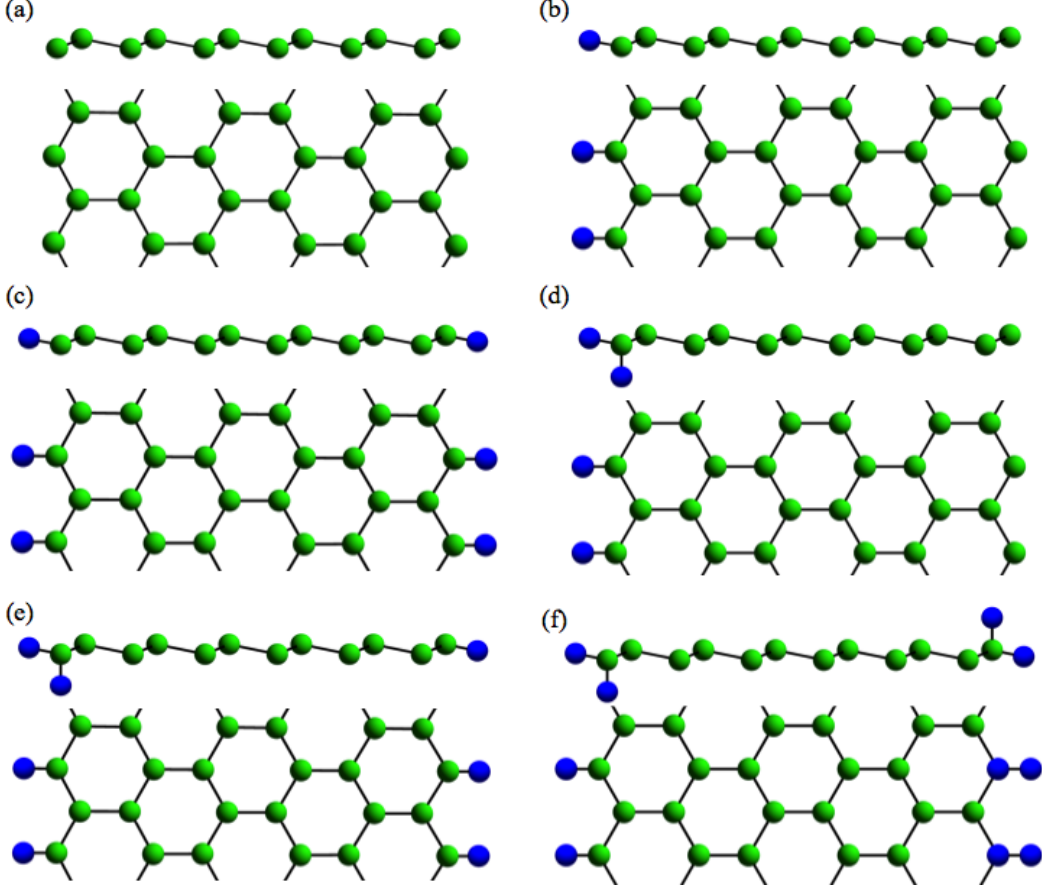
Fig. 2.2 Lattice geometries of silicene ribbons with or without several types of hydrogen terminations. In these figures, upper figures show side views of silicene ribbons, on the other hand bottom figures show top views of silicene ribbons. (a) a silicene ribbon without hydrogen termination (0H/0H ribbon). (b) a ribbon with a termination by single hydrogen atom only one side edge (1H/0H ribbon). (c) a ribbon terminated by single hydrogen atom with both edges (1H/1H ribbon). (d) a ribbon with a termination by two hydrogen atoms only one side edge (2H/0H ribbon). (e) a ribbon terminated by single hydrogen atom with one side edge and two hydrogen atoms with another side (2H/1H ribbon). (f) a ribbon terminated by two hydrogen atoms with both edges (2H/2H ribbon).

$\{3s, 3p_x, 3p_y, 3p_z\}$ orbitals. The Hamiltonian $\mathcal{H}_{tot}$ is given by

$$\mathcal{H}_{\mathrm{tot}} = \mathcal{H} + \mathcal{H}_{\mathrm{H}} \tag{2.6}$$

$$\mathcal{H} = \sum_{\langle \mathbf{i},\mathbf{j} \rangle} \sum_{\alpha,\beta} (t_{ij}^{\alpha\beta} c_{i\alpha}^{\dagger} c_{j\beta} + \mathrm{H.c.}) + \sum_{i} \sum_{\alpha} \epsilon_{\alpha} c_{i\alpha}^{\dagger} c_{i\alpha},$$

$$\mathcal{H}_{\mathrm{H}} = \sum_{\langle\langle i,j \rangle\rangle} \sum_{\alpha} t_{ij}^{s\alpha} c_{is}^{\mathrm{H}\dagger} c_{j\alpha} + \mathrm{H.c.}) + \sum_{i} \epsilon_{\mathrm{H}} c_{is}^{\mathrm{H}\dagger} c_{is}^{\mathrm{H}},$$
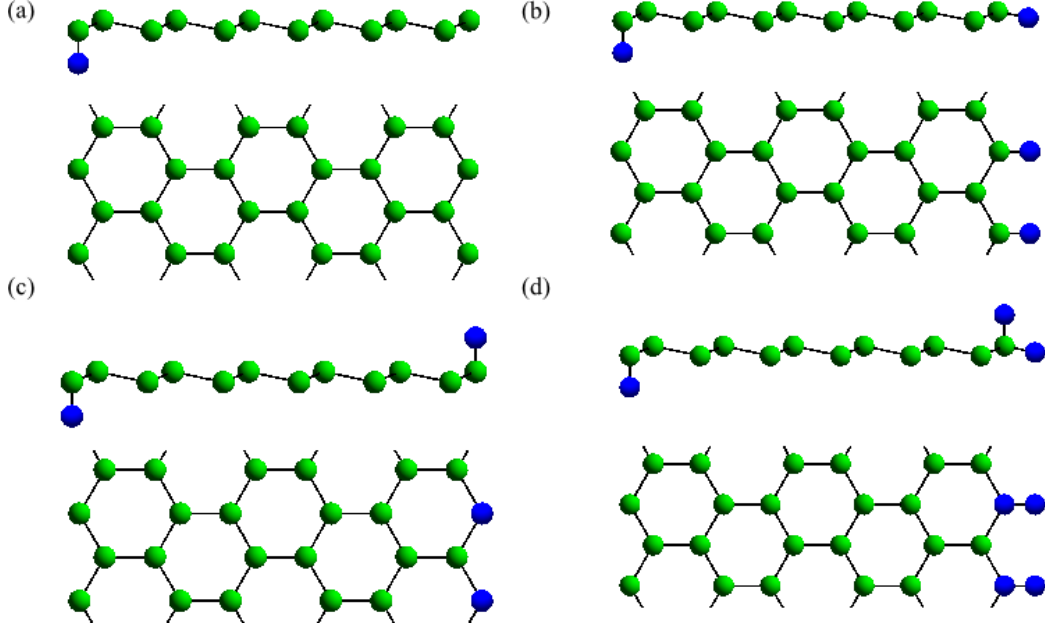
Fig. 2.3   Lattice geometries of silicene ribbons with or without several types of hydrogen terminations. In these figures, upper figures show side views of silicene ribbons, on the other hand bottom figures show top views of silicene ribbons. (a) a silicene ribbon without hydrogen termination (1H'/0H ribbon). (b) a ribbon with a termination by single hydrogen atom only one side edge (1H/1H' ribbon). (c) a ribbon terminated by single hydrogen atom with both edges (1H'/1H' ribbon). (d) a ribbon with a termination by two hydrogen atoms only one side edge (2H/1H' ribbon).

where $c_{i\alpha}^{\dagger}$ and $c_{is}^{H\dagger}$ create an electron with atomic orbital α and an electron of a hydrogen at site i respectively, $<i,j>$ run over all the nearest neighbor hopping sites, $t_{ij}^{\alpha\beta}$ is transfer energy between orbitals α and β, ϵ_{α} is an on-site energy of an orbital α, $<<i,j>>$ run over all the sites of interactions between hydrogen atoms and silicon sites at edges, and ϵ_{H} is on-site energy of hydrogen atoms. The transfer energies are given by the Slater-Koster formula [56][Table.2.1]. In Table.2.1, $V_{ss\sigma}, V_{sp\sigma}, V_{pp\sigma}$, and $V_{pp\pi}$ are the bond parameters which are given by Table. 2.2[23], and l_{ij}, m_{ij}, and n_{ij} are x, y, and z components of direction cosines from a site i to a site j, respectively [24]. In Fig.2.4, we show schematic illustration of examples of the Slator-Koster formula. As shown this figure, transfer energies $t_{ij}^{\alpha\beta}$ can be expressed as linear combinations of bond parameters. Moreover, the bond parameters of interactions with hydrogen atoms are given by Table. 2.3[57, 58, 59]. As mentioned above, we apply the periodic boundary condition along the direction $\vec{e}_2$ with a spacing L_2, and can then make a Fourier transform in that direction, $c_{i\alpha} = c_{\alpha}(\vec{i}) = L_2^{-1/2} \sum_{\vec{k}} e^{i\vec{k}\cdot\vec{i}} c_{\alpha}(\vec{k}, \vec{i'})$, where $\vec{i}$ is a position vector at site i and $\vec{i'}$ is also a position vector of a unit cell. For a case of A sites, we assume that a vector $\vec{i}$ is $\vec{i} = i_1\vec{e}_1 + i_2\vec{e}_2$, for $i_1 = 1, 2, \cdots, L_1$ and $i_2 = 1, 2, \cdots, L_2$. On the other hand for a case of B sites, a vector $\vec{i}$ is $\vec{i} = i_1\vec{e}_1 + i_2\vec{e}_2 - \vec{d}_3$. Similarly,

Table. 2.1   Slater-Koster formula

t_{ij}^{ss}	$V_{ss\sigma}$
t_{ij}^{sx}	$l_{ij}V_{sp\sigma}$
t_{ij}^{xs}	$-l_{ij}V_{sp\sigma}$
t_{ij}^{xx}	$l_{ij}^2 V_{pp\sigma} + (1 - l_{ij}^2)V_{pp\pi}$
t_{ij}^{xy}	$l_{ij}m_{ij}(V_{pp\sigma} - V_{pp\pi})$
t_{ij}^{xz}	$m_{ij}n_{ij}(V_{pp\sigma} - V_{pp\pi})$

Table. 2.2   Numerical values for computation of four orbitals tight-binding model

System	a(Å)	θ(degree)	$V_{ss\sigma}$(eV)	$V_{sp\sigma}$	$V_{pp\sigma}$	$V_{pp\pi}$	$\epsilon_s - \epsilon_p$
Graphene	1.42	90°	-6.769	5.580	5.037	-3.033	-8.868
Silicene	2.28	101.73°	-1.93	2.54	4.47	-1.12	-7.03
Silicene(sp$_3$)	2.24	109.47°	-2.052	2.697	4.749	-1.187	-6.61

Table. 2.3   Numerical values of bond parameters of Si-H and C-H bonds

System	a_H(Å)	$V_{ss\sigma}$(eV)	$V_{sp\sigma}$	ϵ_H
Graphene	1.01	-10.457	13.744	-13.65
Silicene	1.50	-4.741	6.231	-13.65

position vectors $\vec{i'}$ of A and B sites can be written as $\vec{i'} = i_1\vec{e_1}$ and $\vec{i'} = i_1\vec{e_1} - \vec{d_3}$, respectively. These expressions yield a $\vec{k}$ dependent series of one-dimensional Hamiltonian, $\mathcal{H} = \sum_{\vec{k}} \mathcal{H}^{1D}(\vec{k})$. Similarly in Eqs.(2.6), the term of interactions of hydrogen termination $\mathcal{H}_\mathrm{H}$ can be rewritten as $\mathcal{H}_\mathrm{H} = \sum_{\vec{i'}}(\mathcal{H}_{HL}^{1D} + \mathcal{H}_{HR}^{1D})$, where indexes L and R denote left and right edges respectively. The resultant eigenvalue reduces to $(\mathcal{H}^{1D}(\vec{k}) + \mathcal{H}_{HL}^{1D} + \mathcal{H}_{HR}^{1D})|\psi(\vec{k}, E)\rangle = E|\psi(\vec{k}, E)\rangle$ with corresponding eigenstates $|\psi(\vec{k}, E)\rangle$. We calculate this eigenvalue problem numerically and show energy spectra as function of wave number k.

2.3 Z_2 Berry phase as a topological quantities for a detection of edge states

As mentioned before section in Sec.1.2, topological quantities are useful for a detection and characterization of edge states. In this study, to investigate properties of edge states, we adopt not only energy spectra of silicene ribbons and its wave function but also the non-Abelian Berry phase (Zak phase) which is calculated from wave functions of bulk hamiltonian as function of a wave number k which corresponds to the translation vector of silicene ribbons. In this section, we define the non-Abelian Berry phase for a calculation of the Berry phase in multi-band systems[48, 43, 60].
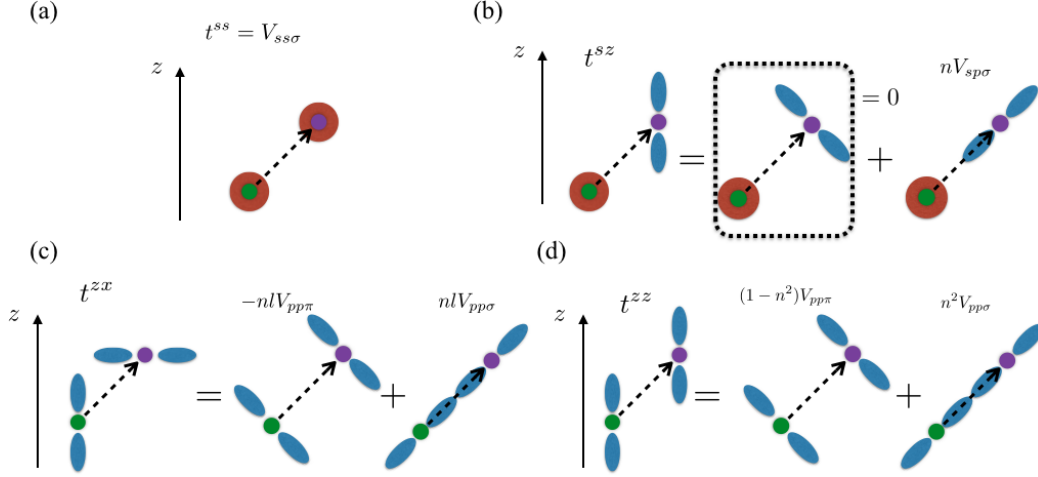
Fig. 2.4 Schematic illustration of the Slator-Koster formula for t^{SS} (a), t^{sz} (b), t^{zx} (c), and t^{zz} (d). Green and purple circles indicated two atomic sites that difference between the two sites are described by a vector $\vec{d}$ (dashed arrows). Red filled circles and blue ellipses indicate s and p orbitals, respectively. l and n represent x and z components of a direction cosine.

2.3.1   Definition of the Berry phase and its quantization for a single band

The Berry phase γ for a single band is defined as follows:

$$\gamma = -i \oint_C A(\phi)dC, \tag{2.7}$$

where $A(\phi)$ is an Abelian Berry connection, which is given by $A(\phi) = \langle \psi(\phi)|\partial_\phi|\psi(\phi)\rangle$ where $|\psi(\phi)\rangle$ is an eigen state of a parameter dependent hamiltonian $\mathcal{H}(\phi)$, and C is a closed loop in the parameter space. Here, we consider a change of a Berry phase for applying a gauge transformation $g = e^{i\Omega(\phi)}$ to $|\psi(\phi)\rangle$, then the gauge transformed Berry connection A_g can be written as follows:

$$\begin{aligned} A_g &= \langle \psi(\phi)|g^{-1}\partial_\phi(g|\psi(\phi)\rangle) \\ &= \langle \psi(\phi)|\partial_\phi|\psi(\phi)\rangle + \langle \psi(\phi)|g^{-1}\partial_\phi(g)|\psi(\phi)\rangle \\ &= A + i\frac{\partial}{\partial\phi}\Omega. \end{aligned} \tag{2.8}$$

Then, we are led to,

$$i\gamma_g = i\gamma + i \oint_L d\Omega. \tag{2.9}$$

In Eq.(2.9), we assume that the phase factor $e^{i\Omega}$ is single-valued function in the whole parameter space, then the integration $\int_L d\Omega$ is proportional to 2π. Therefore

a gauge transformed Berry phase γ_g is congruent to γ modulo 2π. Here we expand $|\psi(\phi)\rangle$ in an orthonormal system $|j\rangle$ as $|\psi(\phi)\rangle = \sum_j C_j(\phi)|j\rangle$ and operate an anti-unitary operator $\Theta = KU$ to this state, where K and U are a complex conjugate and a unitary operators, respectively. Thus, we obtain $\Theta|\psi(\phi)\rangle = \sum_j C_j^*(\phi)|j_\Theta\rangle$. Moreover, Berry connections $A(\phi)$ and $A_\Theta(\phi) = \langle\psi(\phi)|\Theta^{-1}\partial_\phi\Theta|\psi(\phi)\rangle$ are rewritten using this expressions as follows:

$$A(\phi) = (\sum_{j'}\langle j'|C_{j'}^*(\phi))\partial_\phi(\sum_j C_j(\phi)|j\rangle) = \sum_j C_j^* \frac{\partial}{\partial\phi}C_j \tag{2.10}$$

$$A_\Theta(\phi) = (\sum_{j'}\langle j'_\Theta|\Theta^{-1}C_{j'}(\phi))\partial_\phi(\sum_j C_j^*(\phi)|j_\Theta\rangle) = \sum_j C_j \frac{\partial}{\partial\phi}C_j^* \tag{2.11}$$

Since, $\sum_j |C_j|^2 = 1$, then we obtain $\sum_j \frac{\partial}{\partial\phi}|C_j|^2 = \sum_j(\frac{\partial}{\partial\phi}C_j^* C_j + C_j^* \frac{\partial}{\partial\phi}C_J) = 0$. As the result, $\sum_j C_j^* \frac{\partial}{\partial\phi}C_J = -\sum_j C_j \frac{\partial}{\partial\phi}C_J^* \rightarrow A(\phi) = -A_\Theta(\phi)$ satisfies. If a parameter dependent hamiltonian $\mathcal{H}(\phi)$ is invariant under a gauge transformation Θ and $|\psi(\phi)\rangle$ is non-degenerate, then a Berry phase is real and quantized as 0 and π modulo 2π. Because of $A(\phi) = -A_\Theta(\phi)$, Berry phases are calculated as $\gamma = -\gamma_\Theta(\mathrm{mod}\ 2\pi)$. In this case, this Berry phase called Z_2 Berry phase and this quantization is topologically protected unless a gap closing. In the next part, we mention about non-Abelian Berry phase and its quantization.

2.3.2   Definition of non-Abelian Berry phase and its quantization for multi-band systems

Here, we define the non-Abelian Berry phase for a calculation of the Berry phase in a multi-band systems. In this section we consider a non-interacting spinless fermion system with m particles as an example for the definition of non-Abelian Berry phase.

Ground state of a non-interacting spinless fermion system
Before defining a non-Abelian Berry phase, we consider the ground state of a non-interacting spinless fermion system. In this case, the ground state can be constructed by occupying energy eigen states from the lowest energy level up to an energy level. Here, we assume a single orbital tight-binding model as a hamiltonian.

$$H = \sum_{<i,j>} t_{ij}c_i^\dagger c_j + \mathrm{h.c} \tag{2.12}$$

where $c_i^\dagger(c_j)$ are creation(annihilation) operators at $i(j)$ cites, which satisfy an anti-commutation relation $\{c_i, c_j^\dagger\} = \delta_{ij}$, t_{ij} are the hopping energies between i and j sites, and $< i, j >$ mean the nearest neighbor hopping. This hamiltonian can be rewritten using an expression of matrix elements h as $H = c^\dagger h c$ where h is $m \times m$ matrix, $h_{ij} = t_{ij}$ and $c^\dagger = (c_1^\dagger, c_2^\dagger, \cdots, c_m^\dagger)$. Moreover we assume eigen states of

this hamiltonian as ψ_l which satisfy $h\psi_l = \epsilon_l\psi_l$ where ϵ_l are eigen energies. Using this eigen states ψ_l, we construct m-dimensional multiplet $\Psi_N = (\psi_1, \psi_2, \cdots, \psi_N)$ and assume $\epsilon_1 < \epsilon_2 < \cdots < \epsilon_N < E_F < \epsilon_{N+1} < \cdot < \epsilon_m$ where E_F is a Fermi energy. Therefore Ψ_N satisfies as follows:

$$h\Psi_N = h(\psi_1, \psi_2, \cdots, \psi_N) = (\psi_1, \psi_2, \cdots, \psi_N) \begin{pmatrix} \epsilon_1 & & \\ & \ddots & \\ & & \epsilon_N \end{pmatrix} = \Psi_N \mathcal{E}. \quad (2.13)$$

Since ψ_l are orthonormal then

$$\Psi_N^\dagger \Psi_N = \begin{pmatrix} \psi_1^\dagger \\ \psi_2^\dagger \\ \vdots \\ \psi_N^\dagger \end{pmatrix} (\psi_1, \psi_2, \cdots, \psi_N) = \begin{pmatrix} \psi_1^\dagger\psi_1 & \psi_1^\dagger\psi_2 & \cdots & \psi_1^\dagger\psi_N \\ \psi_2^\dagger\psi_1 & \psi_2^\dagger\psi_2 & \cdots & \psi_2^\dagger\psi_N \\ \vdots & \vdots & \ddots & \vdots \\ \psi_N^\dagger\psi_1 & \psi_N^\dagger\psi_2 & \cdots & \psi_N^\dagger\psi_N \end{pmatrix} = E_N,$$

$$(2.14)$$

$$\Rightarrow \Psi_N \Psi_N^\dagger = E_N$$

where E_N is an $N \times N$ identity matrix. From Eqs.(2.13) and (2.15), we can obtain $h = \Psi_N \mathcal{E} \Psi_N^\dagger$ and $H = c^\dagger h c = c^\dagger \Psi_N \mathcal{E} \Psi_N^\dagger c = d^\dagger \mathcal{E} d = \sum_l^N d^\dagger \epsilon_l d_l$, where $d^\dagger = c^\dagger \Psi_N$ and $d_l = c^\dagger \psi_l$. $d_l^\dagger$ (d_l) are creation (annihilation) operators of eigen states with energy ϵ_l and satisfy anti-commutation relation$\{d_i, d_j^\dagger\} = \delta_{ij}$ [1]. Then we can rewrite an N-dimensional multiplet Ψ_N using $d_l^\dagger$ as $|\Psi_N\rangle = d_1^\dagger d_2^\dagger \cdots d_N^\dagger |0\rangle = \prod_{l=1}^N d_l^\dagger |0\rangle$

Definition of non-Abelian Berry phase
Using N-dimensional multiplet $|\Psi_N\rangle$ derived in previous section, we define the Berry phase γ as follows:

$$\gamma = -i \oint_L \langle \Psi_N | d\Psi_N \rangle. \quad (2.15)$$

$\langle \Psi_N | d\Psi_N \rangle$ can be expand as follow:

$$\langle \Psi_N | d\Psi_N \rangle = \langle 0| d_N \cdots d_2 d_1 (c^\dagger d\psi_1) d_2^\dagger \cdots d_N^\dagger |0\rangle + \langle 0| d_N \cdots d_2 d_1 d_1^\dagger (c^\dagger d\psi_2) \cdots d_N^\dagger |0\rangle + \cdots .$$

$$(2.16)$$

---

[1]

$$\{d_i, d_j^\dagger\} = \{\psi_i^\dagger c, c^\dagger \psi_j\} = \{\psi_{i1}^\dagger c_1, c^\dagger \psi_j\} + \{\psi_{i2}^\dagger c_2, c^\dagger \psi_j\} + \cdots + \{\psi_{iN}^\dagger c_N, c^\dagger \psi_j\}$$

$$= \psi_{i1}^\dagger \{c_1, c^\dagger \psi_j\} + \psi_{i2}^\dagger \{c_2, c^\dagger \psi_j\} + \cdots + \psi_{iN}^\dagger \{c_N, c^\dagger \psi_j\}$$

$$= \psi_{i1}^\dagger \psi_{j1} \{c_1, c_1^\dagger\} + \psi_{i2}^\dagger \psi_{j2} \{c_2, c_2^\dagger\} + \cdots + \psi_{iN}^\dagger \psi_{jN} \{c_N, c_N^\dagger\}$$

$$= \psi_{i1}^\dagger \psi_{j1} + \psi_{i2}^\dagger \psi_{j2} + \cdots + \psi_{iN}^\dagger \psi_{jN} = \psi_i^\dagger \psi_j = \delta_{ij}$$

$d_1(c^\dagger d\psi_1)$ in the first term of the right hand side of Eq.(2.16), can be leads to

$$d_1(c^\dagger d\psi_1) = (\psi_1^\dagger c)(c^\dagger d\psi_1) = \sum_{a,b=1}^{N} \psi_{1a} d\psi_{1b}^\dagger c_a c_b^\dagger = \sum_{a,b=1}^{N} \psi_{1a} d\psi_{1b}^\dagger (\delta_{ab} - c_a^\dagger c_b)$$

$$= \psi_1 d\psi_1^\dagger - d_1^\dagger (d\psi_1^\dagger c). \tag{2.17}$$

Thus, we obtain $\langle 0|d_N \cdots d_2 d_1(c^\dagger d\psi_1)d_2^\dagger \cdots d_N^\dagger|0\rangle = \psi_1 d\psi_1^\dagger \langle 0|d_N \cdots d_2 d_2^\dagger \cdots d_N^\dagger|0\rangle - \langle 0|d_N \cdots d_2 d_1^\dagger (d\psi_1^\dagger c)d_2^\dagger \cdots d_N^\dagger|0\rangle = \psi_1 d\psi_1^\dagger$. Moreover we can obtain similar terms for other terms of the right hand side of Eq.(2.16). Then we obtain

$$\langle \Psi_N | d\Psi_N \rangle = \psi_1 d\psi_1^\dagger + \psi_2 d\psi_2^\dagger + \cdots + \psi_N d\psi_N^\dagger. \tag{2.18}$$

Here, we consider m-dimensional multiplet $\Psi = (\psi_1, \psi_2, \cdots, \psi_m)$ where Ψ satisfies $\Psi^\dagger \Psi = E_m$. Then we define non-Abelian Berry connection A as follows:

$$A = \Psi^\dagger d\Psi = \begin{pmatrix} \psi_1^\dagger d\psi_1 & \psi_1^\dagger d\psi_2 & \cdots & \psi_1^\dagger d\psi_m \\ \psi_2^\dagger d\psi_1 & \psi_2^\dagger d\psi_2 & \cdots & \psi_2^\dagger d\psi_m \\ \vdots & \vdots & \ddots & \vdots \\ \psi_m^\dagger d\psi_1 & \psi_m^\dagger d\psi_2 & \cdots & \psi_m^\dagger d\psi_m \end{pmatrix}. \tag{2.19}$$

If we take a diagonal sum of this Berry connection, then this is identical to $\langle \Psi_N | d\Psi_N \rangle$, thus we obtain

$$\gamma = -i \oint_L \langle \Psi_N | d\Psi_N \rangle = -i \oint_L \mathrm{Tr}A \tag{2.20}$$

Gauge transformation of the non-Abelian Berry connection
Next, we consider a gauge transformation of the non-Abelian Berry connection and the Berry phase. Here we assume that a gauge transformation $\omega \in U(m)$ relates to Ψ as $\Psi = \Psi'\omega$ and is a single-valued in $U(m)$. Since ω is unitary ($\omega^\dagger = \omega^{-1}$), and Berry connection can be rewritten as follows:

$$A = \Psi^\dagger d\Psi = (\omega^\dagger(\Psi^{\dagger\prime}))d(\Psi'\omega) = \omega^{-1}(\Psi^{\dagger\prime})(d\Psi'\omega + \Psi'd\omega) = \omega^{-1}\Psi^{\dagger\prime}d\Psi'\omega + \omega^{-1}d\omega. \tag{2.21}$$

From Eq.(2.21), we are led to.

$$\mathrm{Tr}A = \mathrm{Tr}(\omega^{-1}\Psi^{\dagger\prime}d\Psi'\omega) + \mathrm{Tr}(\omega^{-1}d\omega) = \mathrm{Tr}(\Psi^{\dagger\prime}d\Psi') + \mathrm{Tr}(\omega^{-1}d\omega) = \mathrm{Tr}A' + \mathrm{Tr}(\omega^{-1}d\omega), \tag{2.22}$$

where we substitute A' for $\Psi^{\dagger\prime}d\Psi'$. Then the Berry phase γ is rewritten as follows:

$$\gamma = -i \oint_L \mathrm{Tr}A = -i \oint_L A' - i \oint_L \mathrm{Tr}(\omega^{-1}d\omega) = \gamma - i \oint_L \mathrm{Tr}(\omega^{-1}d\omega), \tag{2.23}$$

where $\oint_L \mathrm{Tr}(\omega^{-1}d\omega)$ is proportional to the integral multiple of 2π [*2].

[*2] Since ω is a unitary matrix, ω can be diagonalized. Then we assume a diagonal matrix Ω which is digonalized from ω by a transformation matrix U as $\Omega = U^{-1}\omega U$. Thus, Ω

Quantization of the non-Abelian Berry phase

Here we show that the non-Abelian Berry phase quantizes for the hamiltonian which possess the time reversal symmetry which contains the complex conjugate operator. We define the anti-unitary operator $\Theta = KU$ where K and U are a complex conjugate and a unitary operator, respectively. Next, we assume M-dimensional multiplet $\Psi = (|\psi_1\rangle, |\psi_2\rangle, \cdots, |\psi_M\rangle)$ and Ψ_Θ which Θ operated. Then the Berry connection A_Θ calculated form Ψ_Θ is led to

$$A_\Theta = (\Psi_\Theta)^\dagger d\Psi_\Theta = (\Psi^\dagger)^*(U^\dagger U)^*(d\Psi)^* = (\Psi^\dagger d\Psi)^* = A^*. \qquad (2.24)$$

Since $\Psi^\dagger \Psi = E_M \Rightarrow (d\Psi^\dagger)\Psi + \Psi^\dagger d\Psi = 0$, then we obtain

$$\mathrm{Tr}A^* = \mathrm{Tr}A^\dagger = \mathrm{Tr}(\Psi^\dagger d\Psi)^\dagger = \mathrm{Tr}(d\Psi^\dagger \Psi) = -\mathrm{Tr}A. \qquad (2.25)$$

Therefore, Berry phase γ_Θ is $\gamma_\Theta = -\gamma$. If the multiplet Ψ is gapped, and Ψ_Θ and Ψ are linked by a gauge transformation ω then Ψ_Θ can be expressed as $\Psi_\Theta = \Psi\omega$. In this case, the Berry phase has ambiguities of 2π and quantizes as $\gamma = 0, \pi \pmod{2\pi}$.

2.3.3   Discretized non-Abelian Berry phase for numerical calculations

In this subsection, we mention about the discretized non-Abelian Berry phase for numerical calculations. Firstly we discretize a closed loop $L(L = \{x(t)|t \in [0,1], x(0) = x(1)\})$ in the parameter space as $x_n = x(n\Delta t)(n = \{1, 2, \cdots, N_L\}\Delta t = 1/N_L)$ where N_L is a number of this discretization. Here we define non-Abelian Berry phase in this discretized parameter space as follows:

$$\gamma_L = \arg \det[(\Psi_1^\dagger \Psi_2)(\Psi_2^\dagger \Psi_3)\cdots(\Psi_{N_L-1}^\dagger \Psi_{N_L})]. \qquad (2.26)$$

---

satisfies following equation.

$$\begin{pmatrix} d\log\lambda_1 & & \\ & \ddots & \\ & & d\log\lambda_m \end{pmatrix} = \begin{pmatrix} \frac{d\lambda_1}{\lambda_1} & & \\ & \ddots & \\ & & \frac{d\lambda_m}{\lambda_m} \end{pmatrix} = \Omega^{-1}d\Omega.$$

Besides, $\mathrm{Tr}(\omega^{-1}d\omega)$ can be led to

$$\mathrm{Tr}(\omega^{-1}d\omega) = \mathrm{Tr}((U^{-1}\Omega U)^{-1}d(U^{-1}\Omega U)) = \mathrm{Tr}(U\Omega^{-1}U^{-1}\{dU^{-1}\Omega U + U^{-1}d\Omega U + U^{-1}\Omega dU\})$$
$$= \mathrm{Tr}(\Omega^{-1}d\Omega) + \mathrm{Tr}(UdU^{-1} + U^{-1}dU).$$

In this equation, because of $U^{-1}U = E_m$ and $dU^{-1}U + U^{-1}dU = 0$, the second term is 0. Finally we obtain $\mathrm{Tr}\omega^{-1}d\omega = \mathrm{Tr}\Omega^{-1}d\Omega = \mathrm{Tr}d\log\Omega = d\mathrm{Tr}\log\Omega$. On the other hand, because of $\mathrm{Tr}\log\Omega = \log\lambda_1 + \log\lambda_2 + \cdots = \log\lambda_m = \log(\lambda_1\lambda_2\cdots\lambda_m) = \log\det\Omega$ then we obtain $\mathrm{Tr}\omega^{-1}d\omega = d\log\det\Omega$. Since ω is a unitary matrix, $\det\omega$ satisfies $|\det\omega| = 1$. Thus we assume $\det\omega = e^{i\theta}$ then $-i\oint_L \mathrm{Tr}\omega^{-1}d\omega = -i\oint_L id\theta = \oint_L d\theta$. Furthermore, the Berry phase can be $\gamma = \gamma' + 2\pi n(n \in Z) = \gamma'(\mathrm{mod}\ 2\pi)$.

This expression of the Berry phase is obviously invariant under the gauge transformation in the term of previous sections. In the following part, we show that Eq.(2.26) is identical to $\gamma = -i \oint_L \mathrm{Tr}\Psi^\dagger d\Psi$ in the continuous limit $N_L \to \infty$. γ_L can be rewritten as follows:

$$\gamma_L = \arg \det[(\Psi_1^\dagger \Psi_2)(\Psi_2^\dagger \Psi_3)\cdots(\Psi_{N_L-1}^\dagger \Psi_{N_L})] = \mathrm{Im} \log \det[(\Psi_1^\dagger \Psi_2)(\Psi_2^\dagger \Psi_3)\cdots(\Psi_{N_L-1}^\dagger \Psi_{N_L})]$$

$$= \mathrm{Im} \log[\ \det(\Psi_1^\dagger \Psi_2)\det(\Psi_2^\dagger \Psi_3)\cdots\det(\Psi_{N_L-1}^\dagger \Psi_{N_L})]$$

$$= \mathrm{Im}[\log \det(\Psi_1^\dagger \Psi_2) + \log \det(\Psi_2^\dagger \Psi_3) + \cdots + \log \det(\Psi_{N_L-1}^\dagger \Psi_{N_L})]. \qquad (2.27)$$

Here we assume $\Delta t << 1$ then, $\Psi_l^\dagger \Psi_{l+1}$ can be expanded as $\Psi_l^\dagger \Psi_{l+1} \sim \Psi_l^\dagger(\Psi_l + \Delta t \partial_t \Psi_l) = E_M + \Delta t \Psi_l^\dagger \partial_t \Psi_l$. Generally, Ψ_l is not a diagonalizable matrix but a norm of this matrix satisfies a following equation:

$$||\Psi_l^\dagger \Psi_{l+1} - E_M|| \sim ||E_M + \Delta t \Psi_l^\dagger \partial_t \Psi_l - E_M|| = ||\Delta t \Psi_l^\dagger \partial_t \Psi_l|| = \Delta t ||\Psi_l^\dagger \partial_t \Psi_l|| << 1. \qquad (2.28)$$

Thus we can use the relation $\log \det \Psi_l^\dagger \Psi_{l+1} = \mathrm{Tr} \log \Psi_l^\dagger \Psi_{l+1}$ [*3]. Besides, the definition of exponential of matrix A is given by $e^A = E + A + (1/2)A^2 + (1/3!)A^3 + \cdots$, then we obtain

$$\Psi_l^\dagger \Psi_{l+1} \sim E_M + \Delta t \Psi_l^\dagger \partial_t \Psi_l \sim e^{\Delta t \Psi_l^\dagger \partial_t \Psi_l}. \qquad (2.29)$$

[*3]   If a $n \times n$ matrix M is a diagonalizable matrix then $\log \det M = \mathrm{Tr} \log M$ obviously satisfies. However, when M is not a diagonalizable matrix, then we have to consider from a definition of $\log M$ using the Taylor expansion. Definitions of $\log M$ and e^M are given by $\log M = \sum_{m=0}^\infty \frac{(-1)^{m-1}}{m}(M-E)^m$ and $e^M = \sum_{m=1}^\infty \frac{M^m}{m!}$ where E is an $n \times n$ identity matrix. Generally, the infinite series of e^M converges, but one of $\log M$ does not converge unless a norm of matrix $||M-E||$ satisfies $||M-E|| < 1$ in other words the eigen values of $M - E$ are smaller than one. In this case, $\log M$ can not be defined. Here we assume that $\log M$ can be defined. Thus we obtain $e^M x_i = \sum_{m=0}^\infty \frac{M^m}{m!}x_i^m = e^\lambda x_i$ where λ_i and x_i are eigen values and vectors of $M(i = 1, 2, \cdots, n)$, respectively. If U is $U = (x_1, x_2, \cdots, x_n)$, then we obtain,

$$e^M U = U \begin{pmatrix} e^{\lambda_1} & & & \\ & e^{\lambda_2} & & \\ & & \ddots & \\ & & & e^{\lambda_n} \end{pmatrix} \Rightarrow e^M = U \begin{pmatrix} e^{\lambda_1} & & & \\ & e^{\lambda_2} & & \\ & & \ddots & \\ & & & e^{\lambda_n} \end{pmatrix} U^{-1}$$

. Moreover, $\det(e^M)$ and M are $\det(e^M) = (\det U)e^{\lambda_1+\lambda_2+\cdots+\lambda_n}(\det U^{-1})$ and $M = U\mathrm{diag}(\lambda_1 + \lambda_2 + \cdots + \lambda_n)U^{-1}$. Therefore, we can get $\mathrm{Tr} M = \lambda_1 + \lambda_2 + \cdots + \lambda_n$ and $\det e^M = (\det U)e^{\lambda_1+\lambda_2+\cdots+\lambda_n}(\det U^{-1})=e^{\mathrm{Tr}M}$ where we use $(\det U)(\det U^{-1}) = 1$, respectively. Furthermore, we consider as $e^M M'$ and $M \to \log M'$, then $\det M' = e^{\mathrm{Tr} \log M'}$. Taking the logarithim of this equation, we can get

$$\log \det M' = \mathrm{Tr} \log M'$$

Summarizing the above,

$$
\begin{aligned}
\gamma_L &= \mathrm{Im}[\log \det(\Psi_1^\dagger \Psi_2) + \log \det(\Psi_2^\dagger \Psi_3) + \cdots + \log \det(\Psi_{N_L-1}^\dagger \Psi_{N_L})] \\
&= \mathrm{Im}[\mathrm{Tr}\,\log e^{\Delta t \Psi_1^\dagger \partial_t \Psi_1} + \mathrm{Tr}\,\log e^{\Delta t \Psi_2^\dagger \partial_t \Psi_2} + \cdots + \mathrm{Tr}\,\log e^{\Delta t \Psi_{N_L-1}^\dagger \partial_t \Psi_{N_L-1}}] \\
&= \mathrm{Im} \sum_l \mathrm{Tr}\,\Delta t \Psi_l^\dagger \partial_t \Psi_l.
\end{aligned}
\tag{2.30}
$$

In the limit of $N_L \to \infty$, the summation of this equation becomes an integral, then

$$
\lim_{\Delta t \to 0} \gamma_L = \mathrm{Im} \lim_{\Delta t \to 0} \sum_l \mathrm{Tr}\,\Delta t \Psi_l^\dagger \partial_t \Psi_l = \mathrm{Im} \int dt \mathrm{Tr}\,\Psi^\dagger \partial_t \Psi = \mathrm{Im} \oint_L \mathrm{Tr}\,\Psi^\dagger \partial_t \Psi = \mathrm{Im}(i\gamma) = \gamma.
\tag{2.31}
$$

Moreover, we can also show the quantization of this Berry phase and a Berry phase γ_Θ calculated from a multiplet Ψ_Θ which is operated by an anti-unitary operator $\Theta = KU$, is given by as follows:

$$
\begin{aligned}
\gamma_\Theta &= \arg \det[(\Psi_{\Theta 1}^\dagger \Psi_{\Theta 2}) \cdots (\Psi_{\Theta N_L-1}^\dagger \Psi_{\Theta N_L})] = \arg \det[(\Psi_1^\dagger \Psi_2)^* \cdots (\Psi_{N_L-1}^\dagger \Psi_{N_L})^*] \\
&= \arg \det[(\Psi_1^\dagger \Psi_2) \cdots (\Psi_{N_L-1}^\dagger \Psi_{N_L})]^* = -\arg \det[(\Psi_1^\dagger \Psi_2) \cdots (\Psi_{N_L-1}^\dagger \Psi_{N_L}) = -\gamma_L.
\end{aligned}
\tag{2.32}
$$

Because of the ambiguity of argument of 2π, the Berry phase γ_L is quantized as $\gamma_L = 0, \pi (\mathrm{mod}\ 2\pi)$.

2.3.4 Z_2 Berry phase and the chiral symmetry

In this subsection, we consider about a relation between the chiral symmetry and Z_2 Berry phase.

The chiral symmetry
In a tight-binding model, if we only consider nearest neighbor hopping, then this hamiltonian possess the chiral symmetry. In this case, we assume that a system is divided into two sublattices A and B. Then the chiral operator Γ is defined as $\{\mathcal{H}, \Gamma\} = 0$, $\Gamma^2 = 1$, $(\Gamma c_A \Gamma^{-1} = c_A, \ \Gamma c_A^\dagger \Gamma^{-1} = c_A^\dagger, \ \Gamma c_B \Gamma^{-1} = -c_B, \ \Gamma c_B^\dagger \Gamma^{-1} = -c_B^\dagger)$, that is, this means that wave functions at B sublattices is multipled by -1. Here we consider that a chairal operator Γ operates to an eigen value problem $\mathcal{H}\psi_l = \epsilon_l \psi_l$ from left side as follows:

$$
\Gamma \mathcal{H} \Gamma^{-1} \Gamma \psi_l = \epsilon_l \Gamma \psi_l \Rightarrow \mathcal{H} \Gamma \psi_l = -\epsilon_l \Gamma \psi_l,
\tag{2.33}
$$

where ψ_l and ϵ_l are eigen function and value of $\mathcal{H}$, respectively, and we use an anti-commutation relation $\{\mathcal{H}, \Gamma\} = 0$. Therefore, for a system with the chiral symmetry, $-\epsilon_l$ and $\Gamma \psi_l$ are also eigen value and function.

Particle-hole symmetry

To consider the quantization of non-Abelian Berry phase, we consider the tight-binding model for a free fermion system and its hamiltonian H is given as $H = -\sum_{<i,j>} t_{ij} c_i^\dagger c_j + h.c.$. Next we introduce the periodic parameter ϕ for a calculation of Berry phase as follows:

$$t_{ij} = \begin{cases} te^{i\phi} & (i = I, j = J) \\ t & (i \neq I, j \neq J), \end{cases} \tag{2.34}$$

where t is real , and $I(J)$ corresponds to a specific site. This parametrization means that a phase factor $e^{i\phi}$ is introduced to a specific link of hopping. Additionally, when parametrized hamiltonian $H(\phi)$ possess the chiral symmetry, then it is possible to prove that $H(\phi)$ is anti-unitary invariant by Θ_P, which is the operator of particle-hole transformation [43]. Θ_P is defined as follows

$$\Theta_P = KU_P, \quad U_P = \prod_{j=1}^{N}, \qquad \xi_j = \begin{cases} \xi_{j+} = c_j + c_j^\dagger & (\forall j \in A) \\ \xi_{j-} = -i(c_j - c_j^\dagger) & (\forall j \in B), \end{cases} \tag{2.35}$$

where, K is the complex conjugate operator ($K^2 = 1$), A and B indicate two kinds of sublattices, and N is the number of whole states. Additionally, $\xi_j = \xi_j^\dagger$. Using the anti-commutation relation, it can be proved that $\xi_j^2 = 1$ [*4]. Therefore, it leads to $\Theta_P^2 = 1$. In order to show that $H(\phi)$ is commutative with Θ_p, we consider the transformation of creation and annihilation operators $c_j^\dagger$ and c_j by U_p. To do this, we consider anti-commutation relations of $c_j^\dagger$ and c_j with ξ_j. These relations can be obtained as follows:

$$\{\xi_i, c_j\} = \{\xi_i^\dagger, c_j\} = \begin{cases} \{(c_i + c_i^\dagger), c_j\} = \{c_i^\dagger, c_j\} = \delta_{ij} & (\forall i \in A) \\ \{-i(c_i - c_i^\dagger), c_j\} = i\{c_i^\dagger, c_j\} = i\delta_{ij} & (\forall i \in B), \end{cases}$$

$$\{\xi_i, c_j^\dagger\} = \{\xi_i^\dagger, c_j^\dagger\} = \begin{cases} \delta_{ij} & (\forall i \in A) \\ -i\delta_{ij} & (\forall i \in B) \end{cases}. \tag{2.36}$$

---

*4

$$\xi_j^2 = \begin{cases} (c_j + c_j^\dagger)(c_j + c_j^\dagger) = c_j c_j^\dagger + c_j^\dagger c_j = 1 & (\forall j \in A) \\ -(c_j - c_j^\dagger)(c_j - c_j^\dagger) = -(-c_j c_j^\dagger - c_j^\dagger c_j = 1 & (\forall j \in B) \end{cases}$$

Using relations, we can get

$$\xi_i c_j \xi_i^\dagger = \begin{cases} (-c_j \xi_i)\xi_i^\dagger = -c_j & (i \neq j) \\ (1 - c_j \xi_i)\xi_i^\dagger = \xi_i^\dagger - c_j = c_j^\dagger & (i = j, \ \forall i \in A) \\ (i - c_j \xi_i)\xi_i^\dagger = i\xi_i^\dagger - c_j = -c_j^\dagger & (i = j, \ \forall i \in B) \end{cases}$$

$$\xi_i c_j^\dagger \xi_i^\dagger = \begin{cases} (-c_j^\dagger \xi_i)\xi_i^\dagger = -c_j^\dagger & (i \neq j) \\ (1 - c_j^\dagger \xi_i)\xi_i^\dagger = \xi_i^\dagger - c_j^\dagger = c_j & (i = j, \ \forall i \in A) \\ (i - c_j^\dagger \xi_i)\xi_i^\dagger = i\xi_i^\dagger - c_j^\dagger = -c_j & (i = j, \ \forall i \in B). \end{cases} \tag{2.37}$$

Thus, we are led to

$$\begin{aligned} U_p c_j U_p^\dagger &= \xi_1 \cdots \xi_N c_j \xi_N^\dagger \cdots \xi_1^\dagger = \xi_1 \cdots \xi_{N-1}(-c_j)\xi_{N-1}^\dagger \cdots \xi_1^\dagger \\ &= (-1)^{N-j}\xi_1 \cdots \xi_j c_j \xi_j^\dagger \cdots \xi_1^\dagger \\ &= \begin{cases} (-1)^{N-j}\xi_1 \cdots \xi_{j-1} c_j^\dagger \xi_{j-1}^\dagger \cdots \xi_1^\dagger = (-1)^{N-1}c_j^\dagger & (i = j, \ \forall i \in A) \\ (-1)^{N-j}\xi_1 \cdots \xi_{j-1}(-c_j^\dagger)\xi_{j-1}^\dagger \cdots \xi_1^\dagger = (-1)^N c_j^\dagger & (i = j, \ \forall i \in B) \end{cases}. \end{aligned} \tag{2.38}$$

Similarly,

$$U_p c_j^\dagger U_p^\dagger = \begin{cases} (-1)^{N-1}c_j & (i = j, \ \forall i \in A) \\ (-1)^N c_j & (i = j, \ \forall i \in B) \end{cases}. \tag{2.39}$$

For the chiral symmetric system, its hamiltonian is only consisted of hopping terms between A and B sublattices. Then hamiltonian can be transformed by U_p as follows:

$$\begin{aligned} U_p H U_p^\dagger &= -\sum_{<i,j>} t_{ij} U_p c_i^\dagger U_p^\dagger U_p c_j U_p^\dagger - \sum_{<i,j>} t_{ij}^* U_p c_j^\dagger U_p^\dagger U_p c_i U_p^\dagger \\ &= -\sum_{<i,j>} t_{ij}(-1)^{2N-1}c_i c_j^\dagger - \sum_{ij} t_{ij}^*(-1)^{2N-1}c_j c_i^\dagger \\ &= -\sum_{<i,j>} t_{ij}c_j^\dagger c_i - \sum_{ij} t_{ij}^* c_i^\dagger c_j \end{aligned} \tag{2.40}$$

Taking the complex conjugation on this equation, we can calculate $\Theta_P H \Theta_p^{-1}$ as follows:

$$\Theta_P H \Theta_p^{-1} = -\sum_{<i,j>} t_{ij}c_i^\dagger c_j - \sum_{<i,j>} t_{ij}^* c_j^\dagger c_i = H. \tag{2.41}$$

Thus, this hamiltonian is invariant against the anti-unitary transformation. When we apply the particle-hole transformation against the M-particle ground state $|G_M\rangle$, which is occupied from low energy, then this state is transformed to the $(N-M)$-particle unoccupied state $|G_{N-M}\rangle$. For the cases of $M \neq N/2$, $|G_M\rangle$ and $|G_{N-M}\rangle$ degenerate. For the case of $M = N/2$(half-filled), $|G_M\rangle$ does not degenerate. Moreover, when the excited energy is finite, then the Berry phase calculated from the chiral symmetric model quantizes as 0 and π modulo 2π.

Z_2 Berry phase in a system with the chiral symmetry

For a hamiltonian $\mathcal{H} = c^{\dagger \prime} h c'$ with the chiral symmetry, h can be written as follows:

$$h = \begin{pmatrix} O & q \\ q^{\dagger} & O \end{pmatrix} \tag{2.42}$$

where, h is a $2n \times 2n$ matrix, O is a $n \times n$ zero matrix, q is an arbitrary matrix, and $c^{\dagger \prime} = (c_{A1}^{\dagger}, c_{A2}^{\dagger}, \cdots, c_{An}^{\dagger}, c_{B1}^{\dagger}, \cdots, c_{Bn}^{\dagger})$. Taking a simple form of the chiral operator $\Gamma = \mathrm{diag}(I, -I)$ where I is an n-dimensional identity matrix, h satisfies $\{h, \Gamma\} = 0$. Here, we consider the Berry phase calculated from an N-dimensional multiplet which is constructed by occupying N states from lower energy. In particular, using N-dimensional multiplet $\Psi = (\psi_1, \cdots, \psi_N)$ constructed from normalized eigen states ψ_i of h ($h\psi_i = \epsilon_i \psi_i$, $\epsilon_i < 0$, $i = 1, \cdots, N$), the Berry phase γ is defined as follows:

$$\gamma = -i \int \mathrm{Tr} A, \qquad A = \begin{pmatrix} \psi_1^{\dagger} d\psi_1 & \psi_1^{\dagger} d\psi_2 & \cdots & \psi_1^{\dagger} d\psi_N \\ \psi_2^{\dagger} d\psi_1 & \psi_2^{\dagger} d\psi_2 & \cdots & \psi_2^{\dagger} d\psi_N \\ \vdots & \vdots & \ddots & \vdots \\ \psi_N^{\dagger} d\psi_1 & \psi_N^{\dagger} d\psi_2 & \cdots & \psi_N^{\dagger} d\psi_N \end{pmatrix}. \tag{2.43}$$

Moreover, Ψ can be expressed using $n \times n$ matrices ψ_A and ψ_B as $\Psi = \begin{pmatrix} \psi_A \\ \psi_B \end{pmatrix} / \sqrt{2}$. Using this expression, the Schrödinger equation $h\Psi = \Psi\mathcal{E}$ ($\mathcal{E} = \mathrm{diag}(\epsilon_1, \cdots, \epsilon_N)$) is rewritten as $\begin{pmatrix} O & q \\ q^{\dagger} & O \end{pmatrix} \begin{pmatrix} \psi_A \\ \psi_B \end{pmatrix} = \begin{pmatrix} \psi_A \\ \psi_B \end{pmatrix} \mathcal{E}$. Therefore, we obtain $q\psi_A = \psi_B \mathcal{E}$ and $q^{\dagger}\psi_B = \psi_A \mathcal{E}$. Since the eigen energies of $\Gamma\psi_i$ is $-\epsilon_i$, $\psi_j^{\dagger}\Gamma\psi_i = 0$, $(i, j = 1, \cdots, N)$. Thus, we can get

$$\Psi^{\dagger}\Gamma\Psi = \begin{pmatrix} \psi_1^{\dagger} \\ \psi_2^{\dagger} \\ \vdots \\ \psi_N^{\dagger} \end{pmatrix} (\Gamma\psi_1, \Gamma\psi_2, \cdots, \Gamma\psi_N) = \begin{pmatrix} \psi_1^{\dagger}\Gamma\psi_1 & \psi_1^{\dagger}\Gamma\psi_2 & \cdots & \psi_1^{\dagger}\Gamma\psi_N \\ \psi_2^{\dagger}\Gamma\psi_1 & \psi_2^{\dagger}\Gamma\psi_2 & \cdots & \psi_2^{\dagger}\Gamma\psi_N \\ \vdots & \vdots & \ddots & \vdots \\ \psi_N^{\dagger}\Gamma\psi_1 & \psi_N^{\dagger}\Gamma\psi_2 & \cdots & \psi_N^{\dagger}\Gamma\psi_N \end{pmatrix} = O \tag{2.44}$$

For the expressions of ψ_A and ψ_B, we can get

$$\Psi^{\dagger}\Gamma\Psi = \frac{1}{2}(\psi_A^{\dagger}, \psi_B^{\dagger}) \begin{pmatrix} I & O \\ O & -I \end{pmatrix} \begin{pmatrix} \psi_A \\ \psi_B \end{pmatrix} = \frac{1}{2}(\psi_A^{\dagger}\psi_A - \psi_B^{\dagger}\psi_B) = O \tag{2.45}$$

$$\Rightarrow \psi_A^{\dagger}\psi_A = \psi_B^{\dagger}\psi_B \tag{2.46}$$

Because of $\Psi^{\dagger}\Psi = I$, then we obtain $\frac{1}{2}(\psi_A^{\dagger}, \psi_B^{\dagger}) \begin{pmatrix} \psi_A \\ \psi_B \end{pmatrix} = \frac{1}{2}(\psi_A^{\dagger}\psi_A + \psi_B^{\dagger}\psi_B) = I \Rightarrow \psi_A^{\dagger}\psi_A = I$, $\psi_B^{\dagger}\psi_B = I$. To calculate the Berry phase, we use the gauge fixing with

an arbitrary multiplet Φ, and assume Φ as $\Phi = \begin{pmatrix} I \\ O \end{pmatrix}$. The gauge fixing is making a new state Ψ_Φ calculated from a gauge invariant projection operator $P = \Psi^\dagger \Psi$ and Φ and Ψ_Φ is calculated from $\Phi_\Psi = \frac{1}{C} P\Phi/$ where C is a normalized coefficient. Then, we can get,

$$\Psi_\Phi = \frac{1}{C} P\Phi = \frac{1}{C} \Psi^\dagger \Psi \Phi = \frac{1}{C} \begin{pmatrix} \psi_A \\ \psi_B \end{pmatrix} (\psi_A^\dagger, \psi_B^\dagger) \begin{pmatrix} I \\ O \end{pmatrix} = \frac{1}{2C} \begin{pmatrix} I \\ \psi_B \psi_A^\dagger. \end{pmatrix} \quad (2.47)$$

Since $q^\dagger \psi_A = \psi_B \mathcal{E}$, then we can get $\psi_B \psi_A^\dagger = \psi_B \mathcal{E} \mathcal{E}^{-1} \psi_A^\dagger = q^\dagger \psi_A \mathcal{E}^{-1} \psi_A^\dagger$. Moreover a normalized constant C^2 is given by $C^2 = |(\Phi^\dagger P) P\Phi|$, then we obtain,

$$C^2 = \frac{1}{2} \left| (I, O) \begin{pmatrix} \psi_A \\ \psi_B \end{pmatrix} (\psi_A^\dagger, \psi_B^\dagger) \begin{pmatrix} I \\ O \end{pmatrix} \right| = \frac{1}{2} |I| = \frac{1}{2}. \quad (2.48)$$

Therefore, we can get

$$\Psi_\Phi = \frac{1}{2C} \begin{pmatrix} I \\ \psi_B \psi_A^\dagger \end{pmatrix} = \frac{1}{\sqrt{2}} \begin{pmatrix} I \\ q^\dagger \psi_A \mathcal{E}^{-1} \psi_A^\dagger \end{pmatrix} \equiv \frac{1}{\sqrt{2}} \begin{pmatrix} I \\ q^\dagger g \end{pmatrix}, \quad (2.49)$$

where $g = \psi_A \mathcal{E}^{-1} \psi_A^\dagger$. Using Ψ_Φ, we can calculate the Berry phase. Firstly, the Berry connection A is given as $A = \Psi_\Phi^\dagger d\Psi_\Phi = \frac{1}{2}(I, \xi^\dagger) \begin{pmatrix} O \\ d\xi \end{pmatrix} = \frac{1}{2}\xi^\dagger d\xi$, where ξ is defined as $\xi \equiv q^\dagger g$. Moreover we can get, $\xi\xi^\dagger = q^\dagger g g^\dagger q = q^\dagger g g q = q^\dagger \psi_A \mathcal{E}^{-1} \psi_A^\dagger \psi_A \mathcal{E}^{-1} \psi_A^\dagger q = q^\dagger \psi_A \mathcal{E}^{-1} \mathcal{E}^{-1} \psi_A^\dagger q = (\psi_B \mathcal{E}) \mathcal{E}^{-1} \mathcal{E}^{-1} (\mathcal{E} \psi_B^\dagger) = \psi_B \psi_B^\dagger = I$, where we use the relations $g^\dagger = (\psi_A \mathcal{E}^{-1} \psi_A^\dagger)^\dagger = \psi_A \mathcal{E}^{-1} \psi_A^\dagger = g$, and $q^\dagger \psi_A = \psi_B$. Therefore, we obtain $\mathcal{E}^\dagger = \mathcal{E}^{-1}$ and A is $A = \frac{1}{2}\xi^{-1} d\xi$. Since ξ is a unitary matrix and can be diagonalized. Generally, a diagonalizable matrix satisfies $\text{Tr}\xi d\xi = \text{Tr}d\log\xi = d\log\det\xi$. Thus the Berry phase calculated as

$$\gamma = -i \int \text{Tr} A = -\frac{i}{2} \int d\log\det\xi = -\frac{i}{2} \int d\log\det q^\dagger g$$

$$= -\frac{i}{2} \int d\{\text{Re}(\log\det q^\dagger g) + i\text{Im}(\log\det q^\dagger g)\}. \quad (2.50)$$

In addition, the Berry phase is quantized and real number when a multiplet Ψ is gapped. Then $\text{Re}(\log\det q^\dagger g)$ in Eq.2.50, has to be 0. Moreover $\det g = \det(\psi_A[E^{-1}\psi_A^\dagger) = \det\psi_A \det\mathcal{E}^{-1} \det\psi_A^\dagger = (\det\mathcal{E})^{-1} \in \mathbb{R}$, then we obtain

$$\gamma = \frac{1}{2} \int d\text{Im}(\log\det q^\dagger + \log\det g) = -\frac{1}{2}\arg\det q \quad (2.51)$$

Chapter 3

Energy spectra of silicene and graphene ribbons

3.1 Comparison of silicene ribbons with graphene ribbons

We now show the numerical results of energy spectra of graphene and silicene ribbons without hydrogen terminations or terminated by single hydrogen atom at both edges. In Fig.3.1(a), we show an energy spectrum of a graphene ribbon without a hydrogen termination as function of a wave number k. There are two types of the in-gap states (i) and (ii) in this figure, and these in-gap states are doubly degenerated. Here we denote these degenerated states by $\sum_\alpha \sum_i \psi_\alpha^1(k, x_i)$ and $\sum_\alpha \sum_i \psi_\alpha^2(k, x_i)$, where α and x_i denote orbitals of an electron and x-coordinates of silicon atoms in the unit cell, respectively. Fig.3.2(a) and (b) show numerical values of coefficients of averaged in-gap states of graphene ribbons as a function of x-coordinates of carbon atoms in the unit cell, respectively. These averaged in-gap states (i) and (ii) are summed up in a ranges of $k = \pm\frac{\pi}{2}(1-n/L_2)$ for $L_2 = 400$ and $n = 0,\ 1, \cdots, 24, 25$ and a ranges of $k = \frac{\pi}{2}(n/L_2)$ for $n = -25, -24, \cdots, 24, 25$, respectively. In these figures, we assume a position of a carbon atom at the left edge as the origin of the graph [Fig.2.1(b)]. In Fig.3.1(a), the in-gap states (i) are identical to a result of a single orbital tight-binding model, which is only taken into account π-electrons [31], and as a corollary to this result, coefficients of a wave function of this in-gap state have only p_z components at edge sites [Fig.3.2(a)], which are vertical to the plane. On the other hand, in-gap states (ii) are revealed by taking into account a multi-orbital tight-binding model, and these components of wave function of in-gap states have only s, p_x and p_y components [Fig.3.2(b)]. In the case of an sp^2 hybridized orbital (graphene), these results of components of the wave function of in-gap states are trivial because of the orthogonality between the σ and π orbitals. In an experimental situation, a zigzag graphene ribbon is terminated by single hydrogen atom, since interactions of σ bonds are relatively larger than that of π bonds. Therefore an energy spectrum like Fig.3.1(b), is emerged.

Fig.3.1(c) and (d) show energy spectra of silicene ribbons without hydrogen termination and terminated by single hydrogen atom at both edges, respectively.

In these figures, there are six kinds of in-gap states (iii)-(viii), and they are doubly degenerated. In Fig.3.3(a), (b) and (c), we show coefficients of wave functions of in-gap states (iii), (iv) and (vii) for silicene ribbons. Similarly for the cases of graphene ribbons, we plot these figures as function of x-coordinates of the positions of silicon atoms, and averaged in-gap states (iii) and (vii) are summed up in a ranges of $k = \pm\frac{\pi}{2}(1-n/L_2)$ for $L_2 = 400$ and $n = 0, 1, \cdots, 24, 25$. On the other hand the averaged in-gap states is also summed up a ranges of $k = \frac{\pi}{2}(n/L_2)$ for $n = -25, -24, \cdots, 24, 25$, respectively. In Fig3.3(a), at sites of left and right edges, coefficients of s and p_x orbitals are relatively large than p_y and p_z ones. On the other hand at inner sites adjacent to the edge sites, coefficients of the p_y orbital are relatively large. Thus, components which are parallel to the plane near the edges, contribute mainly to these in-gap states. Furthermore, the in-gap states (iv) are emerged in a region which is different from that of in-gap states (iii) [Fig.3.1(c)]. The in-gap states (iv) consist mainly of p_x orbitals at the edge sites, and p_z orbitals at inner sites adjacent to the edge sites. Additionally, it is found that these in-gap states of a silicene ribbon are different from one of a graphene ribbon in the coefficients of wave functions. These results are caused by a buckled structure. Moreover for an energy spectra of a hydrogen terminated silicene ribbon [Fig.3.1(d)], we obtain in-gap states (vii) like the in-gap states (i) of a graphene ribbon [Fig.3.1(a)]. Besides in the wave function of the in-gap states (vii), the coefficients of the p_z orbitals at the edge sites are large like the case of the in-gap states (i) of the graphene ribbon [Fig.3.3(c)].

In higher energy regions above the Fermi energy, we also obtain in-gap states (v), (vi) and (viii) in energy spectra of 0H/0H and 1H/1H silicene ribbons[Fig.3.1(c) and (d)]. These in-gap states are doubly degenerate and its localization lengths are larger than that of near the Fermi level due to the band gap narrowing. Components of the wave functions of the in-gap state (v) as function of the x-coordinates of silicon sites, are shown in Fig.3.4(a). In this figure, p_x and p_z orbitals are dominant at silicon sites on the both edges. Additionally, s orbitals are dominant at inner sites adjacent to the edge sites. Similarly, Fig.3.4(b) shows components of the wave functions of the in-gap state (vi) as function of the x-coordinates of silicon sites. At the sites on the edges p_z orbitals are dominant, on the other hand at the silicon sites around $x = 4$ and $x = 114$ p_z and s orbitals contribute mainly. Furthermore, Figure.3.4(c) shows of components of edge states (viii). In this figure, p_z orbitals at the silicon sites on the edge mainly contribute.

3.2   Several edge terminations at left and right edges

In the previous subsection, we discuss a comparison between graphene and silicene ribbons without or with a hydrogen termination. Here, we discuss influences of several types of edge terminations at each left and right edges, and consider eight kinds of edge geometries, which are expressed as Figs.2.2(b), (d)-(f), and Fig.2.3. In Fig.3.5(a), we show an energy spectrum of a silicene ribbon whose left and right edges are terminated by two hydrogen atoms [Fig.2.2(f)]. In this figure, there are doubly degenerate in-gap states which like one of graphene ribbon with the Klein
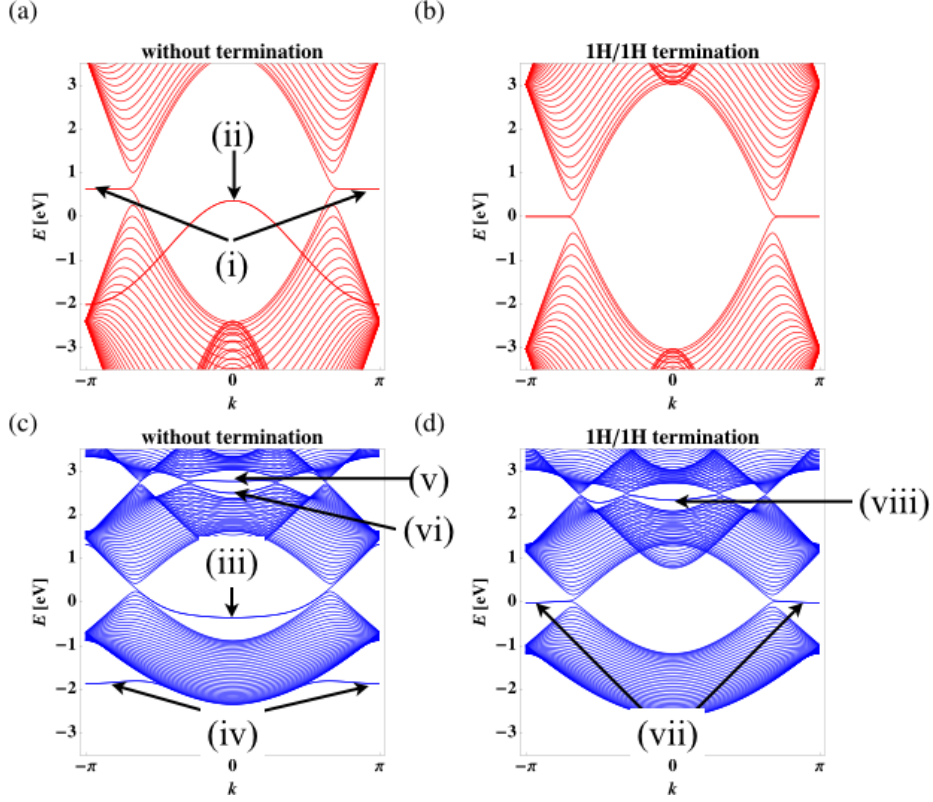
Fig. 3.1   Energy spectra of zigzag graphene and silicene ribbons as a function of a wave number k. (a), (b) : Energy spectra of graphene ribbons without or with a hydrogen termination at each edges. i and ii indicate two in-gap states. (c), (d) : Energy spectra of silicene ribbons without or with a hydrogen termination at each edges. As well as the case of graphene ribbons, (iii)$-$(viii) indicate two in-gap states.

edges [32, 33], and we name these states in-gap states (ix). Moreover in Fig.3.6(a), we show coefficients of wave function of an averaged in-gap states (ix). As well as previous subsection, these averaged in-gap states (ix) are summed up in the ranges of $k = \frac{\pi}{2}(n/L_2)$ for $L_2 = 400$ and $n = -25, -24, \cdots, 24, 25$. From the result of Fig.3.6(a), these wave functions are constructed mainly by p_z orbitals at inner sites adjacent to edge sites in Fig.2.1(b). Therefore, it can be interpreted that the Klein edge of a graphene ribbon, is effectively realized due to a termination by two hydrogen atoms.

In Fig.3.5(b), we show an energy spectrum of a silicene ribbon whose left edge is terminated by two hydrogen atoms and right edge is terminated by a hydrogen atom [Fig.2.2(e)]. In this figure, there are non-degenerate in-gap states, and we call these states in-gap states (x) $< (|\phi_1(k)|^2 + |\phi_2(k)|^2)/2 >$. Moreover in Fig.3.6(b), we show coefficients of wave function of an averaged in-gap states (v) which resemble a flat-band in a graphene ribbon whose left edge is the zigzag edge and right edge is the Klein edge, and these averaged in-gap states (x) are summed up in the ranges of $k = \frac{\pi}{2}(n/L_2)$ for $L_2 = 400$ and $n = -400, -399, \cdots, 399, 400$.
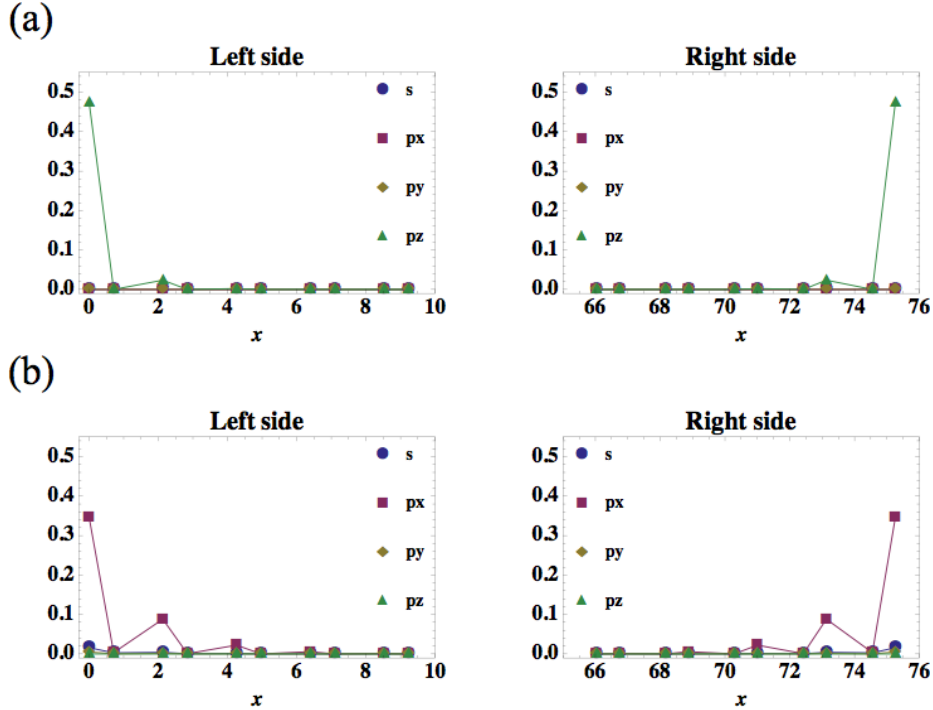
Fig. 3.2   Coefficients of edge states of a graphene ribbon without hydrogen termination. x-axis corresponds to the x-coordinates of silicon sites. (a): For the case of in-gap state (i) in Fig.3.1(a). (b): For the case of in-gap state (ii) in Fig.3.1(a).

From the result of Fig.3.6(b), these wave functions are constructed mainly by p_z orbitals at inner site adjacent to the left edge site and the right edge site in Fig.2.1(b). Therefore, it can be interpreted that the Klein and the graphene edges are effectively realized due to hydrogen terminations. Additionally, we consider silicene ribbons whose left edges are terminated by one or two hydrogen atoms and a right edge is no termination. Fig.3.5(c) shows an energy spectrum of a silicene ribbon whose left edges are terminated by a hydrogen atom and a right edge has no termination[Fig.2.2(b)]. In this figure, we obtain an energy spectrum like an intermediate spectrum between Fig.3.1(c) and (d). On the other hand, Fig.3.5(d) shows an energy spectrum of a silicene ribbon whose left edges are terminated by two hydrogen atoms and a right edge has no termination[Fig.2.2(d)]. In this figure, we obtain an energy spectrum like an intermediate spectrum between Fig.3.1(c) and Fig.3.5(a). These intermediate energy spectra result from assuming width of ribbons enough to consider that interactions between both edges are negligible.

  Next we show the energy spectra of 1H'/0H, 1H'/1H, 1H'/1H' and 2H/1H' silicene ribbons[Fig.2.3]. Figure.3.7(c) shows an energy spectrum of 1H'/1H' silicene ribbons and we obtain three kinds of in-gap states (xi), (xii) and (xiii). Similar to the above, the localization lengths of wave functions of these in-gap states in the higher energy region are larger than that of the wave functions near the Fermi level[Fig.3.8]. Fig.3.8(a) shows components of the wave function of in-gap states
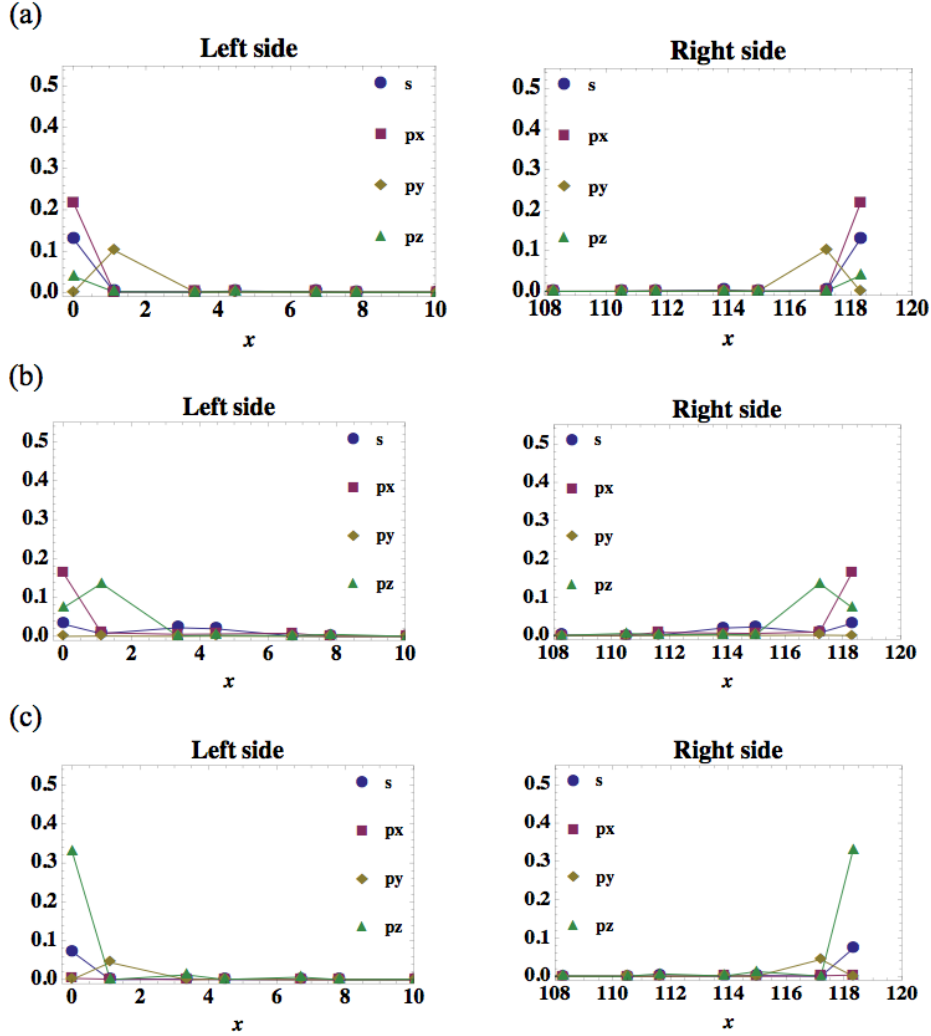
Fig. 3.3 Coefficients of edge states of silicene ribbons with or without hydrogen termination. (a): For the case of in-gap state (iii) in Fig.3.1(c). (b): For the case of in-gap state (iv) in Fig.3.1(c). (c): For the case of in-gap state (vii) in Fig.3.1(d).

(xi) as function of x-coordinates of silicon atoms. As shown in this figure, four orbitals at edge sites almost equivalently contribute to these in-gap states. Additionally, s and p_x orbitals at inner sites from edge sites also contribute to these edge states. Besides, Fig.3.8(b) shows components of the wave function of in-gap states (xii) in the same manner as Fig.3.8(a). Although, as shown in Fig.3.7(c) and 3.5(a), these in-gap states are similar to the edge states (ix) for the 2H/2H silicene ribbon, s orbitals at neighbor sites from edge sites mainly contribute to these in-gap states. Moreover, we show components of the wave function of in-gap states (xiii) in Fig.3.8. As shown in this figure, s orbitals at inner sites around $x = 3.5$ and $x = 74.75$ contribute mainly and contributions of p_x orbitals around $x = 0 \sim 6.75$ and $x = 71.5 \sim 78$ can not be negligible. As shown in Figs.3.7(a), (b), and (d), we obtain intermediate energy spectra between the 1H'/1H' silicene
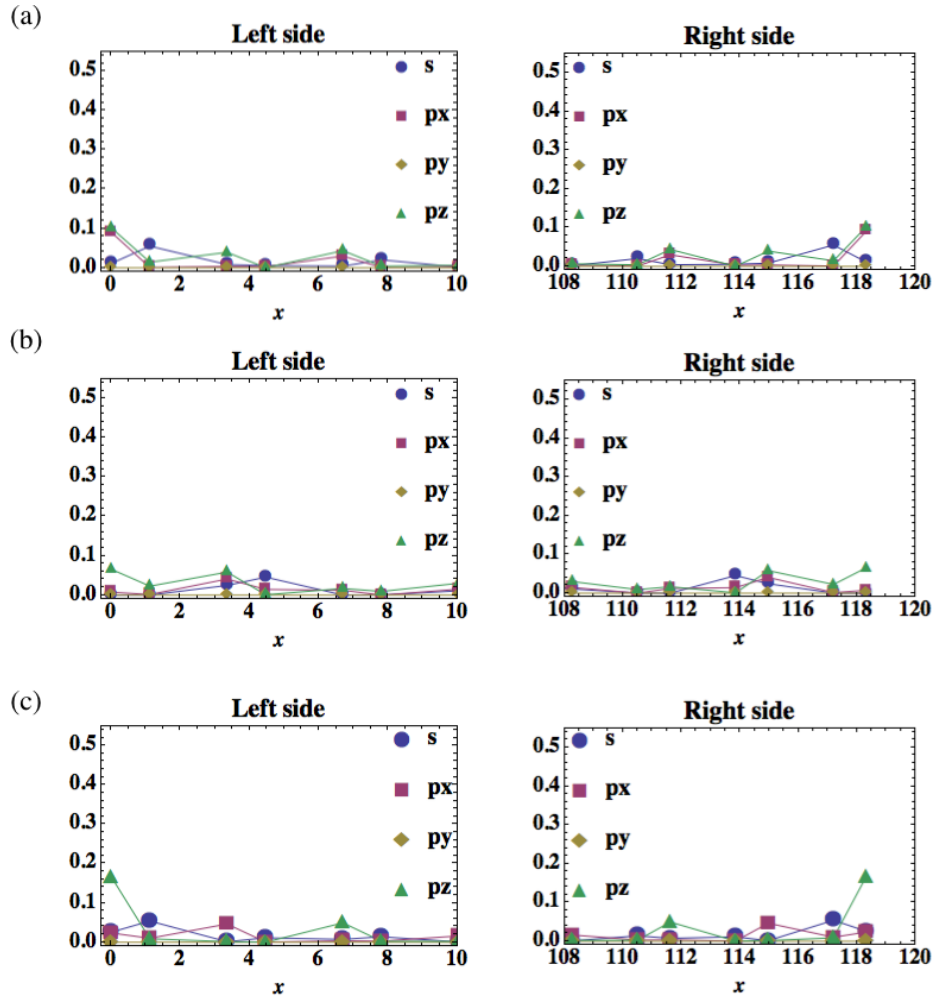
Fig. 3.4   Coefficients of edge states of silicene ribbons with or without hydrogen termination in the higher energy region. (a): For the case of in-gap state (v) in Fig.3.1(c). (b): For the case of in-gap state (vi) in Fig.3.1(c). (c): For the case of in-gap state (viii) in Fig.3.1(d).

ribbon and other hydrogen terminated silicene ribbons. Thus, we find that in-gap states can be partially controlled by hydrogen terminations.
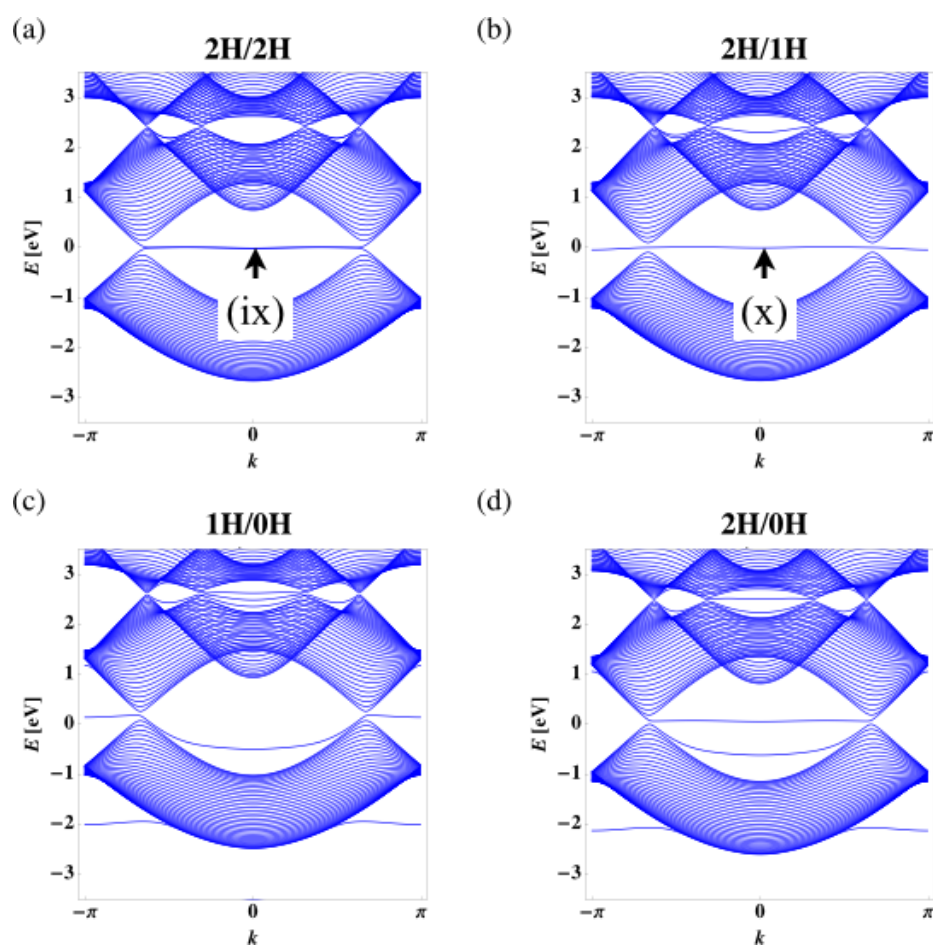
Fig. 3.5   Energy spectra of silicene ribbons as a function of a wave number k with 2H/2H(a), 2H/1H(b), 1H/0H(c) 2H/0H(d) edge terminations. (ix) and (x) indicate two in-gap states.
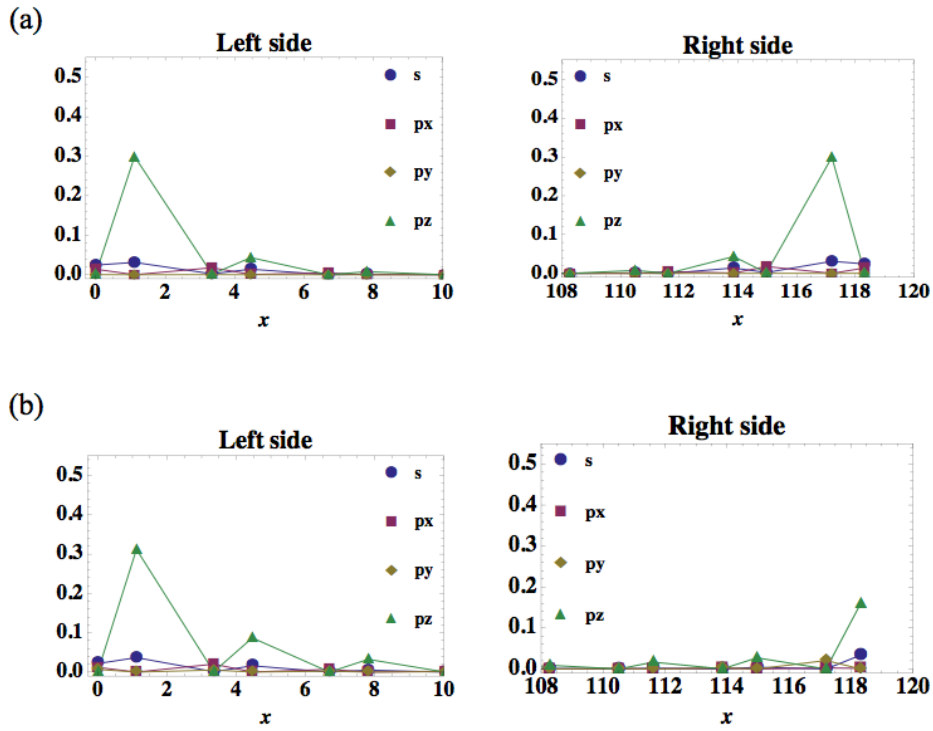
Fig. 3.6   Coefficients of edge states of silicene ribbons with several types of hydrogen termination. (a): For the case of in-gap state (ix) in Fig.3.5(a). (b): For the case of in-gap state (x) in Fig.3.5(b).

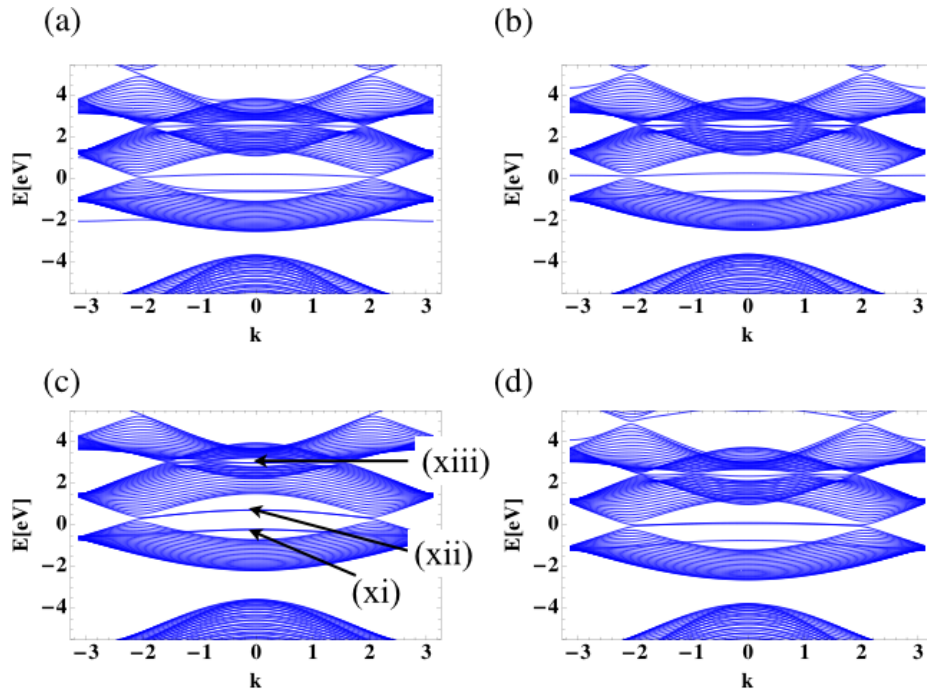Fig. 3.7   Energy spectra of silicene ribbons as a function of a wave number k with 1H'/0H(a), 1H'/1H(b), 1H'/1H'(c) 2H/1H'(d) edge terminations.
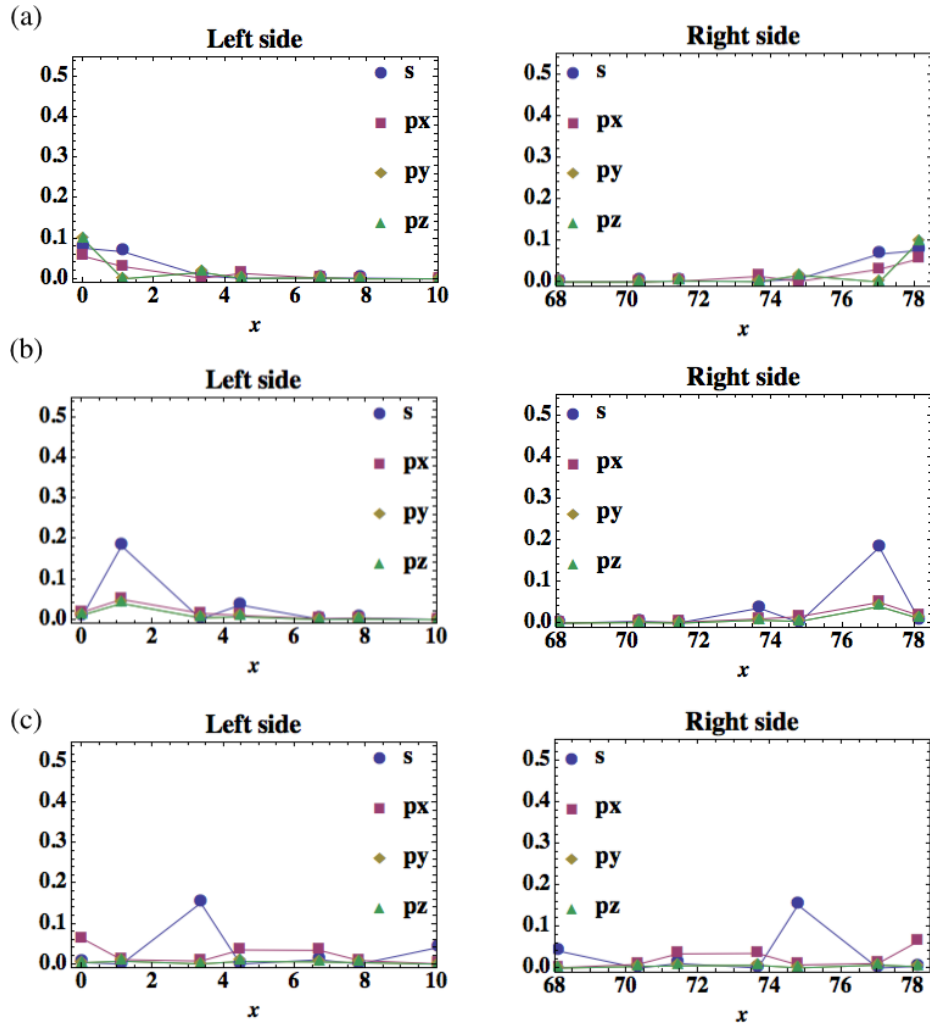
Fig. 3.8   Coefficients of edge states of silicene ribbons with or without hydro-
gen termination. (a): For the case of in-gap state (xi) in Fig.3.7(c). (b): For
the case of in-gap state (xii) in Fig.3.7(c). (c): For the case of in-gap state
(xiii) in Fig.3.7(c).

Chapter 4

Physical origin of edge states

4.1 Physical origin of edge states in hydrogen terminated zigzag silicene ribbons

In this section, we discuss the physical origin of edge states which are obtained in the previous sections. To do this, we consider a continuous deformation of on-site energies ϵ_s, ϵ_p and ϵ_H in the model, from realistic parameters which are $\epsilon_s = -14.69$eV, $\epsilon_p = -8.08$eV and $\epsilon_H = -13.55$eV to a chiral symmetric parameters which are $\epsilon_s = \epsilon_p = \epsilon_H = -14.69$eV. Firstly, we explain the reason why the model is chiral symmetric for parameters which are $\epsilon_s = \epsilon_p = \epsilon_H = -14.69$eV. After that, we show numerical results of energy spectra of silicene ribbons with several types of hydrogen terminations.

4.1.1 Transformation of a hamiltonian of on-site energies from realistic to chiral symmetric models

To discuss the continuous deformation of the models, we consider a change of bases of hamiltonian from $\{s, p_x, p_y, p_z\}$ to $\{|1\rangle, |2\rangle, |3\rangle, |4\rangle\}$, where $|1\rangle$ is a hybrid orbital direct to the direction which is perpendicular to the plane of silicene, $|2\rangle$, $|3\rangle$, and $|4\rangle$ are also the hybrid orbitals direct to the directions which are parallel to the Si-Si bonds of silicene[Fig.4.1]. Here, we assume states of these orbitals for B sublattice. Hybrid orbitals $|i\rangle$ ($i = 1, 2, 3, 4$) can be expressed as $|i\rangle = c_i^s |s\rangle + c_i^x |p_x\rangle + c_i^y |p_y\rangle + c_i^z |p_z\rangle$ using wavefunctions of s, p_x, p_y, and p_z orbitals. Using these expressions, a hamiltonian $\mathcal{H}_{on-site}$ ($\mathcal{H}_{on-site} = \mathrm{diag}(\epsilon_s, \epsilon_p, \epsilon_p, \epsilon_p)$) of a single atom can be transformed as follows;

$$
\mathcal{H}_{on-site} = \begin{pmatrix}
\epsilon_s + (\epsilon_s - \epsilon_p)|c_1^s|^2 & (\epsilon_s - \epsilon_p)c_1^s c_2^{s*} & (\epsilon_s - \epsilon_p)c_1^s c_3^{s*} & (\epsilon_s - \epsilon_p)c_1^s c_4^{s*} \\
(\epsilon_s - \epsilon_p)c_2^s c_1^{s*} & \epsilon_s + (\epsilon_s - \epsilon_p)|c_2^s|^2 & (\epsilon_s - \epsilon_p)c_2^s c_3^{s*} & (\epsilon_s - \epsilon_p)c_2^s c_4^{s*} \\
(\epsilon_s - \epsilon_p)c_3^s c_1^{s*} & (\epsilon_s - \epsilon_p)c_3^s c_2^{s*} & \epsilon_s + (\epsilon_s - \epsilon_p)|c_3^s|^2 & (\epsilon_s - \epsilon_p)c_3^s c_4^{s*} \\
(\epsilon_s - \epsilon_p)c_4^s c_1^{s*} & (\epsilon_s - \epsilon_p)c_4^s c_2^{s*} & (\epsilon_s - \epsilon_p)c_4^s c_3^{s*} & \epsilon_s + (\epsilon_s - \epsilon_p)|c_4^s|^2
\end{pmatrix}.
$$
$$(4.1)$$

For $\epsilon_s \neq \epsilon_p$, this hamiltonian is not diagonal matrix and does not possess chiral symmetry. However, if $\epsilon_s = \epsilon_p$, this hamiltonian possess chiral symmetry then
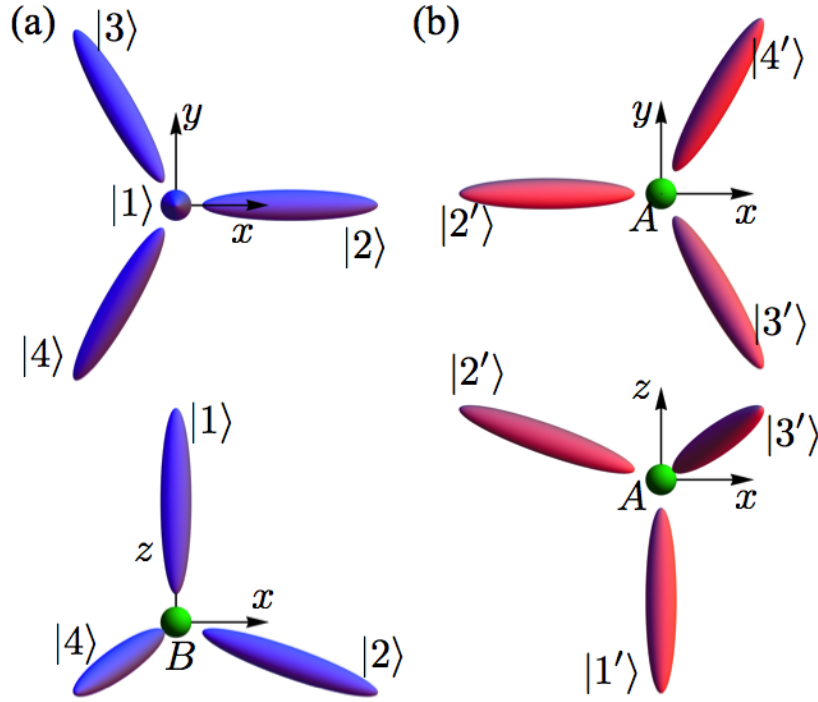
Fig. 4.1 Schematic description of hybrid orbitals of A(Figure.(a)) and B(Figure.(b)) sublattices. Red and blue ellipsoids mean hybrid orbitals. Upper(bottom) figure shows top(side) view of four orbitals.

discussions of flat bands due to the chiral symmetry are available similar to the case of graphene. This consideration is also applied to cases of hydrogen terminated silicene ribbons.

4.1.2   Continuous deformation of on-site energies from realistic to chiral symmetric models

Here, we show numerical results of energy spectra of several systems for applying continuous deformation of on-site energies to the models from realistic to chiral symmetric models. To consider continuous deformations of on-site energies for hydrogen terminated silicene ribbons, we introduce a parameter $\alpha(0 \leq \alpha \leq 1)$ which changes on-site energies ϵ_p and ϵ_H as follows $\epsilon_p' = \alpha\epsilon_p + (1-\alpha)\epsilon_s$ and $\epsilon_H' = \alpha\epsilon_H + (1-\alpha)\epsilon_s$. When $\alpha = 1$, these on-site energies correspond to realistic ones. On the other hand when $\alpha = 0$, this model corresponds to a chiral symmetric model.

Bulk silicene
Firstly, we consider numerical results of energy spectra of bulk silicene deforming on-site energies. Fig.4.2 shows energy spectra for several cases of an on-site energy difference between s and p orbitals. In this figure, for the case whose an on-site energy differences is $\epsilon_s - \epsilon_p = -6.61$eV which correspond to realistic silicene, the

(a)

(b)
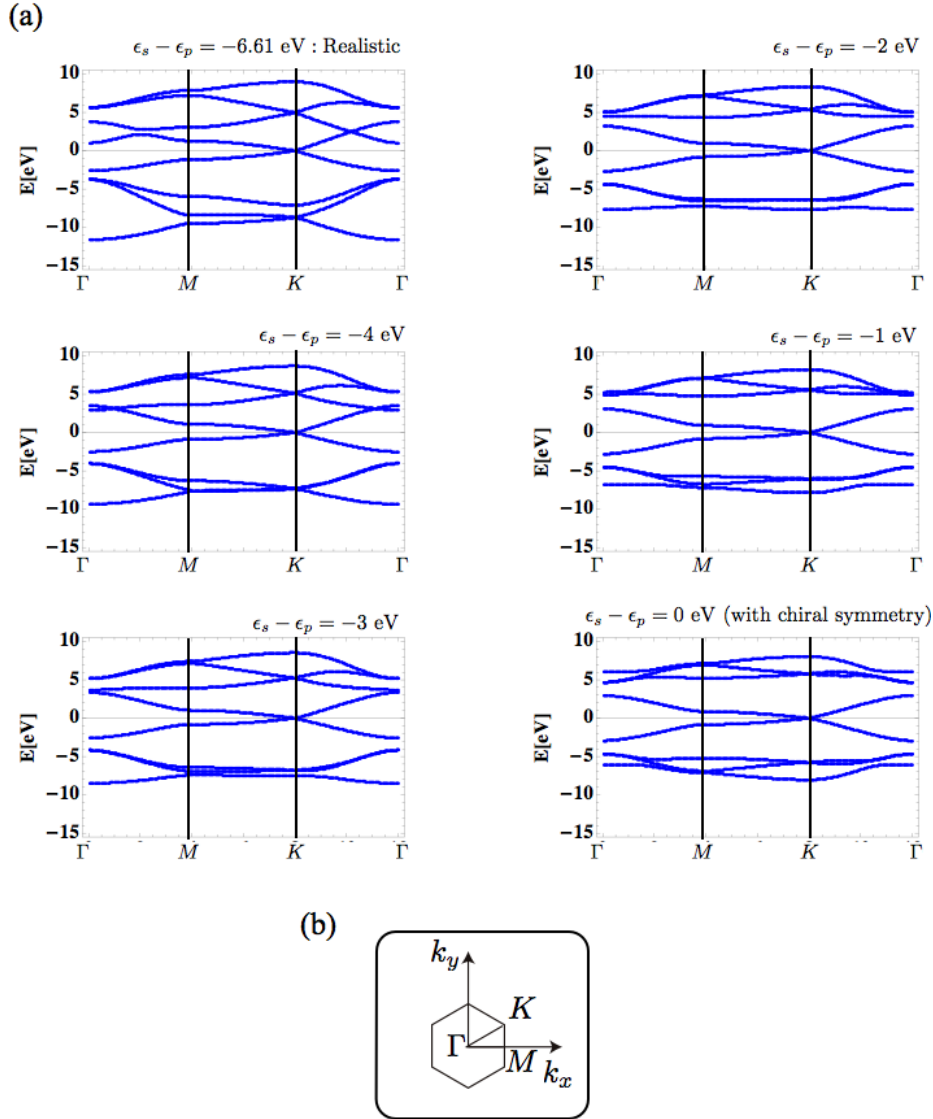
Fig. 4.2   Energy spectra of bulk silicene with several variations of on-site energies.

behaviors of energy bands are consistent with energy bands calculated by DFT calculations [1, 23, 2] in points of view of a linear dispersion near the Fermi level and a shape of energy bands in a region of low-energy. As deforming energy differences between on-site energies, energy bands in low energy region below the Fermi level change significantly and shift to higher energy regions. On the other hand, in the higher energy region above the Fermi level, the width of these energy bands narrow as deforming the energy differences. For $\alpha = 0$ that the model has the chiral symmetry, the shape of energy bands are symmetric up and down with respect to the Fermi level ($E = 0$).
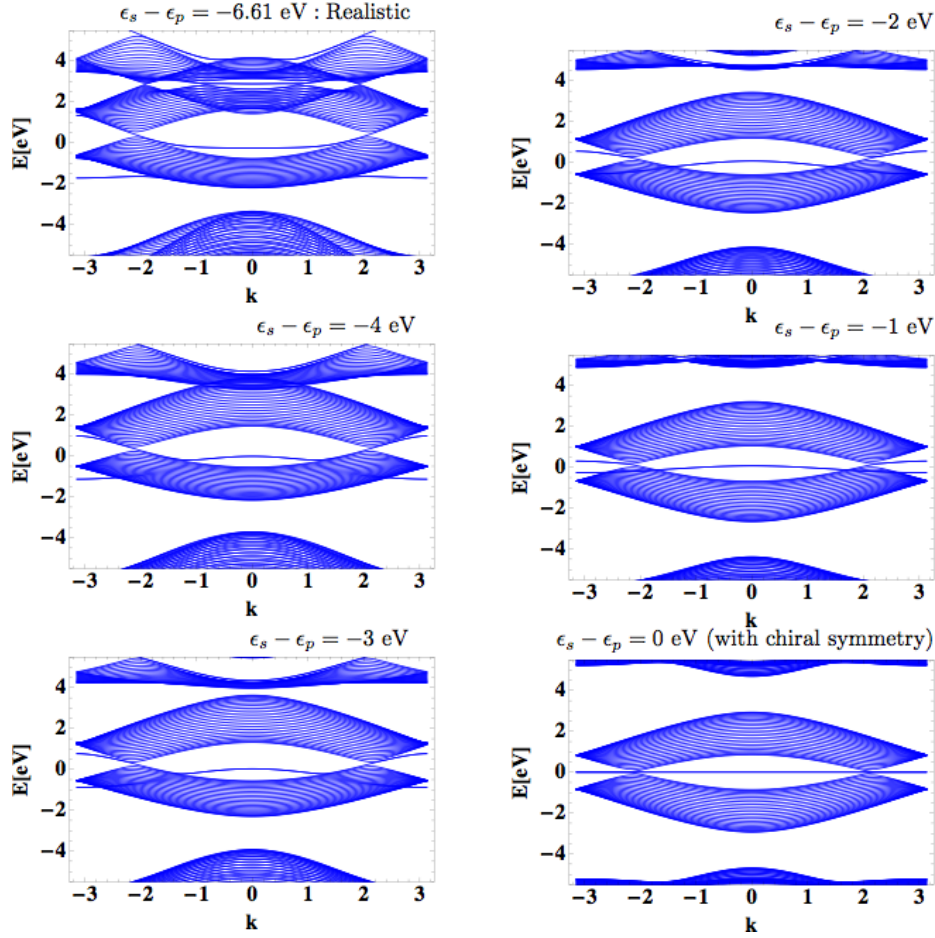
Fig. 4.3   Energy spectra of a 0H/0H zigzag silicene ribbon with several variations of on-site energies.

0H/0H silicene ribbon

Next, we show energy spectra of a 0H/0H zigzag silicene ribbons with several on-site energies[Fig.4.3]. For $\alpha = 1$, as mentioned Sec.3.1, we obtain two types of edge states near the Fermi level. As deforming energy differences, edge states in the region of a wave number space $-2\pi/3 \le k \le 2\pi/3$ come close to the Fermi level. On the other hand, edge states in the regions of a wave number space $-\pi \le k \le -2\pi/3$ and $2\pi/3 \le k \le \pi$ around $E \sim -2\text{eV}$ also come close to the Fermi level. Furthermore, other edge states, which are indistinguishable from energy bands of bulk around $E \sim 2\text{eV}$ for $\alpha = 1$ in the regions of a wave number space $-\pi \le k \le -2\pi/3$ and $2\pi/3 \le k \le \pi$, come down to the Fermi level and doubly degenerate. Eventually for $\alpha = 0$, these edge states degenerate at the Fermi level. In the regions of a wave number space $-\pi \le k \le -2\pi/3$ and $2\pi/3 \le k \le \pi$, edge states fourfold degenerate. Besides, in the region of a wave number space $-2\pi/3 \le k \le 2\pi/3$, edge states doubly degenerate.

Fig. 4.4 Energy spectra of 1H/1H silicene ribbon with several variations of on-site energies.

1H/1H silicene ribbon

Fig.4.4 shows energy spectra of a 1H/1H zigzag silicene ribbon. As deforming energy differences, edge states in the regions of a wave number space $-\pi \leq k \leq -2\pi/3$ and $2\pi/3 \leq k \leq \pi$, which similar to that of zigzag graphene ribbon are stable. This results indicated that edge states for the realistic 1H/1H silicene ribbon are adiabatically connected to the edge states for the chiral symmetric 1H/1H ribbon. On the other hand, in-gap states that emerge around $E \sim 4$eV in the regions of a wave number space $-\pi \leq k \leq -2\pi/3$ and $2\pi/3 \leq k \leq \pi$ for $\alpha = 1$, become indistinguishable from energy bands of bulk as deforming energy differences.
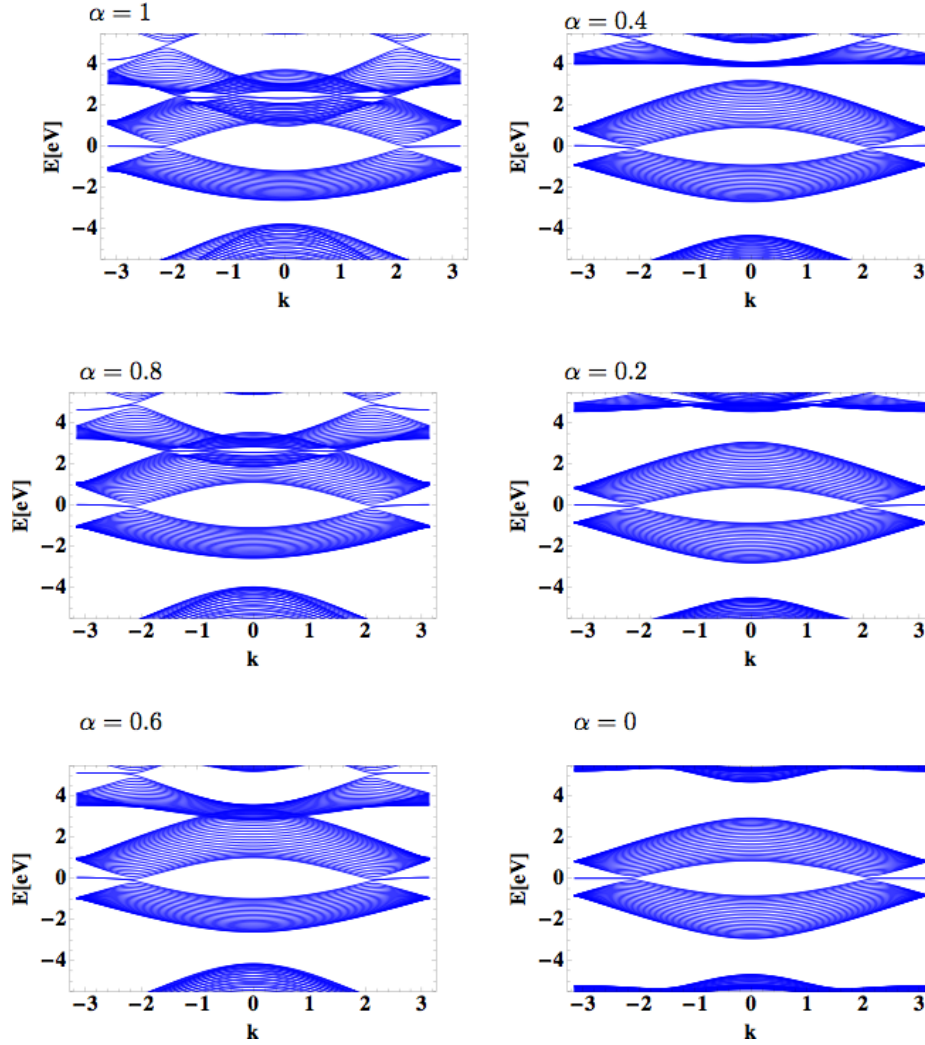
Fig. 4.5   Energy spectra of 2H/2H silicene ribbon with several variations of on-site energies.

2H/2H silicene ribbon

Fig.4.5 shows energy spectra of a 2H/2H zigzag silicene ribbon. Similar to the case of 1H/1H silicene ribbon, edge states in the region of a wave number space $-2\pi/3 \leq k \leq 2\pi/3$ are stable against deforming differences between on-site energies. Thus, these edge states are also adiabatically connected to the edge states of the chiral symmetric model. Moreover, for $\alpha = 0$, these energies of edge states are zero rigorously.

1H/0H silicene ribbon

Fig.4.6 shows energy spectra of a 1H/0H zigzag silicene ribbon. As deforming difference between on-site energies from $\alpha = 1$ to $\alpha = 0$, flat bands at the Fermi level are stable. In addition, energy bands of edge states around $E \sim -2\mathrm{eV}$ and
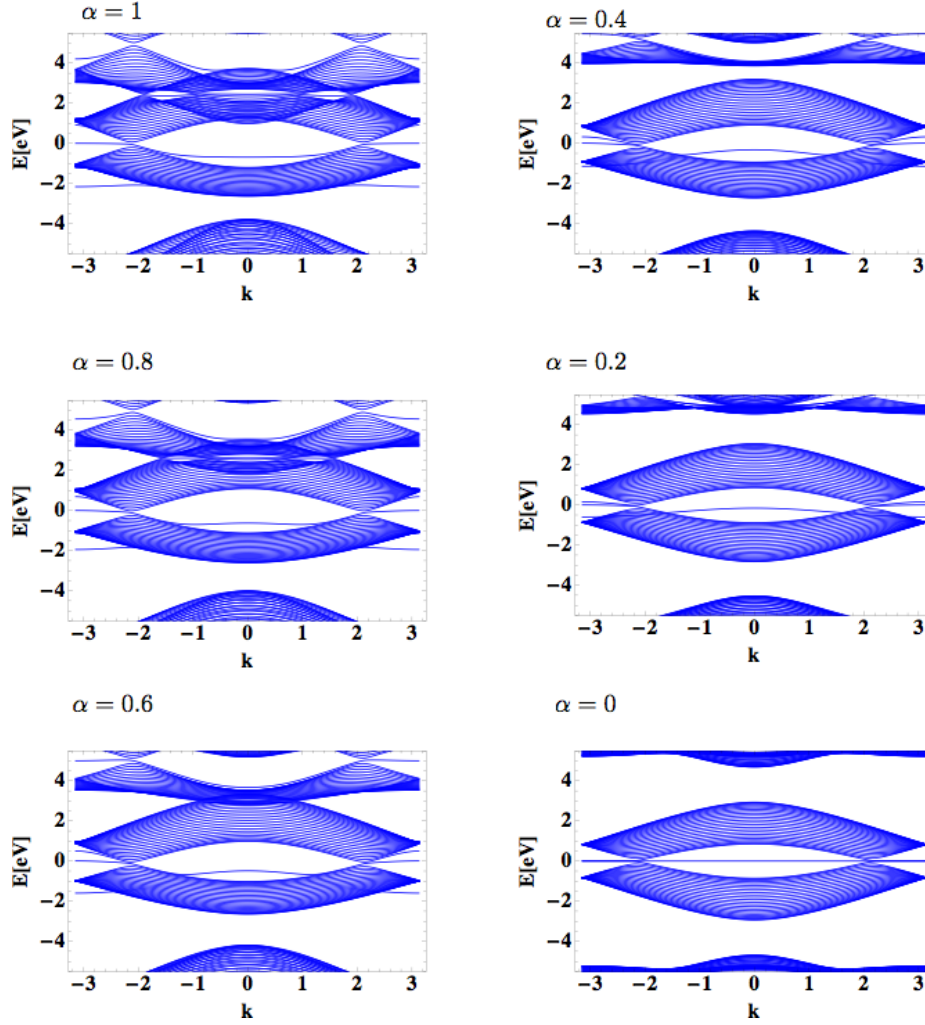
Fig. 4.6   Energy spectra of 1H/0H silicene ribbon with several variations of on-site energies.

$E \sim 2\text{eV}$ in the regions of k-space $-\pi \leq k \leq -2\pi/3$ and $2\pi/3 \leq k \leq \pi$, come close to the Fermi level. Simultaneously, energy bands of edge states in the regions of k-space $-2\pi/3 \leq k \leq 2\pi/3$ also come close to the Fermi level. For $\alpha = 0$, these edge states threefold degenerate in the regions of $-\pi \leq k \leq -2\pi/3$ and $2\pi/3 \leq k \leq \pi$, and non-degenerate in the regions of $-2\pi/3 \leq k \leq 2\pi/3$.

2H/1H silicene ribbon

Fig.4.7 shows energy spectra of a 2H/1H zigzag silicene ribbon. An energy band at the Fermi level is stable against the continuous deformation of α and non-degenerate. For $\alpha \neq 0$, this energy band is slightly dispersive, by contrast for $\alpha = 0$ an energy of this band is rigorously at the Fermi level ($E = 0$). In the after section, we show that this edge states originates from the chiral symmerty.
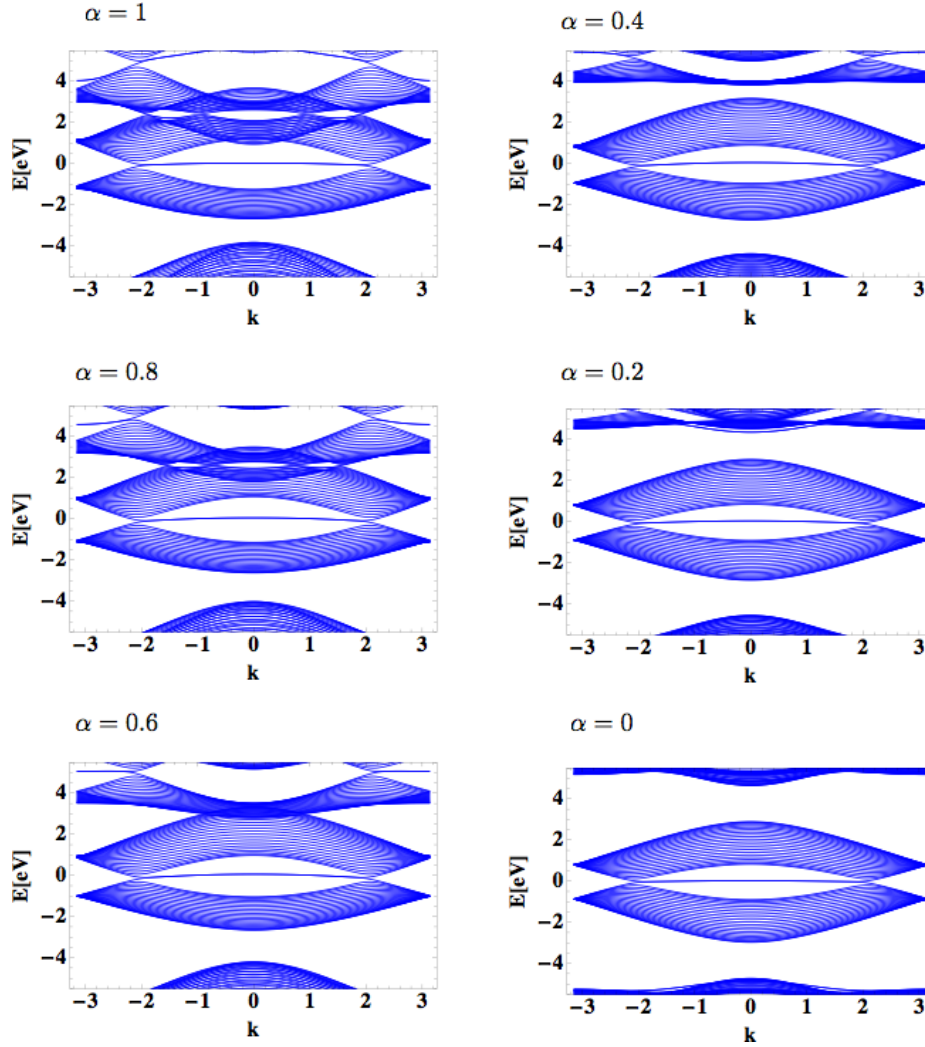
Fig. 4.7   Energy spectra of 2H/1H silicene ribbon with several variations of on-site energies.

2H/0H silicene ribbon

Fig.4.8 shows energy spectra of a 2H/0H zigzag silicene ribbon. As deforming difference between on-site energies from $\alpha = 1$ to $\alpha = 0$, flat bands in the region of of k-space $-2\pi/3 \leq k \leq 2\pi/3$ at the Fermi level are stable. In addition, energy bands of edge states around $E \sim -2$eV and $E \sim 2$eV in the regions of k-space $-\pi \leq k \leq -2\pi/3$ and $2\pi/3 \leq k \leq \pi$, come close to the Fermi level. Simultaneously, energy bands of edge states in the region of k-space $-2\pi/3 \leq k \leq 2\pi/3$ also come close to the Fermi level. For $\alpha = 0$, these edge states twofold degenerate in the whole region of k-space,
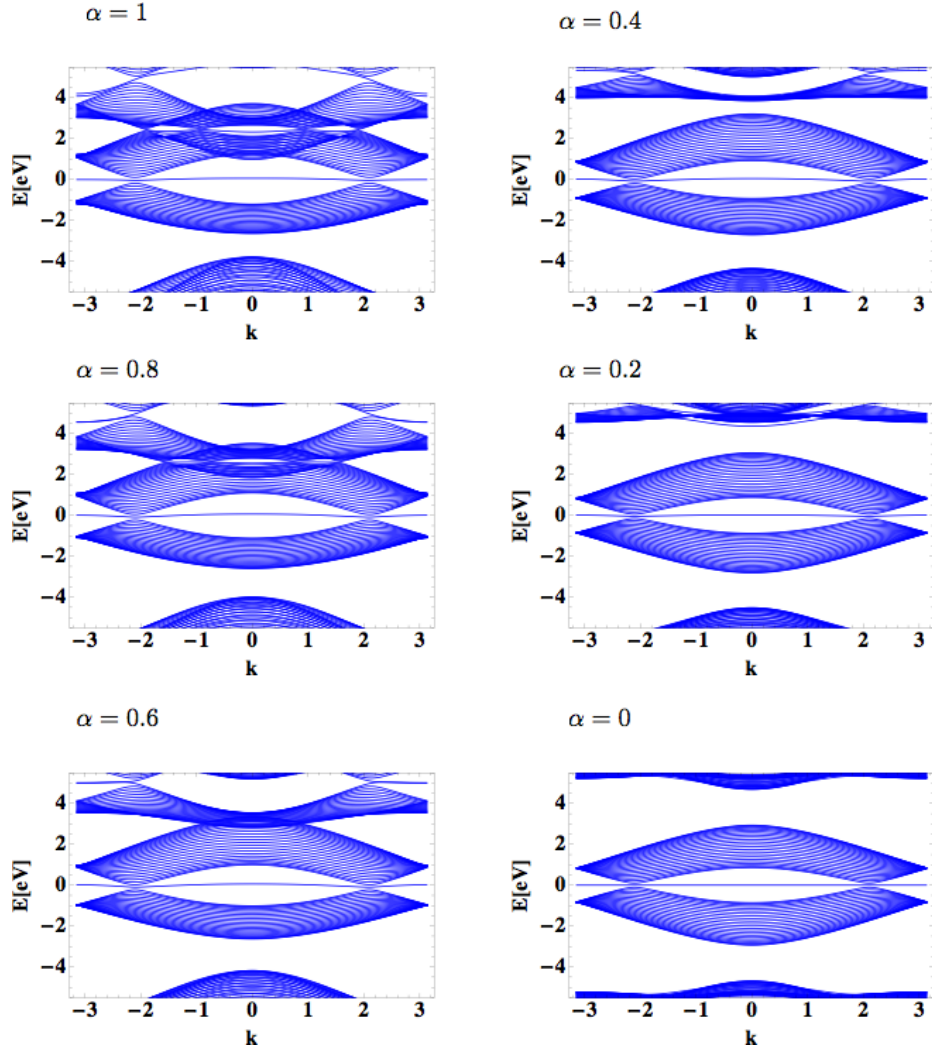
Fig. 4.8   Energy spectra of 2H/0H silicene ribbon with several variations of on-site energies.

1H'/0H silicene ribbon

Fig.4.9 shows energy spectra of a 1H'/0H zigzag silicene ribbon. As deforming difference between on-site energies from $\alpha = 1$ to $\alpha = 0$, flat bands in the region of of k-space $-2\pi/3 \leq k \leq 2\pi/3$ at the Fermi level is shifted to the high energy region. In addition, energy bands of edge states around $E \sim -2$eV and $E \sim 2$eV in the regions of k-space $-\pi \leq k \leq -2\pi/3$ and $2\pi/3 \leq k \leq \pi$, comes close to the Fermi level. Simultaneously, energy bands of edge states in the region of k-space $-2\pi/3 \leq k \leq 2\pi/3$ also come close to the Fermi level. For $\alpha = 0$, the edge state in the region of k-space $-2\pi/3 \leq k \leq 2\pi/3$ non-degenerate, by contrast the edge states in the regions of $-\pi \leq k \leq -2\pi/3$ and $2\pi/3 \leq k \leq \pi$ threefold degenerate.
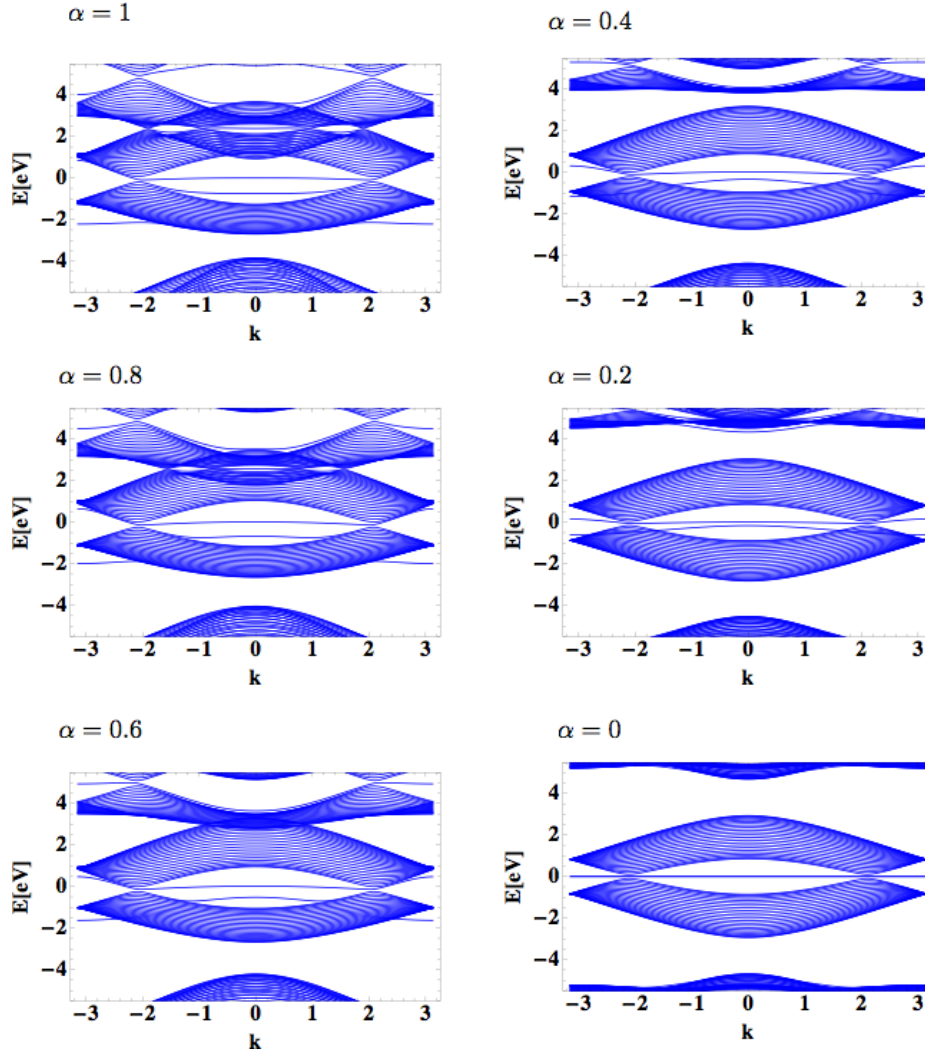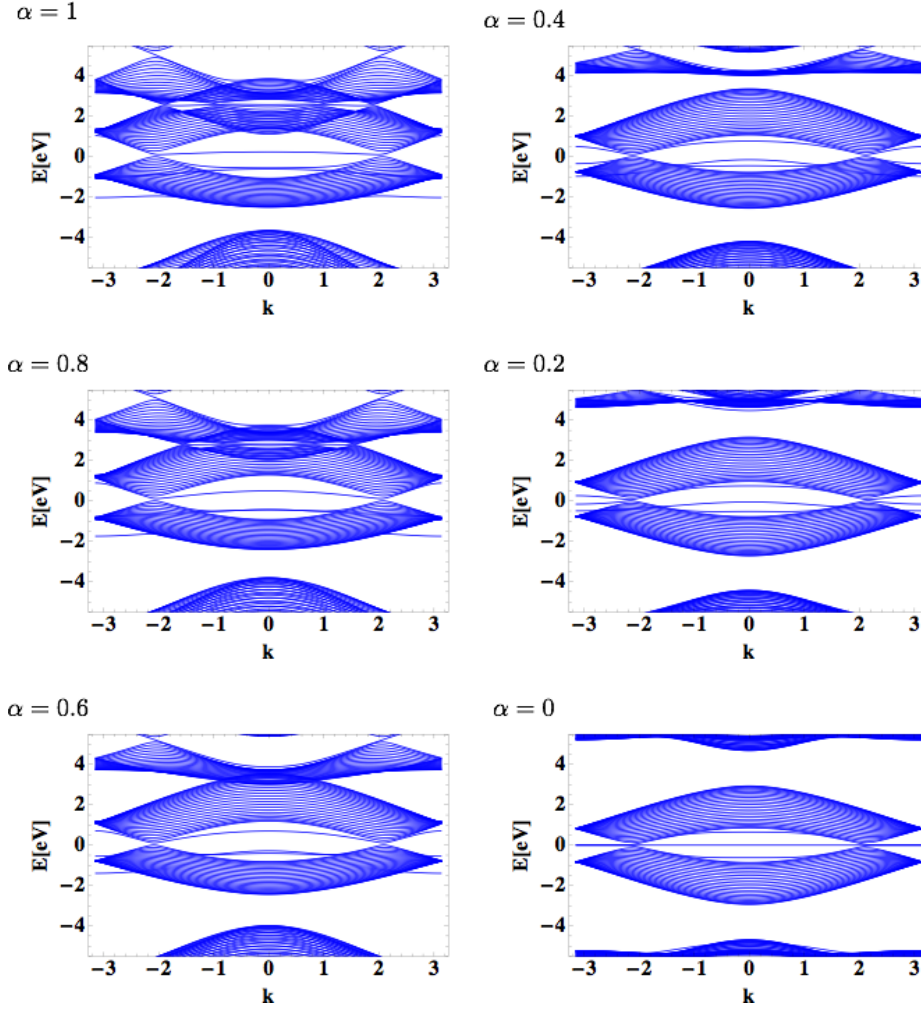
Fig. 4.9   Energy spectra of 1H'/0H silicene ribbon with several variations of on-site energies.

1H'/1H silicene ribbon

Fig.4.10 shows energy spectra of a 1H'/1H zigzag silicene ribbon. As deforming difference between on-site energies from $\alpha = 1$ to $\alpha = 0$, flat bands in the region of k-space $-2\pi/3 \leq k \leq 2\pi/3$ at the Fermi level is shifted to the high energy region, on the other hand flat bands in the regions of $-\pi \leq k \leq -2\pi/3$ and $-2\pi/3 \leq k \leq \pi$ are stable. In addition, an energy band of an edge state around $E \sim -2$eV in the regions of $-\pi \leq k \leq -2\pi/3$ and $2\pi/3 \leq k \leq \pi$, comes close to the Fermi level. For $\alpha = 0$, the edge states in the regions of $-\pi \leq k \leq -2\pi/3$ and $2\pi/3 \leq k \leq \pi$ twofold degenerate.

1H'/1H' silicene ribbon

Fig.4.11 shows energy spectra of a 1H'/1H' zigzag silicene ribbon. As deforming difference between on-site energies from $\alpha = 1$ to $\alpha = 0$, flat bands in the region
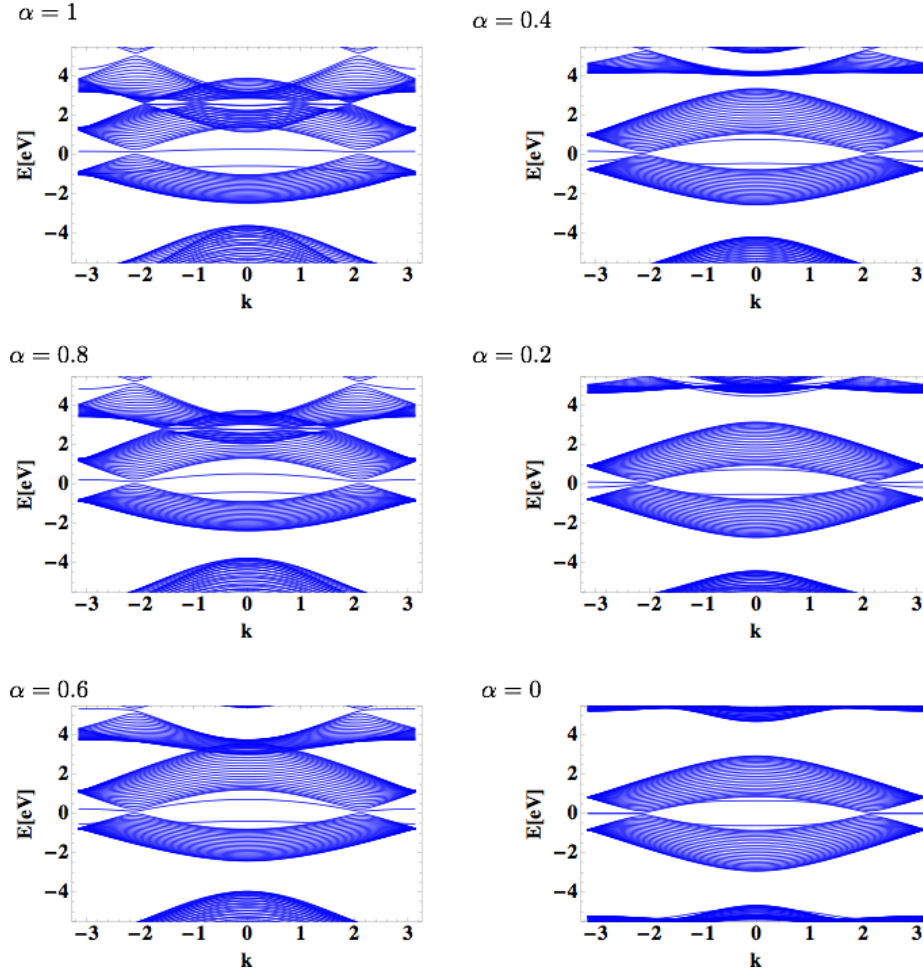
Fig. 4.10   Energy spectra of 1H'/1H silicene ribbon with several variations of on-site energies.

of k-space $-2\pi/3 \leq k \leq 2\pi/3$ at the Fermi level is shifted to the high energy region. In addition, energy bands of edge states around $E \sim -1$eV in the regions of $-\pi \leq k \leq -2\pi/3$ and $2\pi/3 \leq k \leq \pi$, come close to the Fermi level. For $\alpha = 0$, the edge states in the regions of $-\pi \leq k \leq -2\pi/3$ and $2\pi/3 \leq k \leq \pi$ twofold degenerate.

2H/1H' silicene ribbon

Fig.4.12 shows energy spectra of a 2H/1H' zigzag silicene ribbon. As deforming difference between on-site energies from $\alpha = 1$ to $\alpha = 0$, one of doubly degenerated flat bands in the region of k-space $-2\pi/3 \leq k \leq 2\pi/3$ at the Fermi level is shifted to the high energy region. In addition, energy bands of edge states around $E \sim -1$eV in the regions of $-\pi \leq k \leq -2\pi/3$ and $2\pi/3 \leq k \leq \pi$, come close to the Fermi level. For $\alpha = 0$, the flat band edge state in the whole region of k-space emerges and non-degenerate.
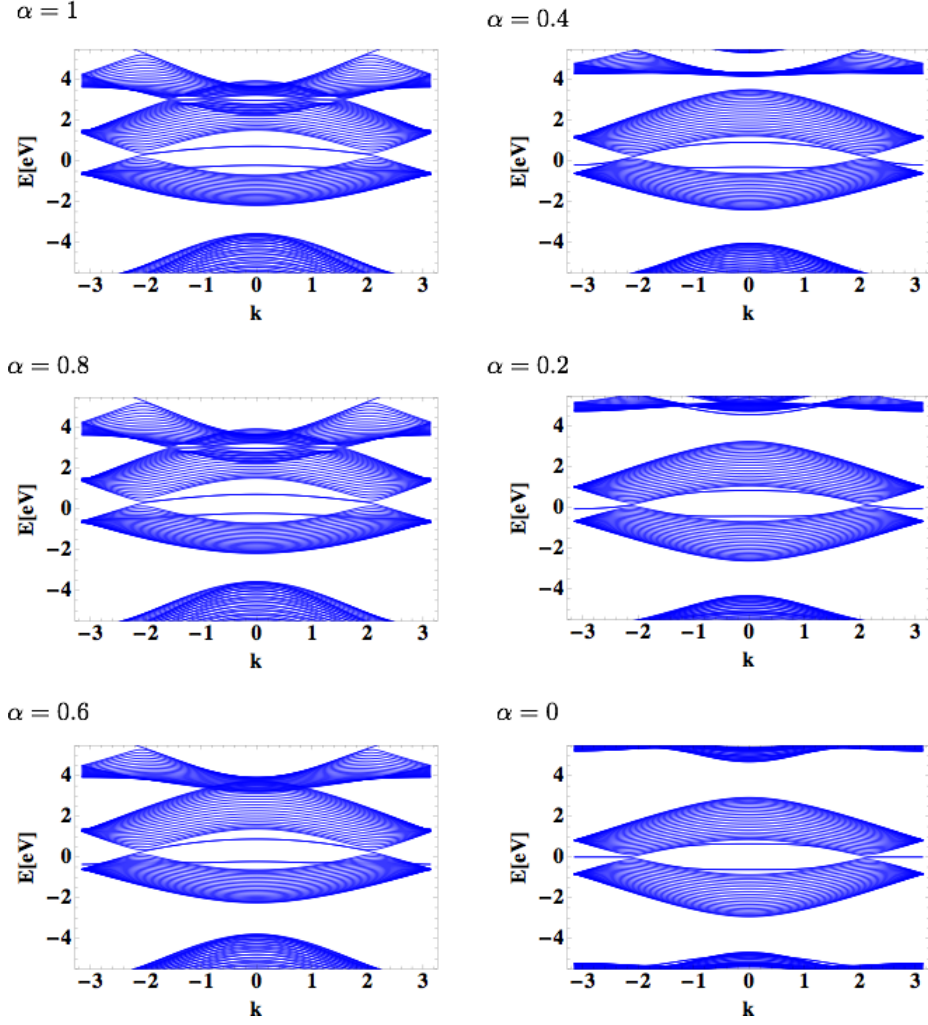
Fig. 4.11 Energy spectra of 1H'/1H' silicene ribbon with several variations of on-site energies.

4.2 Discussion of flat bands in hydrogen terminated silicene ribbons

4.2.1 zero energy flat bands in the chiral symmetric models

Before the consideration of edge states of hydrogen terminated silicene ribbons, we review the zero energy flat bands protected the chiral symmetry following Hatsugai *et. al.*'s discussion[48]. To do this, we consider the eigen value problem of the chiral symmetric hamiltonian $\mathcal{H}$. This hamiltonian can be written $\mathcal{H} = \boldsymbol{c}^\dagger H \boldsymbol{c}$ where $\boldsymbol{c}^\dagger = (c^\dagger_{A1}, c^\dagger_{A2}, \cdots, c^\dagger_{AM}, c^\dagger_{B1}, c^\dagger_{B2}, \cdots, c^\dagger_{BN})$, $c^\dagger_{Ai}(c^\dagger_{Bj})$ is a creation operator at the $i(j)$-th site in $A(B)$ sublattice and H is $(M+N) \times (M+N)$ matrix. H is
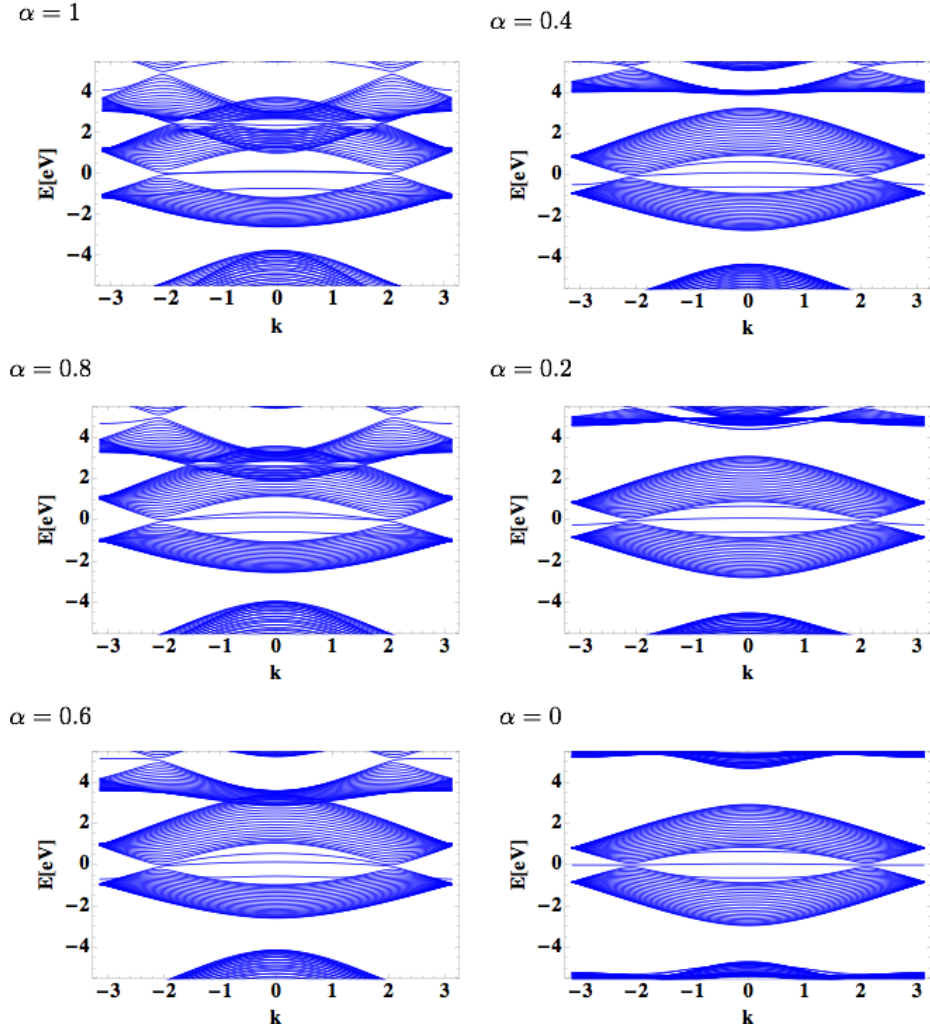
Fig. 4.12   Energy spectra of 2H/1H' silicene ribbon with several variations of on-site energies.

given as follows:

$$H = \begin{pmatrix} O_M & D \\ D^\dagger & O_N \end{pmatrix}, \tag{4.2}$$

where D is $M \times N$ matrix and O_M and O_N are $M \times M$ and $N \times N$ matrices. This H satisfies the anti commutation relation $\{H, \Gamma\} = 0$, where $\Gamma = \mathrm{diag}(I_M, -I_N)$. Here, we assume that $M > N$, and consider eigenvalue problem of this H as

follows:

$$H\Psi = \lambda\Psi$$
$$\Rightarrow$$
$$\det|\lambda I - H| = \det \begin{vmatrix} \lambda I_M & -D \\ -D^\dagger & \lambda I_N \end{vmatrix} = 0$$
$$\Rightarrow$$
$$\det \begin{vmatrix} \lambda I_M & -D \\ -D^\dagger & \lambda I_N \end{vmatrix} = \det \begin{vmatrix} \lambda I_M & -D \\ -D^\dagger + D^\dagger I_M & \lambda I_N - D^\dagger D/\lambda \end{vmatrix}$$
$$= \det \begin{vmatrix} \lambda I_M & -D \\ O_{NM} & \lambda I_N - D^\dagger D/\lambda \end{vmatrix}$$
$$= \lambda^{M-N} \det|\lambda^2 I_N - D^\dagger D|. \tag{4.3}$$

Thus, the minimum number of zero energies is obtained from $M - N$. In this case, the amplitude of wave functions of this zero energy only has A sublattices. Furthermore, zero energy flat bands that emerge in the whole region in k-space, originate from these wave functions. This discussion is also applicable for multi orbital treatment[Fig.4.13(a)].

Based on these discussions, we consider the hydrogen terminated silicene ribbons. Figs.4.13(b) and (c) show hydrogen terminated silicene ribbons whose atomic sites are distinguished between A and B sublattices. The number of orbitals belonging to $A(B)$ sublattice, $N_{A(B)}$, can be given as $N_{A(B)} = 4N_{Si}^{A(B)} + N_H^{A(B)}$ where $N_{Si}^{A(B)}$ is the number of silicon sites of $A(B)$ sublattice, 4 means four orbitals of a silicon atom, and $N_H^{A(B)}$ is the number of hydrogen sites of $A(B)$ sublattice. For $|N_A - N_B| = 1$ as described in Fig.4.13(b), edge states near the Fermi level that have pretty well flat bands in the whole region of k-space, energy bands are continuously connected to the flat bands originated from the chiral symmetry. As the numerical result of edge states (x)[Fig.3.6(b)], an edge state at one side edge does not influence one at another side edge. Thus, for the discussion of edge states, edge states at each edges can be consider separately. Consequently, for $|N_A - N_B| = 0$ as described Fig.4.13(c), edge states also continuously connected to the flat bands in the chiral symmetric models. However, for the edge state without hydrogen terminations, this consideration is inapplicable, because an energy band of this edge state changes shape significantly as continuous deforming of difference between on-site energies. Nevertheless, the edge states of the 0H/0H silicene ribbon is continuously connected to that of the chiral symmetric silicene ribbon. Therefore, in the next section we will consider this edge state in terms of topological aspects using the Berry phase.

4.3 Non-Abelian Berry phase in silicene

In the previous section, we have showed that edge states of silicene ribbons with several hydrogen terminations can be continuously connected to zero energy edge
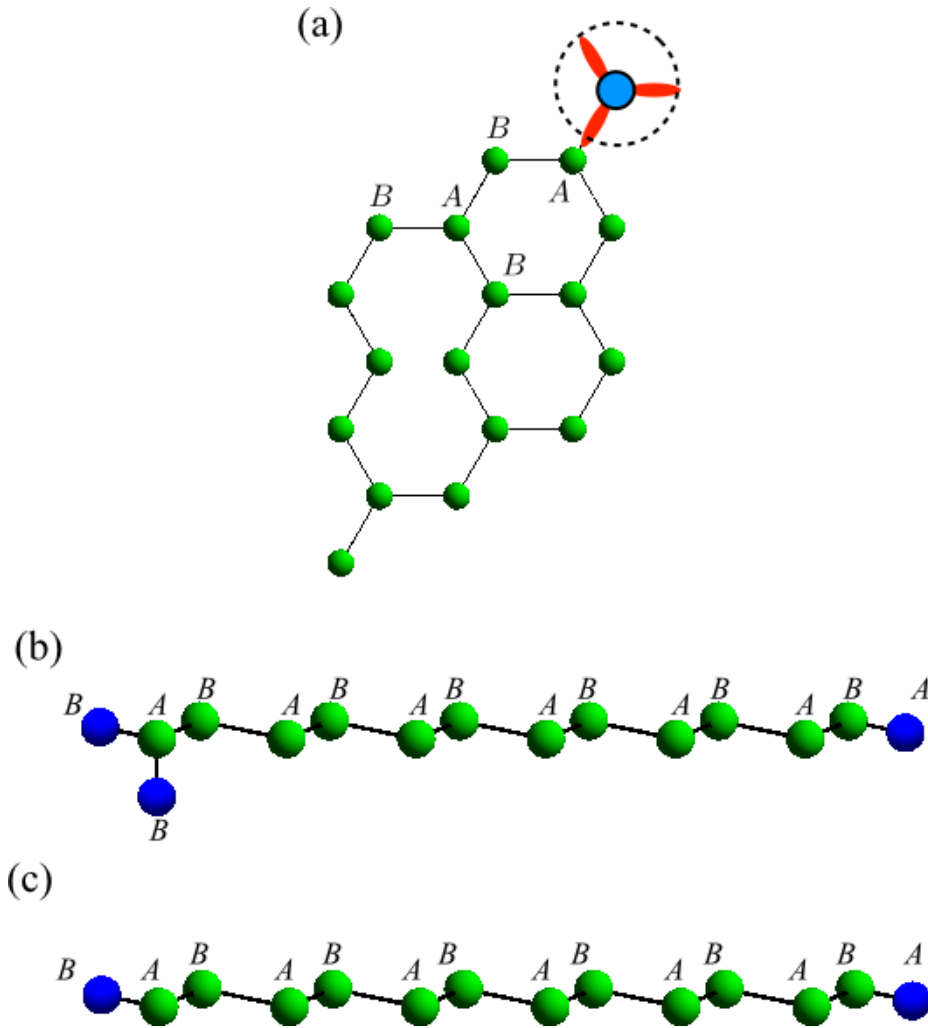
Fig. 4.13   (a) Schematic illustration of silicene distinguished A and B sublattice. Red ellipses and blue circles indicate the hybidized orbitals directed to the another sublattices and normal to the plane of silicene, respectively. Schematic illustration of 2H/1H(b) and 1H/1H(c) hydrogen terminated silicene ribbons distinguished A and B sublattice.

states due to the chiral symmetry. However, the physical origin of edge states of a 0H/0H silicene ribbon is unclear yet. Here, we discuss edge states of a silicene ribbons without hydrogen termination in the point of view of topological aspects using the Berry phase that is calculated from energy eigen states in the wave number space.

4.3.1   Definition of the Berry phase for numerical calculation

To calculate Berry phase numerically, firstly we define the Berry phase $\gamma(k)$ in the wave number space as $\gamma(k) = -i \oint_{k_1} \text{Tr} A(k_1, k)$ where k corresponds to the wave number calculated from the translation vector $\vec{e}_2$[Fig.2.1(b)]. $A(k_1, k)$ is given as

follows

$$A(k_1, k) = \begin{pmatrix} \psi_1^\dagger(k_1,k)d\psi_1(k_1,k) & \psi_1^\dagger(k_1,k)d\psi_2(k_1,k) & \cdots & \psi_1^\dagger(k_1,k)d\psi_N(k_1,k) \\ \psi_2^\dagger(k_1,k)d\psi_1(k_1,k) & \psi_2^\dagger(k_1,k)d\psi_2(k_1,k) & \cdots & \psi_2^\dagger(k_1,k)d\psi_N(k_1,k) \\ \vdots & \vdots & \ddots & \vdots \\ \psi_N^\dagger(k_1,k)d\psi_1(k_1,k) & \psi_N^\dagger(k_1,k)d\psi_2(k_1,k) & \cdots & \psi_N^\dagger(k_1,k)d\psi_N(k_1,k) \end{pmatrix},$$

$$(4.4)$$

where $\psi_i(k_1, k)$ are energy eigen states of the Fourier transformed hamiltonian $H(k_1, k)$ with eigen energy $\epsilon_i (i = 1, \cdots, N = 4, 5, \cdots, 8)$. Furthermore, we assume that $\epsilon_1 < \epsilon_2 < \cdots < \epsilon_{N=4} < \epsilon_5 < \cdots < \epsilon_8$ for the definition of the Berry phase. When $\epsilon_{N=4} = \epsilon_5$, the Berry phase is undefined. For the numerical calculation, we discretize the wave number k_1 as $k_1 = \frac{2\pi j}{N_B}(N_B = 40, j = -N_B/2, -N_B/2 + 1, \cdots, N_B/2 - 1)$. According to Eq.2.26, the Berry phase $\gamma(k)$ is written as follows:

$$\gamma(k) = \arg \det[(\Psi^\dagger(\frac{2\pi(-N_B/2)}{N_B}, k)\Psi(\frac{2\pi(-N_B/2 + 1)}{N_B}, k))$$
$$\times (\Psi^\dagger(\frac{2\pi(-N_B/2 + 1)}{N_B}, k)\Psi(\frac{2\pi(-N_B/2 + 2)}{N_B}, k))$$
$$\times \cdots (\Psi^\dagger(\frac{2\pi(j)}{N_B}, k)\Psi(\frac{2\pi(j + 1)}{N_B}, k)) \cdots (\Psi^\dagger(\frac{2\pi(N_B/2 - 1)}{N_B}, k)\Psi(\frac{2\pi(-N_B/2)}{N_B}, k))],$$

$$(4.5)$$

where $(\Psi^\dagger(\frac{2\pi(j)}{N_B}, k)\Psi(\frac{2\pi(j+1)}{N_B}, k))$ is written as follows:

$$(\Psi^\dagger(\frac{2\pi(j)}{N_B}, k)\Psi(\frac{2\pi(j + 1)}{N_B}, k)) =$$
$$\begin{pmatrix} \psi_1^\dagger(\frac{2\pi(j)}{N_B},k)d\psi_1(\frac{2\pi(j+1)}{N_B},k) & \psi_1^\dagger(\frac{2\pi(j)}{N_B},k)d\psi_2(\frac{2\pi(j+1)}{N_B},k) & \cdots & \psi_1^\dagger(\frac{2\pi(j)}{N_B},k)d\psi_N(\frac{2\pi(j+1)}{N_B},k) \\ \psi_2^\dagger(\frac{2\pi(j)}{N_B},k)d\psi_1(\frac{2\pi(j+1)}{N_B},k) & \psi_2^\dagger(\frac{2\pi(j)}{N_B},k)d\psi_2(\frac{2\pi(j+1)}{N_B},k) & \cdots & \psi_2^\dagger(\frac{2\pi(j)}{N_B},k)d\psi_N(\frac{2\pi(j+1)}{N_B},k) \\ \vdots & \vdots & \ddots & \vdots \\ \psi_N^\dagger(\frac{2\pi(j)}{N_B},k)d\psi_1(\frac{2\pi(j+1)}{N_B},k) & \psi_N^\dagger(\frac{2\pi(j)}{N_B},k)d\psi_2(\frac{2\pi(j+1)}{N_B},k) & \cdots & \psi_N^\dagger(\frac{2\pi(j)}{N_B},k)d\psi_N(\frac{2\pi(j+1)}{N_B},k) \end{pmatrix}.$$

$$(4.6)$$

4.3.2 Numerical results of the Berry phase

Fig.4.14 shows the numerical results of the Berry phase. In these figures, Berry phase changed around $k = \frac{-2\pi}{3}$ and $k = \frac{2\pi}{3}$ reflecting energy gap closing for bulk. For $k = \frac{-2\pi}{3}$ and $k = \frac{2\pi}{3}$, the Berry phase is undefined because of a degeneracy. As mentioned in Sec.2.3, the Berry phase quantizes as 0 or π modulo 2π for the chiral symmetric silicene. For $\alpha = 0$ that corresponds to the chiral symmetric silicene, the Berry phase is π in $-\frac{2\pi}{3} < k < \frac{2\pi}{3}$, on the other hand the Berry phase is 0 in $-\pi < k < -\frac{2\pi}{3}$ and $\frac{2\pi}{3} < k < \pi$. As continuous deforming of difference between on-site energies, Berry phases are stable in each regions of π and 0. Thus this result means that edge states of 0H/0H silicene ribbon exist in the region of $-\frac{2\pi}{3} < k < \frac{2\pi}{3}$.
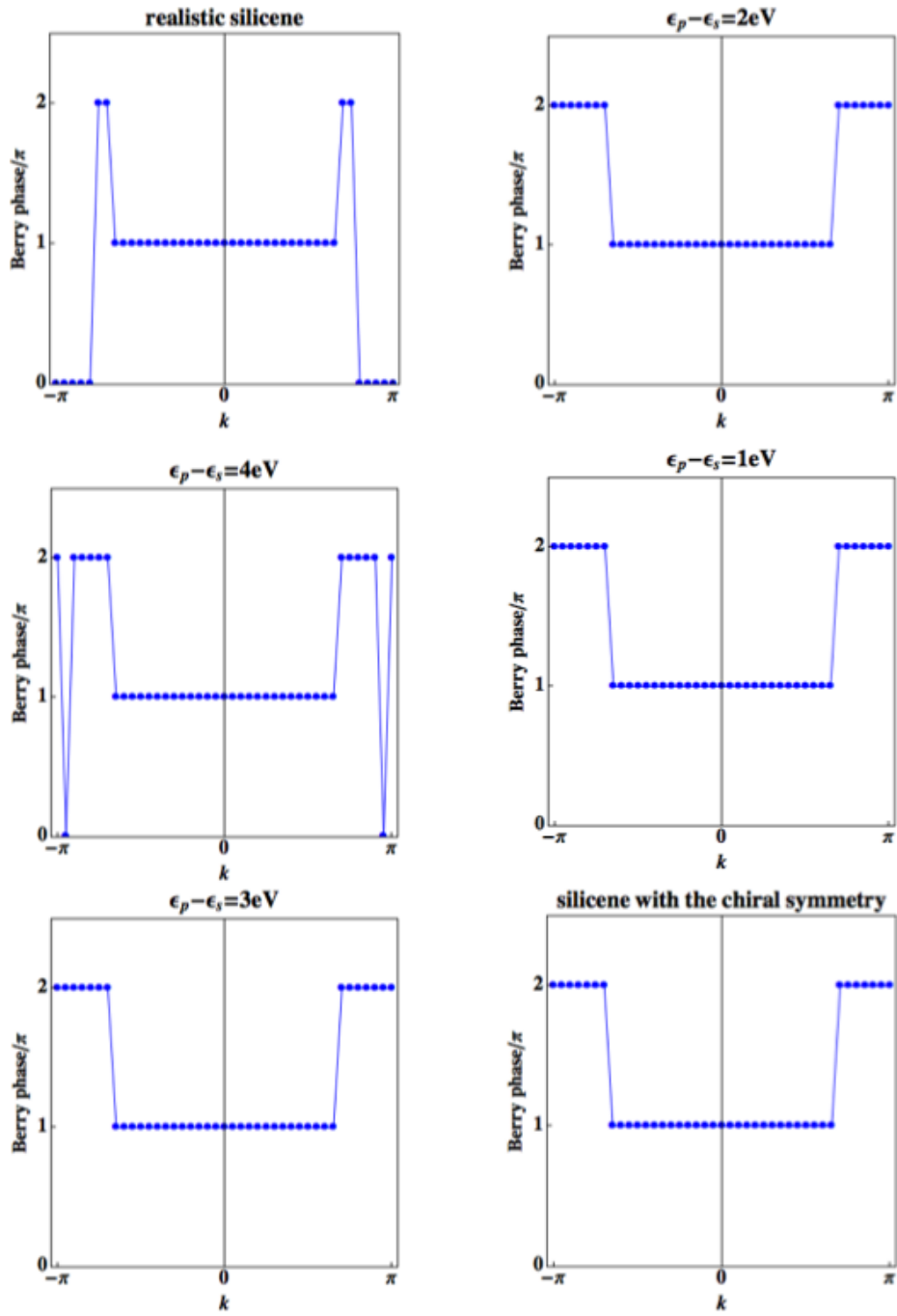
Fig. 4.14 Numerical calculation results of Berry phase as deforming on-site energies from a realistic silicene ribbon to a chiral symmetric silicene ribbons as function of k. Berry phases are normalized by π.

Chapter 5

Conclusion

In this thesis, we have investigated edge states in hydrogen terminated zigzag silicene ribbons as a Dirac fermion system and its physical origin via a multi orbital tight binding model on a honeycomb lattice. To do this, we have numerically calculated energy spectra of zigzag silicene ribbons with several types of hydrogen terminations and the Berry phase. In such cases, we have also took into account the continuous deformation of on-site energies of s and p orbitals that means to a continuous deformation from realistic models of silicene to chiral symmetric models of silicene.

Firstly, we have compare energy spectra of 0H/0H and 1H/1H zigzag silicene ribbons to zigzag graphene ribbons with or without hydrogen terminations. In the energy spectrum of zigzag graphene ribbons with hydrogen termination, we have obtained energy spectrum near the Fermi level consistent with one calculated from single orbital tight binding model. Besides, for the case of silicene ribbon, we have obtained an energy spectrum similar to ones of a zigzag graphene ribbon with hydrogen termination near the Fermi level. Additionally, we found that main components of the wave functions of these edge states of silicene are p_Z components at the edges similar to the edge states of zigzag graphene ribbons. On the other hand, in the numerical result of energy spectra of zigzag graphene ribbons without hydrogen termination, edge states originated from σ orbitals as dangling bonds emerge near the Fermi level. These edge states have been also obtained by DFT calculations. In a silicene ribbon without a hydrogen termination, we find new edge states different from one of a graphene ribbon. If an ideal zigzag silicene ribbon without hydrogen termination can be synthesized experimentally, then these edge states may be observed.

Next, we have investigated effects of hydrogen terminations to edge states of zigzag silicene ribbons through the consideration of several types of hydrogen terminations. For the energy spectrum of silicene ribbon with 2H/2H hydrogen termination, we have obtained that edge states in the region of wave number $-2\pi/3 < k < 2\pi/3$ like ones of a graphene ribbon with the Klien edge and wave functions of edge states localize at the inner sites from edge sites. This results imply that the Klein edge fictitiously realized at both edges due to a termination of two dangling bonds at both edge sites. In addition, for the energy spectrum of silicene ribbon with 2H/1H hydrogen termination, we have obtained an edge state

consistent with one calculated by DFT calculation. This edge state is pretty well flat band and emerges in the whole region of wave number.

In order to clarify physical origin of edge states obtained from energy spectra, we have investigated behaviors of energy spectra of silicene ribbons with several types of termination as deforming on-site energies of s and p orbitals and have found that flat bands emerging in energy spectra in realistic models of hydrogen terminated silicene ribbons, is continuously connected to flat bands of hydrogen terminated silicene ribbons with chiral symmetry. However, for a silicene ribbon without hydrogen termination near the Fermi level, its edge states cannot be interpreted based on the chiral symmetry.

Thus, we have changed one's perception of edge states and focused on the topological aspects of edge states in terms of bulk properties. To do this, we have calculated the Berry phase that called the Zak phase numerically, which calculated from eigen energy states in the wave number space. As deforming difference of on-site energies between s and p orbitals, Berry phase stably quantized as 0 or π modulo 2π. For the chiral symmetric model, Berry phase quantized analytically reflecting degeneracy of zero-energy edge states. In the region of wave number $-2\pi/3 < k < 2\pi/3$, Berry phase is π, on the other hand in the regions of $-\pi < k < -2\pi/3$ and $2\pi/3 < k < \pi$, Berry phase is 0. Similar to the case of the chiral symmetric silicene, for the realistic silicene, numerical results of Berry phase are 0 in the regions of $-\pi < k < -2\pi/3$ and $2\pi/3 < k < \pi$, and are π in the region of the wave number $-2\pi/3 < k < 2\pi/3$. This means that edge states of a 0H/0H zigzag silicene ribbon exist in the region of wave number $-2\pi/3 < k < 2\pi/3$ and the Berry phase is quantized due to the other symmetry different from the chiral symmetry.

In conclusion, we would like to emphasizes the possibility of realization of exotic edge states in silicene due to the buckled structures and considerations of several types of edge termination.

Bibliography

[1] Kyozaburo Takeda and Kenji Shiraishi. Theoretical possibility of stage corrugation in si and ge analogs of graphite. *Phys. Rev. B*, Vol. 50, pp. 14916–14922, Nov 1994.

[2] S. Cahangirov, M. Topsakal, E. Aktürk, H. Şahin, and S. Ciraci. Two- and one-dimensional honeycomb structures of silicon and germanium. *Phys. Rev. Lett.*, Vol. 102, p. 236804, Jun 2009.

[3] Boubekeur Lalmi, Hamid Oughaddou, Hanna Enriquez, Abdelkader Kara, Sébastien Vizzini, Bénidicte Ealet, and Bernard Aufray. Epitaxial growth of a silicene sheet. *Applied Physics Letters*, Vol. 97, No. 22, p. 223109, 2010.

[4] Chun-Liang Lin, Ryuichi Arafune, Kazuaki Kawahara, Noriyuki Tsukahara, Emi Minamitani, Yousoo Kim, Noriaki Takagi, and Maki Kawai. Structure of silicene grown on ag(111). *Applied Physics Express*, Vol. 5, No. 4, p. 045802, 2012.

[5] Patrick Vogt, Paola De Padova, Claudio Quaresima, Jose Avila, Emmanouil Frantzeskakis, Maria Carmen Asensio, Andrea Resta, Bénédicte Ealet, and Guy Le Lay. Silicene: Compelling experimental evidence for graphenelike two-dimensional silicon. *Phys. Rev. Lett.*, Vol. 108, p. 155501, Apr 2012.

[6] Baojie Feng, Zijing Ding, Sheng Meng, Yugui Yao, Xiaoyue He, Peng Cheng, Lan Chen, and Kehui Wu. Evidence of silicene in honeycomb structures of silicon on ag(111). *Nano Letters*, Vol. 12, No. 7, pp. 3507–3511, 2012.

[7] H Jamgotchian, Y Colignon, N Hamzaoui, B Ealet, J Y Hoarau, B Aufray, and J P Bibrian. Growth of silicene layers on ag(111): unexpected effect of the substrate temperature. *Journal of Physics: Condensed Matter*, Vol. 24, No. 17, p. 172001, 2012.

[8] Antoine Fleurence, Rainer Friedlein, Taisuke Ozaki, Hiroyuki Kawai, Ying Wang, and Yukiko Yamada-Takamura. Experimental evidence for epitaxial silicene on diboride thin films. *Phys. Rev. Lett.*, Vol. 108, p. 245501, Jun 2012.

[9] Lei Meng, Yeliang Wang, Lizhi Zhang, Shixuan Du, Rongting Wu, Linfei Li, Yi Zhang, Geng Li, Haitao Zhou, Werner A. Hofer, and Hong-Jun Gao. Buckled silicene formation on ir(111). *Nano Letters*, Vol. 13, No. 2, pp. 685–690, 2013.

[10] C. Leandri, G. Le Lay, B. Aufray, C. Girardeaux, J. Avila, M.E. Dvila, M.C. Asensio, C. Ottaviani, and A. Cricenti. Self-aligned silicon quantum wires on ag(110). *Surface Science*, Vol. 574, No. 1, pp. L9 – L15, 2005.

[11] Paola De Padova, Claudio Quaresima, Paolo Perfetti, Bruno Olivieri, Christel Leandri, Bernard Aufray, Sebastien Vizzini, and Guy Le Lay. Growth

of straight, atomically perfect, highly metallic silicon nanowires with chiral asymmetry. *Nano Letters*, Vol. 8, No. 1, pp. 271–275, 2008. PMID: 18092826.

[12] Paola De Padova, Claudio Quaresima, Carlo Ottaviani, Polina M. Sheverdyaeva, Paolo Moras, Carlo Carbone, Dinesh Topwal, Bruno Olivieri, Abdelkader Kara, Hamid Oughaddou, Bernard Aufray, and Guy Le Lay. Evidence of graphene-like electronic signature in silicene nanoribbons. *Applied Physics Letters*, Vol. 96, No. 26, p. 261905, 2010.

[13] Fabio Ronci, Stefano Colonna, Antonio Cricenti, Paola De Padova, Carlo Ottaviani, Claudio Quaresima, Bernard Aufray, and Guy Le Lay. Low temperature stm/sts study of silicon nanowires grown on the ag(110) surface. *physica status solidi (c)*, Vol. 7, No. 11-12, pp. 2716–2719, 2010.

[14] Bernard Aufray, Abdelkader Kara, Sébastien Vizzini, Hamid Oughaddou, Christel Léandri, Benedicte Ealet, and Guy Le Lay. Graphene-like silicon nanoribbons on ag(110): A possible formation of silicene. *Applied Physics Letters*, Vol. 96, No. 18, p. 183102, 2010.

[15] Paola De Padova, Claudio Quaresima, Bruno Olivieri, Paolo Perfetti, and Guy Le Lay. sp2-like hybridization of silicon valence orbitals in silicene nanoribbons. *Applied Physics Letters*, Vol. 98, No. 8, pp. –, 2011.

[16] Abdelkader Kara, Sbastien Vizzini, Cristel Leandri, Benedicte Ealet, Hamid Oughaddou, Bernard Aufray, and Guy LeLay. Silicon nano-ribbons on ag(110): acomputational investigation. *Journal of Physics: Condensed Matter*, Vol. 22, No. 4, p. 045004, 2010.

[17] Paola De Padova, Osamu Kubo, Bruno Olivieri, Claudio Quaresima, Tomonobu Nakayama, Masakazu Aono, and Guy Le Lay. Multilayer silicene nanoribbons. *Nano Letters*, Vol. 12, No. 11, pp. 5500–5503, 2012.

[18] Paola De Padova, Patrick Vogt, Andrea Resta, Jose Avila, Ivy Razado-Colambo, Claudio Quaresima, Carlo Ottaviani, Bruno Olivieri, Thomas Bruhn, Toru Hirahara, Terufusa Shirai, Shuji Hasegawa, Maria Carmen Asensio, and Guy Le Lay. Evidence of dirac fermions in multilayer silicene. *Applied Physics Letters*, Vol. 102, No. 16, p. 163106, 2013.

[19] Zhi-Xin Guo, Shinnosuke Furuya, Jun ichi Iwata, and Atsushi Oshiyama. Absence of dirac electrons in silicene on ag(111) surfaces. *Journal of the Physical Society of Japan*, Vol. 82, No. 6, p. 063714, 2013.

[20] Seymur Cahangirov, Martha Audiffred, Peizhe Tang, Amilcare Iacomino, Wenhui Duan, Gabriel Merino, and Angel Rubio. Electronic structure of silicene on ag(111): Strong hybridization effects. *Phys. Rev. B*, Vol. 88, p. 035432, Jul 2013.

[21] Chun-Liang Lin, Ryuichi Arafune, Kazuaki Kawahara, Mao Kanno, Noriyuki Tsukahara, Emi Minamitani, Yousoo Kim, Maki Kawai, and Noriaki Takagi. Substrate-induced symmetry breaking in silicene. *Phys. Rev. Lett.*, Vol. 110, p. 076801, Feb 2013.

[22] J Avila, P De Padova, S Cho, I Colambo, S Lorcy, C Quaresima, P Vogt, A Resta, G Le Lay, and M C Asensio. Presence of gapped silicene-derived band in the prototypical (3×3) silicene phase on silver (111) surfaces. *Journal of Physics: Condensed Matter*, Vol. 25, No. 26, p. 262001, 2013.

[23] Cheng-Cheng Liu, Wanxiang Feng, and Yugui Yao. Quantum spin hall effect in silicene and two-dimensional germanium. *Phys. Rev. Lett.*, Vol. 107, p. 076802, Aug 2011.

[24] Cheng-Cheng Liu, Hua Jiang, and Yugui Yao. Low-energy effective hamiltonian involving spin-orbit coupling in silicene and two-dimensional germanium and tin. *Phys. Rev. B*, Vol. 84, p. 195430, Nov 2011.

[25] Motohiko Ezawa. A topological insulator and helical zero mode in silicene under an inhomogeneous electric field. *New Journal of Physics*, Vol. 14, No. 3, p. 033003, 2012.

[26] Motohiko Ezawa and Naoto Nagaosa. Interference of topologically protected edge states in silicene nanoribbons. *Phys. Rev. B*, Vol. 88, p. 121401, Sep 2013.

[27] Motohiko Ezawa. Quantum hall effects in silicene. *Journal of the Physical Society of Japan*, Vol. 81, No. 6, p. 064705, 2012.

[28] Motohiko Ezawa. Dirac theory and topological phases of silicon nanotube. *EPL (Europhysics Letters)*, Vol. 98, No. 6, p. 67001, 2012.

[29] Motohiko Ezawa. Quasi-topological insulator and trigonal warping in gated bilayer silicene. *Journal of the Physical Society of Japan*, Vol. 81, No. 10, p. 104713, 2012.

[30] Ko Kikutake, Motohiko Ezawa, and Naoto Nagaosa. Edge states in silicene nanodisks. *Phys. Rev. B*, Vol. 88, , Sep 2013.

[31] Mitsutaka Fujita, Katsunori Wakabayashi, Kyoko Nakada, and Koichi Kusakabe. Peculiar localized state at zigzag graphite edge. *Journal of the Physical Society of Japan*, Vol. 65, No. 7, pp. 1920–1923, 1996.

[32] D.J. Klein. Graphitic polymer strips with edge states. *Chemical Physics Letters*, Vol. 217, No. 3, pp. 261 – 265, 1994.

[33] D. J. Klein and L. Bytautas. Graphitic edges and unpaired π-electron spins. *The Journal of Physical Chemistry A*, Vol. 103, No. 26, pp. 5196–5210, 1999.

[34] Susumu Okada and Atsushi Oshiyama. Magnetic ordering in hexagonally bonded sheets with first-row elements. *Phys. Rev. Lett.*, Vol. 87, p. 146803, Sep 2001.

[35] Yousuke Kobayashi, Ken-ichi Fukui, Toshiaki Enoki, Koichi Kusakabe, and Yutaka Kaburagi. Observation of zigzag and armchair edges of graphite using scanning tunneling microscopy and spectroscopy. *Phys. Rev. B*, Vol. 71, p. 193406, May 2005.

[36] Shinsei Ryu and Yasuhiro Hatsugai. Topological origin of zero-energy edge states in particle-hole symmetric systems. *Phys. Rev. Lett.*, Vol. 89, p. 077002, Jul 2002.

[37] B. I. Halperin. Quantized hall conductance, current-carrying edge states, and the existence of extended states in a two-dimensional disordered potential. *Phys. Rev. B*, Vol. 25, pp. 2185–2190, Feb 1982.

[38] T. Kennedy. *J. Phys . Condens. Matter*, Vol. 2, p. 5737, 1990.

[39] Yasuhiro Hatsugai. Chern number and edge states in the integer quantum hall effect. *Phys. Rev. Lett.*, Vol. 71, pp. 3697–3700, Nov 1993.

[40] D. J. Thouless, M. Kohmoto, M. P. Nightingale, and M. den Nijs. Quantized

hall conductance in a two-dimensional periodic potential. *Phys. Rev. Lett.*, Vol. 49, pp. 405–408, Aug 1982.

[41] Qian Niu, D. J. Thouless, and Yong-Shi Wu. Quantized hall conductance as a topological invariant. *Phys. Rev. B*, Vol. 31, pp. 3372–3377, Mar 1985.

[42] M. V. Berry. *Proc. R. Soc. Lond. A*, Vol. 392, p. 45, 1984.

[43] Yasuhiro Hatsugai. *Journal of the Physical Society of Japan*, Vol. 75, p. 123601, 2006.

[44] T. Kariyado and Y. Hatsugai. Symmetry Protected Quantization and Bulk-Edge Correspondence of Massless Dirac Fermions: Application to Fermionic Shastry-Sutherland Model. *ArXiv e-prints*, July 2013.

[45] J. V. Neumann and E. P. Wigner. *Phys. Z*, Vol. 30, p. 467, 1929.

[46] J. Zak. Berry's phase for energy bands in solids. *Phys. Rev. Lett.*, Vol. 62, pp. 2747–2750, Jun 1989.

[47] Y. Hatsugai. Bulk-edge correspondence in graphene with/without magnetic field: Chiral symmetry, dirac fermions and edge states. *Solid State Communications*, Vol. 149, 27—28, pp. 1061 – 1067, 2009. Recent Progress in Graphene Studies.

[48] Y. Hatsugai and I. Maruyama. Z q topological invariants for polyacetylene, kagome and pyrochlore lattices. *EPL (Europhysics Letters)*, Vol. 95, No. 2, p. 20003, 2011.

[49] Shinsei Ryu and Yasuhiro Hatsugai. Zero-energy edge states and chiral symmetry breaking at edges of graphite sheets. *Physica E: Low-dimensional Systems and Nanostructures*, Vol. 22, 1—3, pp. 679 – 683, 2004. 15th International Conference on Electronic Propreties of Two-Dimensional Systems (EP2DS-15).

[50] Koichi Kusakabe and Masanori Maruyama. Magnetic nanographite. *Phys. Rev. B*, Vol. 67, p. 092406, Mar 2003.

[51] Maxim Ziatdinov, Shintaro Fujii, Koichi Kusakabe, Manabu Kiguchi, Takehiko Mori, and Toshiaki Enoki. Visualization of electronic states on atomically smooth graphitic edges with different types of hydrogen termination. *Phys. Rev. B*, Vol. 87, p. 115427, Mar 2013.

[52] Leopold Talirz, Hajo Sde, Jinming Cai, Pascal Ruffieux, Stephan Blankenburg, Rached Jafaar, Reinhard Berger, Xinliang Feng, Klaus Mllen, Daniele Passerone, Roman Fasel, and Carlo A. Pignedoli. Termini of bottom-up fabricated graphene nanoribbons. *Journal of the American Chemical Society*, Vol. 135, No. 6, pp. 2060–2063, 2013.

[53] Xiaowei Zhang, Oleg V. Yazyev, Juanjuan Feng, Liming Xie, Chenggang Tao, Yen-Chia Chen, Liying Jiao, Zahra Pedramrazi, Alex Zettl, Steven G. Louie, Hongjie Dai, and Michael F. Crommie. Experimentally engineering the edge termination of graphene nanoribbons. *ACS Nano*, Vol. 7, No. 1, pp. 198–202, 2013.

[54] Jun Kang, Fengmin Wu, and Jingbo Li. Symmetry-dependent transport properties and magnetoresistance in zigzag silicene nanoribbons. *Applied Physics Letters*, Vol. 100, No. 23, p. 233122, 2012.

[55] Yi Ding and Yanli Wang. Electronic structures of zigzag silicene nanoribbons

with asymmetric sp[sup 2] - sp[sup 3] edges. *Applied Physics Letters*, Vol. 102, No. 14, p. 143115, 2013.

[56] J. C. Slater and G. F. Koster. Simplified lcao method for the periodic potential problem. *Phys. Rev.*, Vol. 94, pp. 1498–1524, Jun 1954.

[57] Yu-Ling Song, Yan Zhang, Jian-Min Zhang, and Dao-Bang Lu. Effects of the edge shape and the width on the structural and electronic properties of silicene nanoribbons. *Applied Surface Science*, Vol. 256, No. 21, pp. 6313 – 6317, 2010.

[58] Yoshiyuki Miyamoto, Kyoko Nakada, and Mitsutaka Fujita. First-principles study of edge states of h-terminated graphitic ribbons. *Phys. Rev. B*, Vol. 59, pp. 9858–9861, Apr 1999.

[59] W. A. Harrison. *Electronic Structure and Properties of Solids-The Physics of Chemical Bonds.* Dover, 1980.

[60] 関大地. 有限形状グラフェンにおける z2 ベリー位相, 2009.